PFC/RR-94-1

PROPULSION RESEARCH ON THE VARIABLE I_{SP} TANDEM MIRROR PLASMA ROCKET FINAL REPORT

T. F. Yang

F. R. Chang-Díaz*

January 28, 1994

Plasma Fusion Center

massachusetts Institute of Technology

Cambridge, MA 02139 USA

This work was supported by NASA under Contract #NAS-9-18372, NASA/JPL under Contract #958265 and AFOSR under Contract #AFOSR-89-0345.

*Astronaut Office of the Johnson Space Center

Contents

ABSTRACT

Several milestones have been achieved towards the realization of a practical space plasma thruster from the tandem mirror rocket experiment, i.e. the specifi impulse, thrust, energy conversion efficiency, and mass flow-rate have been determined. The experiment operates at 9.4 kW of input power at an rf-to-plasma efficiency of 68%; The ion temperature is 172 eV (2,000,000 K) which gives an I_{sp} of 12,852 s. The thrust is 76 mN (milli Newton) which is a high value for a low input power (9.4 kW) and very high I_{sp} (12,852 s). The radiation loss was found to be very low. Most important, these results fall within our prediction.

A key advantage of this propulsion system is its high energy density that can be contained in the plasma. A flight system design and analysis has shown that the present experimental device can handle a power level in excess of 10 MW, resulting in specific weights as low as 0.04 kg/kW. The overall specific weight of a space vehicle for a piloted Mars mission, including nuclear power and power conditioning equipment, is only 8 kg/kW. This is a conservative value which can be further reduced to 6 kg/kW.

A 150 day trip to Mars (480 day round trip including 90 days stay over) can be achieved with only 10 MW of power. The trip time has been optimized by varying the I_{sp} and thrust to meet a required returned mass of 57,000 kg. In that study an efficiency of only 50% was assumed. Except for nuclear power, the technology involved is state-of-the-art with very minimal engineering scaling. In addition, substantial advancements in high temperature superconductors, solid state transmitters and power conditioning equipment are expected. Such development makes this device a most competitive electric propulsion approach when it is fully developed. The concept can be demonstrated near-term as gauged on our rapid, limited resource progress.

Our future goal is to reach a plasma coupling efficiency as high as 90%. This expectation is reasonable because there is sufficient room for improvement as shown by our theoretical analyses. These studies predict that higher coupling efficiency can be obtained if the magnetic field is made more uniform and the plasma radius larger. At present, the ionization efficiency is very low because the microwave frequency is not in resonance with electron cyclotron frequency. The efficiency is expected to improve when the newly installed 14.5 GHz microwave transmitter becomes operational. This frequency is closer to resonance at the operating fields of the experiment (2.0 to 10.0 kG). These features will be implemented in our future experiment.

A general review of this research is given in the introduction section. Section 2 summarizes the progress made in the past year. The detailed discussions of the theoretical work, thrust balance development, laser fluorescence system development, flight system design, exhaust modeling and experimental results are given in sections 3, 4, 5, 6 and 7. Among these topics, the theoretical analysis of wave propagation, some important experimental results

and flight system design and exhaust modeling have been presented in the previous reports. They are included here to give the complete picture and to show the depth and broadness of this research project.

1 Introduction

We have often pointed out that the tandem mirror plasma rocket has the potential of being a highly efficient propulsion device with variable I_{sp} and thrust from low to very high values. Such a propulsion system hinges on the reliable production and controlled exhaust of plasma from an rf heated tandem mirror device. To this general end, an experimental research program was initiated at MIT in 1988 [1],[2], [3],[4],[5],[6].

It is the point of the time and for future development that we reiterate the advantages of this rocket engine, as weel as the reasons, purposes and scenario of this research. It has been shown in fusion energy research on a Tandem Mirror device that the plasma can be heated to as high 3,000,000 K, but at very low density (typically in the neighborhood of $5 \times 10^{18} m^{-3}$). This high plasma ion temperature will give a very high specific impulse not attainable by other electrical propulsion methods with the exception of ion propulsion. The thrust of an ion engine is very low while the thrust of a tandem mirror engine can be potentially very high by operating the system at low temperature and high density. A very important feature unique to this rocket engine is that both the thrust and specific impulse can be varied by controlling the temperature and density. Also the relationship of the variation of these two parameters in this engine is the most desirable, i.e., this engine can be operated at high thrust and low specific impulse and vice versa at constant power level, whereas in the other types of electric systems high thrust always associates with high specific impulse and high power. Therefore high thrust can be delivered to the vehicle when it is accelerated from low speed and the thrust can be tapered off when the vehicle is approaching a cruising speed. The spacecraft can then be flown at constant power. This is an economical way of utilizing the precious space power and an efficient way of flying. Another advantage is that this system can be operated at either steady state or pulse mode. The energy conversion efficiency is very high with ICRF (ion cyclotron resonance frequency) heating method.

However, the tandem mirror device is by no means mature enough for direct application to space propulsion. As it was pointed out previously, the Tandem Mirror devices for fusion energy research are large and heavy, whereas the propulsion device must be compact and light weight. Hence we must first demonstrate that the projected plasma parameters are achievable in a compact device (which was accomplished in the first year of our research). For propulsion purposes the preferred plasma temperature is much lower than the temperature required for ignition, with much higher density. Low temperature and high density plasma conditions have to be established. The mode of operation is also different. For a fusion energy reactor the plasma has to be well confined and the end leakage should be kept as low as possible. On the other hand, for propulsion purposes the fuel gas has to be fed, ionized, heated and exhausted in a controlled fashion. Such a dynamic mode of streaming plasma operation is unknown and has to be developed.

The desirable temperature range for propulsion application is from 5 to 100 eV (1.16 million degrees K) and density range is from $10^{18}cm^{-3}$ to $10^{20}cm^{-3}$. To obtain such a wide range of plasma parameters extensive research is required. The physics of wave propagation and dissipation in the plasma in a mirror geometry had not yet been fully investigated before the mirror fusion program was terminated. Since the ICRF heating is chosen as the method for transfering electric energy to the propulsive energy, a full understanding of the wave-plasma physics has to be realized. The management of the advanced propulsion group at JPL appreciated this need and wisely advised us to concentrate on the understanding of the physics involving the ICRF heating at the time when this project was funded. Therefore analytic, numerical and experimental studies on the physics of wave propagation and absorption in the plasma of the mirror device have been undertaken as our second major task. This effort has been paid off and a sufficient understanding of the physics of ICRH has been obtained and is the key to the success of our experiment. This leads to the achievement of stable plasma condition and heating of ion temperature to 170 keV.

To make this system applicable to space propulsion the plasma has to be detached from the field lines after being exhausted through one end while the other end is closed or used for fueling. The dynamic property of the plasma for the open ended operation with fueling and exhaust are unknown. Two plasma detachment schemes have been proposed: One is the disconnection of magnetic field line , and the other is the injection of annular cold gas (a hot plasma exhaust surrounded by a layer of cold gas named as hybrid plume). Theoretical investigation on the understanding of the dynamic property of plasma exhaust has been an on-going effort since conceiving this concept in early 1980. The detachment of the plasma with the annual injection of gas has been found feasible. At present the experiment can not been done because the fueling and exhaust systems have not been implemented due to lack of funding. However, the thrust and mass flow-rate have been measured at the exit of the exhaust chamber and found to be in agreement with prediction. Therefore the next major task will the experimental demonstration of the plasma detachment.

Although the spacecraft system design and the analysis of engine perfomance in a model mission have never been part of our research program, we are fully aware of the importance of the system implementation. Therefore a scoping study of the system design and mission analysis based a assumed trip to Mars has been carried out. From this exercise we learned that this system is very competitive in terms of specific weight and trip time.

This device is very compact. It is only three meters in length and less than one meter in diameter. It is only one tenth of the size of the smallest fusion device [7] but at four time the field intensity. The machine parameters are shown in Table 1 and the system layout is shown in Figure 1. Although the device is much smaller than the fusion device, the needed experimental facility is as extensive as that for fusion research. The present size was chosen based on the minimum spaces needed for diagnostic purpose. In reality, the actual size can be much smaller. The system scoping study indicates that this device can deliver 10 MW of power which is large enough for a Mars mission.

Table 1: Device Parameters

Overall length	3.2 m
Central cell length	1.15 m
Central cell radius	0.36 m
Central cell field (Bc)	2.4 kG
Maximum field (Bmax)	20.0 kG
Plasma heating power:	
• ECRF	1.0 kW
• ICRF	1.0 MW

The experiments conducted on this device have shed new light on the dynamics of these high-power devices and their application to multimegawatt space propulsion. In the past years the successful ICRF heating of a mirror plasma has been demonstrated both theoretically and experimentally [8], [9]. Two types, I and II, of plasma discharges can be produced, with greater stability being obtained in type II at high magnetic fields. Plasma parameters nearly equivalent to those of large fusion devices have been obtained.

Further milestone accomplishments are the measurement of ion temperature, the measurement of thrust and mass flow-rate. The ion temperature is an important parameter because it determines both I_{sp} and thrust. The ion temperature has not been measured in any electric propulsion system. The radiation loss was found to be very low. The extracted efficiency was as high as 68% even though the rf transmitter was running at a deteriorated condition. At an I_{sp} of 12,852 s and power level of only 9.4 kW the thrust of 76 mN is a respectable value. Most important, these results fall within our prediction. These achievements are way ahead of the goals which we set out to accomplish.

The 10 MW class vehicle and MARS mission were chosen as the models for our flight system and mission analysis so that a comparison can be made with an established analysis for an ion engine. The design study of a 20 kW class Tandem Mirror Rocket based on the fuel cell or solar panel technology is underway. A direct comparison with MPD and Arcjet can then be made when such a system design is ready. The 10 MW class system study is comparable to the ion engine and is expected to show better performance when higher efficiency and lower weight are considered. In addition to high I_{sp} and efficiency, this rocket has the flexibility of being operated at either variable or constant I_{sp} and thrust. There is no electrode damage problem and the rocket can use any type of propellant.

Our future goal is to reach an efficiency as high as 90%. This expectation is reasonable because there is sufficient room for improvement as shown by our theoretical analysis. The newly accomplished theoretical analysis predicts that higher coupling efficiency can be obtained if the magnetic field is made more uniform and the plasma radius larger. At present, the ionization efficiency is very low because the microwave frequency is not in resonance with electron cyclotron frequency. The efficiency is expected to improve when the newly installed 14.5 GHz microwave transmitter becomes operational. These features will be implemented

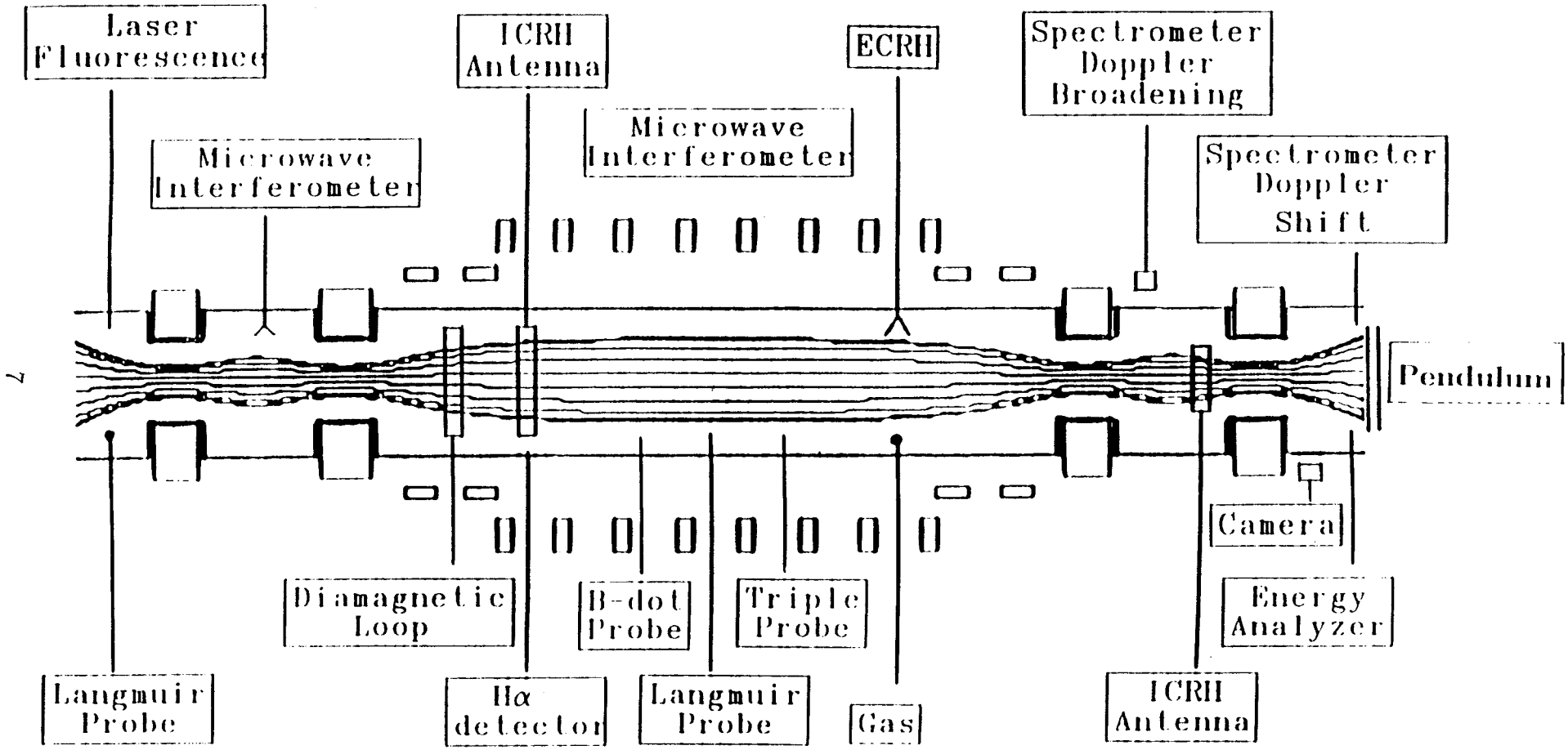

Figure 1. Experimental setup of the Tandem Mirror Plasma propulsion facility.

in our future experiment and will undoubtedly raise the efficiency. The weight for the power conditioning equipment was scaled linearly from a 1 MW system. Actually the specific weight will level off when the power increases. The frequency of the transmitter system used as basis for the system study is 100 MHz which is much higher than the 500 kHz to 10 MHz frequency needed for propulsion application. The weight of the power conditioning system will be much lighter at these frequencies. The projected specific weight can be reduced to as low as 6 kg/kW. These values are significantly lower than any known electric propulsion system.

To bring our system into the mainstream of electric propulsion programs, it is our wish to to move forward to carry out the experiment that will demonstrate the plasma detachment. However, such an experiment requires a major upgrade of our facility which is not realistic at the current funding level. We propose, instead, to carry out the experiments to improve the energy conversion efficiency and obtain the conditions for high thrust operation. The development of reliable plasma condition control is as important as the detachment. The detachment may become obvious at higher thrust (high density and low temperature).

The entire facility has been built and operated by graduate students, undergraduate students, part time staffs, and visiting scientists. Of the the entire facility only the mirror device was fabricated with the instrumentation fund from the Air Force and constitutes a very small fraction. The major components of the facility are surplus equipment. This project has made a very significant contribution to education. There are two graduate students earned their doctoral degrees based on their work on this project. In addition there have been four graduate students, five undergraduate students and even summer high school students working on this project. This project has been greatly benefited from the visiting scientists, two of them from the Institute of Physics of the Chinese Academy of Science in Beiging, one from the Southwestern Institute of Physics in Sichuan, China. They have helped in the construction of the facility, developed the laser fluorescence system, many probes, and the development of space bound solid state RF transmitter systems.

2 Summary of Progress

The progress made in the past year is summarized in the following subsections. To keep the discussion brief, only the key points will be given and details can be found in later sections.

2.1 Experimental Study

The experimental setup is shown in Figure 2. A wave is launched from a double-half-loop antenna located at the high field region of the central cell. The wave propagates radially inwards and toward the resonance midplane where the diagnostics are located. A 172 eV ion temperature, a 21.6 eV electron temperature and a $1.98 \times 10^{17}\mathrm{m}^{-3}$ plasma density are obtained from probe measurements. In addition, the absence of pronounced H_α lines in the Doppler broadening spectrometer confirms the expectation of a high degree of ionization and hence a relatively low power loss due to atomic excitation. Other important parameters can be extracted from these data and are included in Table 2. This operating point is shown in the performance graph of Figure 3 at the power level of 9.4 kW. From these data, the rf-to-plasma coupling efficiency is determined to be 68%.

Table 2: Plasma Parameters

T_i	Measured ion temperature	172 eV
T_e	Measured electron temperature	21.6 eV
n_e	Measured plasma density	$1.98\times10^{17}m^{-3}$
τ	Extracted energy confinement time	50 μ s
P_{in}(rf)	Extracted input rf power	9.4 kW
P_{in}(microwave)	Extracted input microwave power	0.3 kW
P_{absorb}(ion)	Power absorbed by the ions n_ek $T_i V_p$	5.2 kW
P_{absorb}(electron)	Power absorbed by the electrons n_ek $T_e V_p$	0.69 kW
$P_{exhaust}$	Power flows into the exhaust chambers	0.5 kW
ξ	Coupling efficiency	68%
I_{sp}	Extracted specific impulse	12,852 s
$\dot{m}$	Mass flow-rate	0.1 mg
Thrust	Measured	76 mN

Resource limitations have prevented us from operating in the streaming-plasma mode. This capability requires that a vacuum interface to the large vacuum tank in our laboratory be manufactured and the design and manufacture of a propellant injector. Two additional magnet power supplies are required to run the system asymmetrically. These system enhancements are necessary to perform the plasma detachment experiment.
Nevertheless, rapid progress has been made in the understanding of both the plasma and neutral components in the exhaust. The tandem mirror is operated at a mirror ratio of 10 and the plasma is well confined. Any exhaust plasma is the result of the loss-cone effect and is only 20% of the central density. However, this axial loss plasma shows no drop in

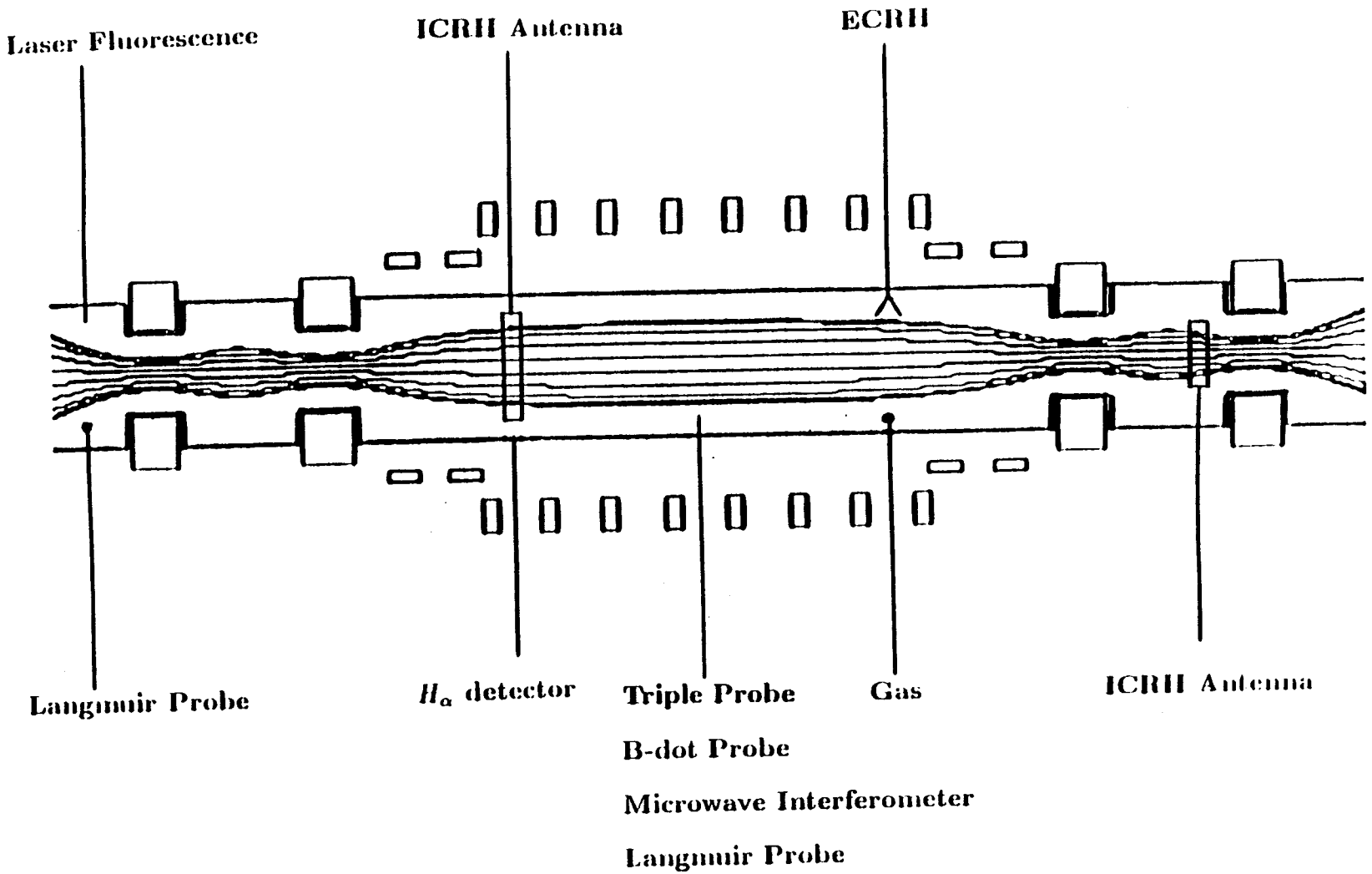

Figure 2: ICRF Wave experimental layout

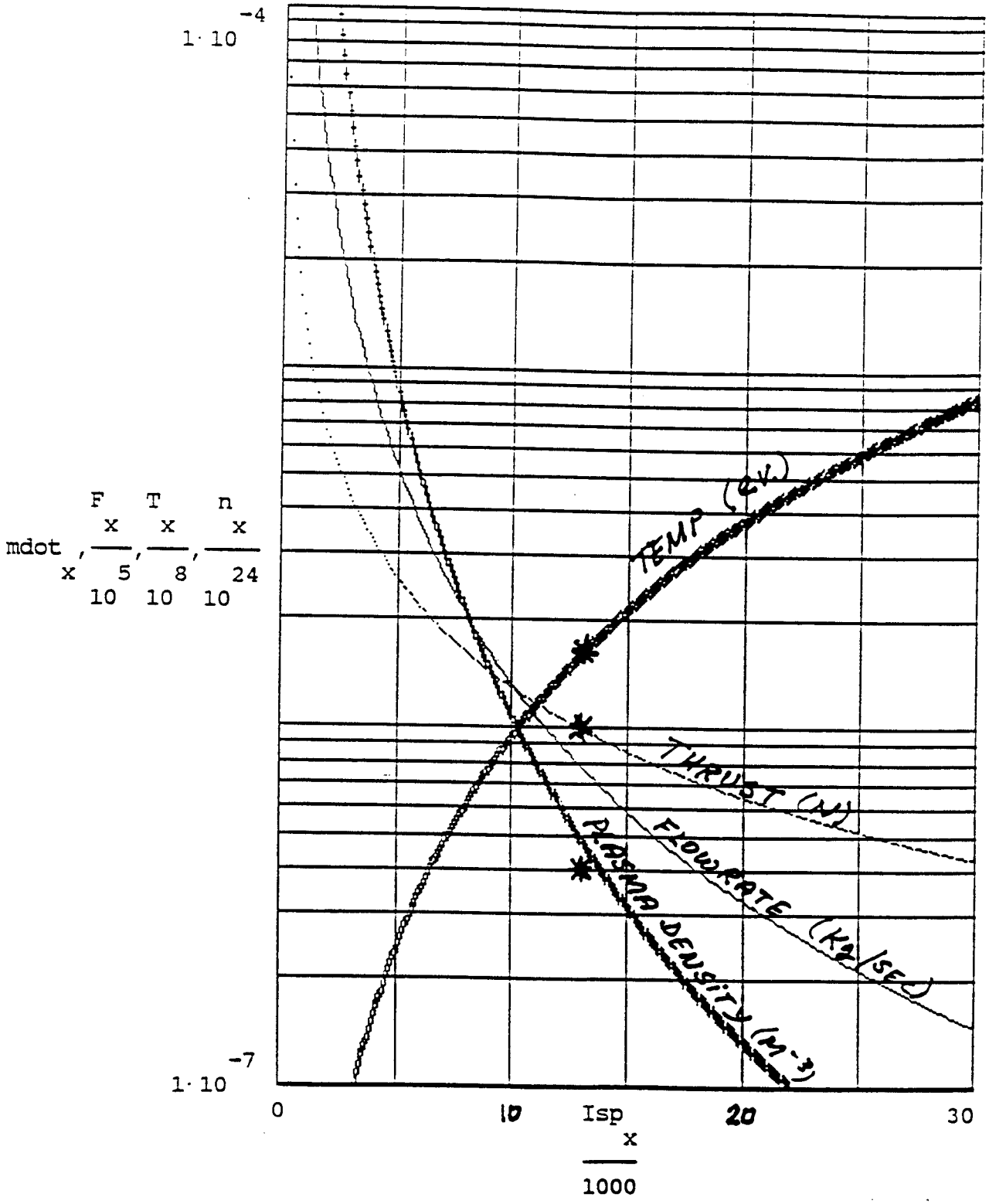

Figure 3: Overlay of the experimental data with performance projection

temperature from that of the central cell. Radially, both density and temperature profiles are nearly flat suggesting no loss of efficiency due to profile effects. A laser fluorescence system is now operating to measure neutral density. The system utilizes a new two-optical-path fluorescence signal reduction method developed by our group[10]. The radial profile of the neutral density in the exhaust has been measured. The results show a hollow profile, peaking near the edge and dropping to negligible values on axis. This phenomenon agrees with our earlier prediction that the wall is insulated by neutrals. The density in the exhaust will match that of the central cell when the device is operated in the streaming-plasma mode.

Two independent thrust measurement methods are being developed: a grid energy analyzer to measure ion axial energy from which the plasma velocity and thrust distribution can be determined, and a ballistic balance to measure total thrust. The former method requires a sweeping power supply or amplifier which has been acquired and will be ready for the future experiment. The ballistic balance has been successfully used to measure the the thrust of this device. The sensitivity of the balance is better than 0.1 mN. The measured thrust at exhaust is given in Table 2. The description of the ballistic balance are given in section 4.

The Doppler broadening measuring instrument is a monochromatic spectrometer fitted with a fast rotating mirror in the optical path. The system was developed in the past few years and has become operational recently. A resolution as high as 0.5 Angstrom has been achieved. However, we have difficulty in making measurement because the radiation was found to be extremely weak. This is a strong indication of low radiation losses from the plasma.

2.2 Theoretical Analysis

As has been reported in the past, the experimental effort was guided by sound theoretical predictions. The early theoretical work was the development of the numerical simulation BEACH code [8]. In the past year an analytical solution of ICRF wave propagation in an axially inhomogeneous cylindrical plasma has been undertaken[9]. The main result of this work has been the development of the code CYLWAVE. This new tool allows us to carry out some parameter scans which can not be done with numerical simulation. The results reveal two important points. First, the behavior of the plasma impedance as a function of the mirror ratio is in good agreement with the resonance volume theory. This theory simply states that the dissipation is proportional to the volume of plasma that is close to the resonance. Second, optimal power coupling to the plasma is obtained with the resonance located directly underneath the rf antenna or at the machine midplane. These findings provide appropriate design guidelines which favor machines providing a large plasma volume in a uniform magnetic field at the ion cyclotron resonance.

The results obtained for the slab geometry show that the efficiency $\mathcal{F}$ increases as resonance is approached. In other words, large wave power is dissipated or the wave is damped.

These theoretical predictions agree with preliminary experimental results of the axial B_z profile as have been reported previously.

These results will guide our future experiments even though many hardware modifications will have to be made in order to implement the new features.

2.3 Flight System Study

A flight system design study has been undertaken (postulating a piloted Mars mission at 10 MWe and 50% efficiency)[11]. The preliminary results are very attractive. The overall specific weight of a 10 MW flight system is only 8 kg/kW using an existing space nuclear electric system design. Initial calculations performed recently for our group by J. Gilland and C. Hack of NASA/Lewis [12] indicate an attractive 150 day transit to MARS. The total trip time is 480 days including a 90 day stay on MARS. The calculations used an input value of 8 kg/kW and an efficiency of 50%. Since then, experimental results and hardware design modifications have allowed us to refine the subsystem specific weight estimates, as well as to consider a more realistic efficiency value of 70%.

3 Theoretical Analysis

The effort of the theoretical work is to obtain much more rigorous treatment of the ICRF wave propagation than previously reported. The true geometry can be considered in numerical simulations, but the physical insight is difficult to extract. The functional dependence of the wave dissipation on the plasma parameters can be formulated analytically only after many simplified assumptions are made. Notwithstanding these simplifications building upon the relatively crude analytical solution of slab and cylindrical models which was presented previously [6]. The refined analysis of both models was undertaken and the results of the slab model is discussed in the following.

3.1 Analytical Study

3.1.1 Slab Model

The analysis of wave propagation in the slab geometry is much simpler than that in the cylindrical geometry and can provide information on the coupling efficiency of ICRF power to plasma. The detailed analysis will be given in reference [13]. A figure of merit was defined as the dissipated power divided by the source power as given by the incident Poynting Flux. Since for the majority of the cases, $\omega - \Omega_i \gg \nu_i$, the much simplified $\mathcal{F}$ is obtained

$$\mathcal{F} = 2\cos\theta_T \left(\frac{\Omega_i}{\omega_{pi}}\right) \left[\frac{\cos^2\theta_I}{(\cos\theta_I + \frac{k_0}{k_{pl}}\cos\theta_T)^2 + \frac{D^2}{(S^2-D^2)^2}\sin^2\theta_I}\right] \tag{1}$$

where $\theta_{I,T}$ are the incident and transmitted angles of the power flux and are defined as

$$\begin{aligned} \theta_I &\equiv \cos^{-1}\left(\tfrac{k_x}{k_0}\right) \\ \theta_T &\equiv \cos^{-1}\left(\tfrac{k_{xB}}{k_{pl}}\right) \end{aligned}$$

where

$$\begin{aligned} k_{pl}^2 &\equiv k_0^2 \frac{S^2 - D^2}{S} \\ k_{xB}^2 &= k_0^2 \frac{S^2 - D^2}{S} - k_y^2 \end{aligned}$$

We will examine the following two important limits:

1. Resonance limit ($\omega \to \Omega_i$)

   In this limit, it is seen that $S, D \to \infty$. This allows the dropping of the last term in the denominator. It is also seen that $\cos\theta_T \simeq 1$, and $k_{pl} \gg k_0$. This results in the

$$\mathcal{F} = \sqrt{\frac{S_{Re}}{S_{Re}^2 - D_{Re}^2}} \tag{2}$$

   Since $S_{Re} \simeq 1$, $D_{Re} \simeq 0$ in the limit of resonance, it can be shown that the efficiency $\mathcal{F}$ approaches a maximum of 1 when resonance is approached.

2. Far from the Resonance Limit ($\omega \gg \Omega_i$, $\omega \ll \Omega_i$)

   For frequencies far away from resonance, the value of the efficiency can be given by the same equation as before (Equation 2). However, the simplification of

$$\sqrt{\frac{S_{Re}}{S_{Re}^2 - D_{Re}^2}} \simeq \left(\frac{\Omega_i}{\omega_{pi}}\right) \tag{3}$$

   can still be made. This results in an efficiency of

$$\mathcal{F} \simeq \left(\frac{\Omega_i}{\omega_{pi}}\right) \cos\theta_T \tag{4}$$

   Since for our range of frequencies, $\Omega_i \ll \omega_{pi}$, for frequencies off resonance, the efficiency approaches zero.

The results obtained for the slab geometry show that $\mathcal{F}$ increases as resonance is approached. In other words, large wave power is dissipated or the wave is damped. These theoretical predictions agree with preliminary experimental results of the axial B_z profile.

3.1.2 Cylindrical Model

Purpose of Study – The purpose of this study is to examine the problem of ICRF wave propagation in an axially inhomogeneous cylindrical plasma-vacuum system. A new method of solving this complicated problem is proposed and carried out.

An analysis of ICRF propagation in an axially-inhomogeneous cylindrical plasma-vacuum system is undertaken. Due to the conservation of the flux embedded in the plasma, the radius of the plasma cylinder changes with the varying axial magnetic field as

$$\Phi \propto R^2(z)B(z) = R_0^2 B_0 \qquad \Rightarrow \qquad R(z) = R_0\sqrt{\frac{B_0}{B(z)}}$$

Because of this nonconstant plasma-vacuum interface $R(z)$, matching boundary conditions across the plasma-vacuum interface poses a major problem. The traditional (r, z) cylindrical geometry is transformed into a new geometry (ρ, ξ) which is selected to facilitate the matching of the boundary condition and to simplify the form of the plasma field equations. The new variables ρ and ξ are defined as

$$\rho \equiv \frac{r}{R(z)} \qquad ; \qquad d\xi \equiv \frac{dz}{R(z)}$$

In this new coordinate system, the boundaries are located at

- $\rho = 1$: Plasma-vacuum interface.
- $\rho = \kappa$: Conducting wall.

This new coordinate system (ρ, ξ) has a much simpler boundary at the plasma-vacuum boundary $(\rho = 1)$ as opposed to the varying radius of the plasma-vacuum interface $r = R(z)$ of the (r, z) coordinate system. The new (ρ, ξ) geometry includes a conducting wall with a radius that changes in proportion to the plasma column radius. This is not an unrealistic assumption since the vacuum chamber necks down near the B-field maximum in most mirror machines in order to locate the magnets closer to the plasma.

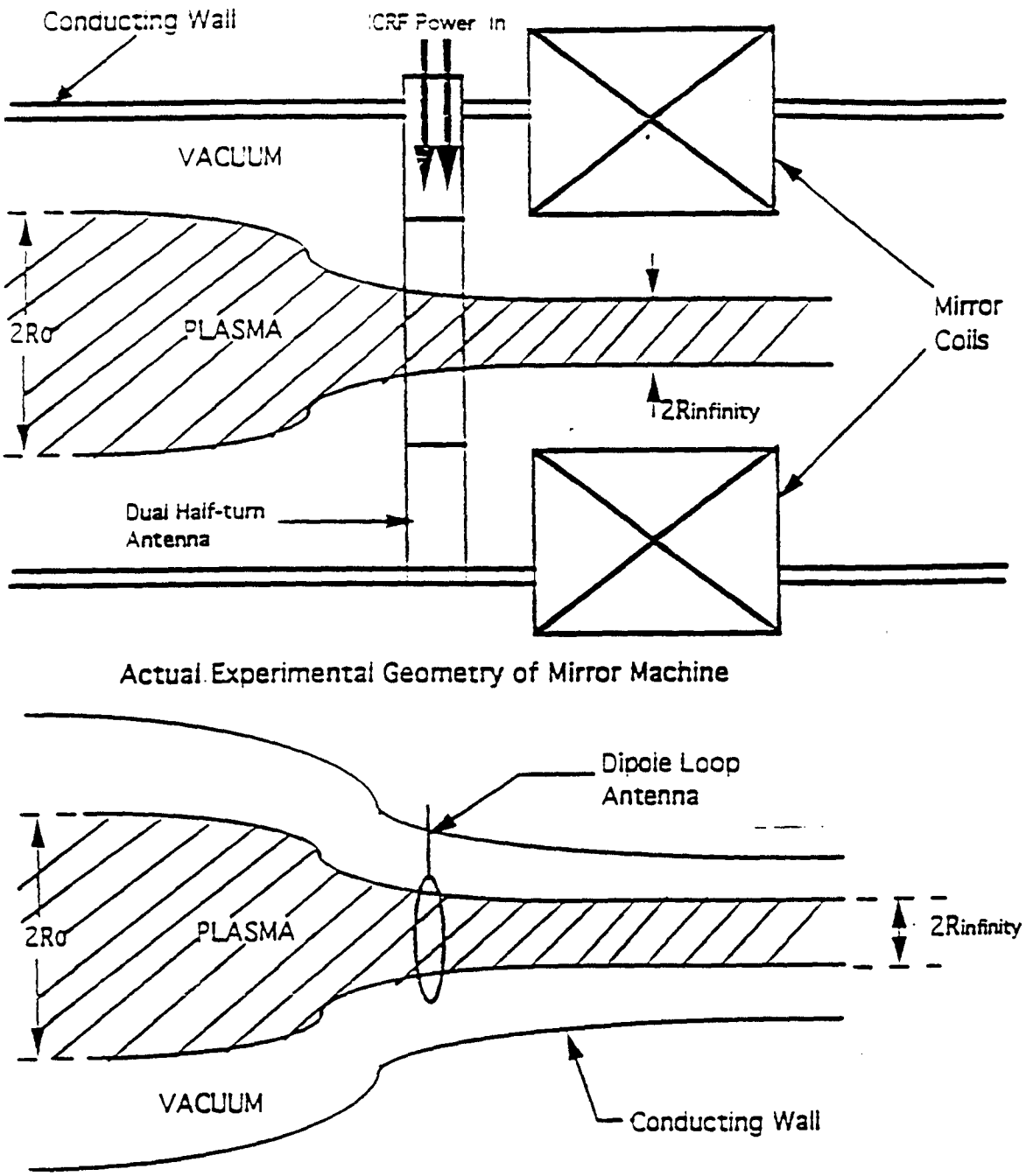

Figure 4: Geometry of the Cylindrical Plasma-Vacuum System. An experimental geometry (The MIT Tandem Mirror Rocket) is shown schematically at top, the model geometry used in the analytical theory is shown at bottom. The source antenna is a dual half-turn loop for the MIT PPEX experiment and a dipole loop for the model.

The steps taken in the solution of the EM fields in this inhomogeneous medium are as follows:

1. Solve for source fields generated by dipole loop in vacuum. A complete solution, i.e. both coefficient and functional dependence of the fields is possible because the source term is known.

2. Solve for the full vacuum fields

3. Starting from Maxwell's equations and assume the following

   (a) $m = 0$. Only axisymmetric mode is considered.

   (b) $E_z \ll E_\theta$, E_r. This assumes that the E_z field is of order ϵ lower than E_θ or E_r, where $\epsilon = m_e/m_i$.

   (c) Constant radial density profile (skin current model). A macroscopic (non-RF) surface current is assumed to exist on the plasma-vacuum boundary. This surface current generates an MHD pressure balance [14] that can support a radially constant density.

   (d) Slow-z approximation. The magnetic field is assumed to be a slowly varying function of z. This means that $k_y \sim k_z \sim 1/a \gg 1/L_B$, where k_y is the transverse wave number of the ICRF waves, k_z is the axial wave number, a the radius of the plasma, and and L_B is the axial scale length of the magnetic field. This assumption simplifies the cross-coupling terms in ρ and ξ in the differential equations.

From these assumptions, one can derive two sets of coupled differential equations linking ϕ_p and χ_p, where $E_\theta \equiv i\omega\phi_p/r$, $E_r \equiv i\omega\chi_p/r$, and $B_z = i\omega\phi_p'/r$ are the RF electric and magnetic fields in plasma.

$$\frac{\partial^2}{\partial\xi^2}\chi_p + k_0^2 K_1(\xi)R^2(\xi)\chi_p + k_0^2 K_2(\xi)R^2(\xi)\phi_p = 0 \tag{5}$$

$$\frac{\partial^2}{\partial\xi^2}\phi_p + \rho\frac{\partial}{\partial\rho}\frac{1}{\rho}\frac{\partial}{\partial\rho}\phi_p + k_0^2 R^2(\xi)K_1(\xi)\phi_p - k_0^2 R^2(\xi)K_2(\xi)\chi_p = 0 \tag{6}$$

where $R(\xi)$ is the plasma radius as a function of ξ and $K_1(\xi)$ and $K_2(\xi)$ are elements of the dielectric tensor $\underline{\underline{K}}$ where

$$\nabla \times \vec{E} = \frac{-i\omega}{c^2}\underline{\underline{K}} \cdot \vec{E} \quad ; \quad \underline{\underline{K}} \equiv \begin{bmatrix} K_1 & K_2 & 0 \\ -K_2 & K_1 & 0 \\ 0 & 0 & K_3 \end{bmatrix}$$

4. The coefficients of the differential equation $K_{1,2}(\xi)R^2(\xi)$ can be decomposed into three parts: its value as $\xi \to \infty$, its resonance-pole contribution, and a smooth portion, i.e.

$$K_1(\xi)R^2(\xi) \equiv S_\infty + \underbrace{S_{sub}(\xi)}_{\text{resonance pole}} + \underbrace{S_{sm}(\xi)}_{\text{smooth portion}}$$

Likewise

$$K_2(\xi)R^2(\xi) \equiv -i\left[D_\infty + \underbrace{D_{sub}(\xi)}_{\text{resonance pole}} + \underbrace{D_{sm}(\xi)}_{\text{smooth portion}}\right]$$

5. The functional dependence of the Resonance Pole term is selected to be

$$\mathcal{R}_{sub} = \frac{1}{(1+\epsilon c_{11})\hat{f}_0'\hat{\xi} + i\epsilon(1+c_{12}\epsilon)} + \frac{1}{(1+\epsilon c_{21})\hat{\hat{f}}_0'\hat{\hat{\xi}} + i\epsilon(1+c_{22}\epsilon)}$$

where

$$\hat{\xi} \equiv \xi - \xi_\alpha$$
$$\hat{\hat{\xi}} \equiv \xi + \xi_\alpha$$
$$\hat{f}_0' \equiv f_0'(\xi = +\xi_\alpha)$$
$$\hat{\hat{f}}_0' \equiv f_0'(\xi = -\xi_\alpha)$$
$$f_0(\xi) \equiv \left(1 - \frac{R_\alpha^4}{R^4(\xi)}\right)$$

where R_α is the radius of the resonance layer of plasma. Note that $\mathcal{R}_{sub}$ has two components. The first component is for the subtraction of the pole at $\xi = \xi_\alpha$, while the second component treats the pole at $\xi = -\xi_\alpha$.

6. Assume a Bessel-type radial solution and perform a Fourier transform on ϕ.

$$\rho\frac{\partial}{\partial\rho}\frac{1}{\rho}\frac{\partial}{\partial\rho}\phi_p = -\alpha^2\phi_p$$

Solving this yields the functional form for ϕ

$$\phi(\rho, k_\xi) = \phi(\alpha, k_\xi)\rho J_1(\alpha\rho)$$

7. Boundary condition. Application of the continuity of fields at the plasma-vacuum boundary ($\rho = 1$) yields the following for $\phi(\alpha, k_\xi)$.

$$\phi_p(\alpha, k_\xi) = \frac{1}{\alpha J_0(\alpha) - J_1(\alpha)\frac{\frac{\partial}{\partial\rho}\hat{F}}{\hat{F}}}\left[\frac{\partial}{\partial\rho}\hat{G} - \frac{\frac{\partial}{\partial\rho}\hat{F}}{\hat{F}}\hat{G}\right]_{\rho=1} \tag{7}$$

where

$$F(\rho, k_\xi) \equiv \frac{\rho \triangle_{\kappa\rho}}{K_1(k_\xi \kappa)} \tag{8}$$

$$G(\rho, k_\xi) \equiv -\left(\frac{\rho}{\kappa}\right) \frac{K_1(k_\xi \rho)}{K_1(k_\xi \kappa)} \hat{\Psi}_{wire}(\kappa, k_\xi) + \hat{\Psi}_{wire}(\rho, k_\xi) \tag{9}$$

$$\triangle_{\kappa\rho} \equiv K_1(k_\xi \kappa) I_1(k_\xi \rho) - I_1(k_\xi \kappa) K_1(k_\xi \rho) \tag{10}$$

It is seen that ϕ is completely determined from Equation 7 since the source fields Ψ_{wire} is completely known.

8. Perform a Fourier transform in ξ on the two coupled differential equations in ϕ_p and χ_p. The Fourier transform of the resonance pole S_{sub} and D_{sub} are performed using residue calculus to transform the $\mathcal{R}_{sub}$ analytically. The smooth term S_{sm} and D_{sm} are transformed first by curve fitting them with a given function in ξ, minimizing the error in the curve fit by adjusting some coefficients, then Fourier transforming the curve fitting function analytically.

   The resulting equations contain convolution integrals because of the ξ dependence of the coefficients S_{sm}, S_{sub}, D_{sm} and D_{sub}.

$$-k_\xi^2 \hat{\chi}_p(\alpha, k_\xi) + k_0^2 \left\{ \begin{array}{l} +\int \left[\tilde{S}_{sm}(k_\xi - k'_\xi) + \tilde{S}_{sub}(k_\xi - k'_\xi)\right] \hat{\chi}_p(\alpha, k'_\xi) dk'_\xi \\ -i \int \left[\tilde{D}_{sm}(k_\xi - k'_\xi) + \tilde{D}_{sub}(k_\xi - k'_\xi)\right] \hat{\phi}_p(\alpha, k'_\xi) dk'_\xi \\ +S_\infty \hat{\chi}_p(\alpha, k_\xi) \\ -iD_\infty \hat{\phi}_p(\alpha, k_\xi) \end{array} \right\} = 0$$

$$(-k_\xi^2 - \alpha^2) \hat{\phi}_p(\alpha, k_\xi) + k_0^2 \left\{ \begin{array}{l} +\int \left[\tilde{S}_{sm}(k_\xi - k'_\xi) + \tilde{S}_{sub}(k_\xi - k'_\xi)\right] \hat{\phi}_p(\alpha, k'_\xi) dk'_\xi \\ +i \int \left[\tilde{D}_{sm}(k_\xi - k'_\xi) + \tilde{D}_{sub}(k_\xi - k'_\xi)\right] \hat{\chi}_p(\alpha, k'_\xi) dk'_\xi \\ +S_\infty \hat{\phi}_p(\alpha, k_\xi) \\ +iD_\infty \hat{\chi}_p(\alpha, k_\xi) \end{array} \right\} = 0$$

9. Finite differencing the two coupled differential equations yields

$$-k_j^2 \chi_j^m + k_0^2 \left[\sum_l S_{j-l} \chi_l^m \triangle k_l - i \sum_l D_{j-l} \phi_l^m \triangle k_l\right] + k_0^2 \left(S_\infty \chi_j^m - iD_\infty \phi_j^m\right) = 0 \tag{11}$$

$$-(k_j^2 + \alpha_j^2) \phi_j^m + k_0^2 \left[\sum_l S_{j-l} \phi_l^m \triangle k_l + i \sum_l D_{j-l} \chi_l^m \triangle k_l\right] + k_0^2 \left(S_\infty \phi_j^m + iD_\infty \chi_j^m\right) = 0 \tag{12}$$

where

$$k_j \equiv k_\xi \quad ; \quad k_l \equiv k'_\xi$$

$$\chi_j^m \equiv \chi_p(\alpha^m, k_\xi)$$

$$\phi_j^m \equiv \phi_p(\alpha^m, k_\xi)$$

$$S_{j-l} \equiv \left[\tilde{S}_{sm}(k_\xi - k'_\xi) + \tilde{S}_{sub}(k_\xi - k'_\xi)\right]$$

$$D_{j-l} \equiv \left[\tilde{D}_{sm}(k_\xi - k'_\xi) + \tilde{D}_{sub}(k_\xi - k'_\xi)\right]$$

The two coupled difference equations could be written as two sets of matrix equations.

$$\underline{\underline{A}}_1(\alpha) \cdot \underline{\chi} = \underline{B}_1(\alpha)$$

$$\underline{\underline{A}}_2(\alpha) \cdot \underline{\chi} = \underline{B}_2(\alpha)$$

They are then solved simultaneously to yield an α for each k_ξ as well as χ. The ϕ is solved directly from the boundary conditions. These are then inverse Fourier transformed to return the ICRF fields E_r, E_θ, and B_z.

10. A figure of merit is selected as the antenna impedence. R_{pl}. This is found by

$$P_{abs} = \frac{1}{2} I^2 R_{pl} = \frac{1}{2} \mathrm{Re} \int \vec{E} \cdot \vec{J}^* dV$$

which is the volume integrated absorbed power. This figure of merit can then be maximized for different field and plasma conditions.

A code, CYLWAVE, is written in order to implement the theoretical analysis detailed above. The computed ICRF B_z from CYLWAVE for a resonance-in-chamber case is plotted on Figure 5. It is seen that the ICRF waves decay very quickly after leaving the launching antenna. For a Resonance-out-of-chamber case seen on Figure 6, it is seen that the absence of a resonance results in more oscillations and larger field amplitudes after the ICRF waves are launched from the antenna.

A mirror ratio scan is performed in order to calculate the mirror ratio for the optimum wave-plasma coupling. The plasma impedence R_{pl} at different mirror ratios is plotted on Figure 7. The behavior of the R_{pl} as a function of the mirror ratio is in good general agreement with the resonance volume theory, which simply states that the dissipation is proportional to the volume of plasma that is close to resonance.

The behavior of the antenna-plasma coupling impedence as a function of resonance location is also performed. The resulting R_{pl} versus ξ_{res} is plotted on Figure 8. The coupling impedence is seen to peak in two locations – resonance at plasma center, and resonance directly underneath the antenna. In fact, the resonance-under-antenna case shows peak in plasma loading impedence that is just as large as the resonance-at-center case. This indicates that, depending on the mirror ratio, locating the resonance close to the antenna may be just as important for coupling as locating the resonance at the plasma center. Thus an optimum coupling condition, from a wave-propagation point of view, would be to have the resonance located either directly underneath the antenna or at the center of the machine.

It must be noted here that the analytical study described here has two significant advantages over other studies. First, the axial inhomogeneity and cylindrical geometry are both treated in a consistent manner in the analysis, and secondly, the subtraction of the resonance pole performed in this study allows the ICRF waves to propagate up to and through the resonance. These advantages demonstrate the power of this method of analysis.

As summary of this analysis we can draw the following conclusion: A high coupling efficiency can be obtained if: (1) The magnetic filed is made as uniform as possible; (2) The rf frequency is in resonance with ion cyclotron frequency at minimum field; and (3) The coupling efficiency increases with plasma radius. This will lead our future experiment.

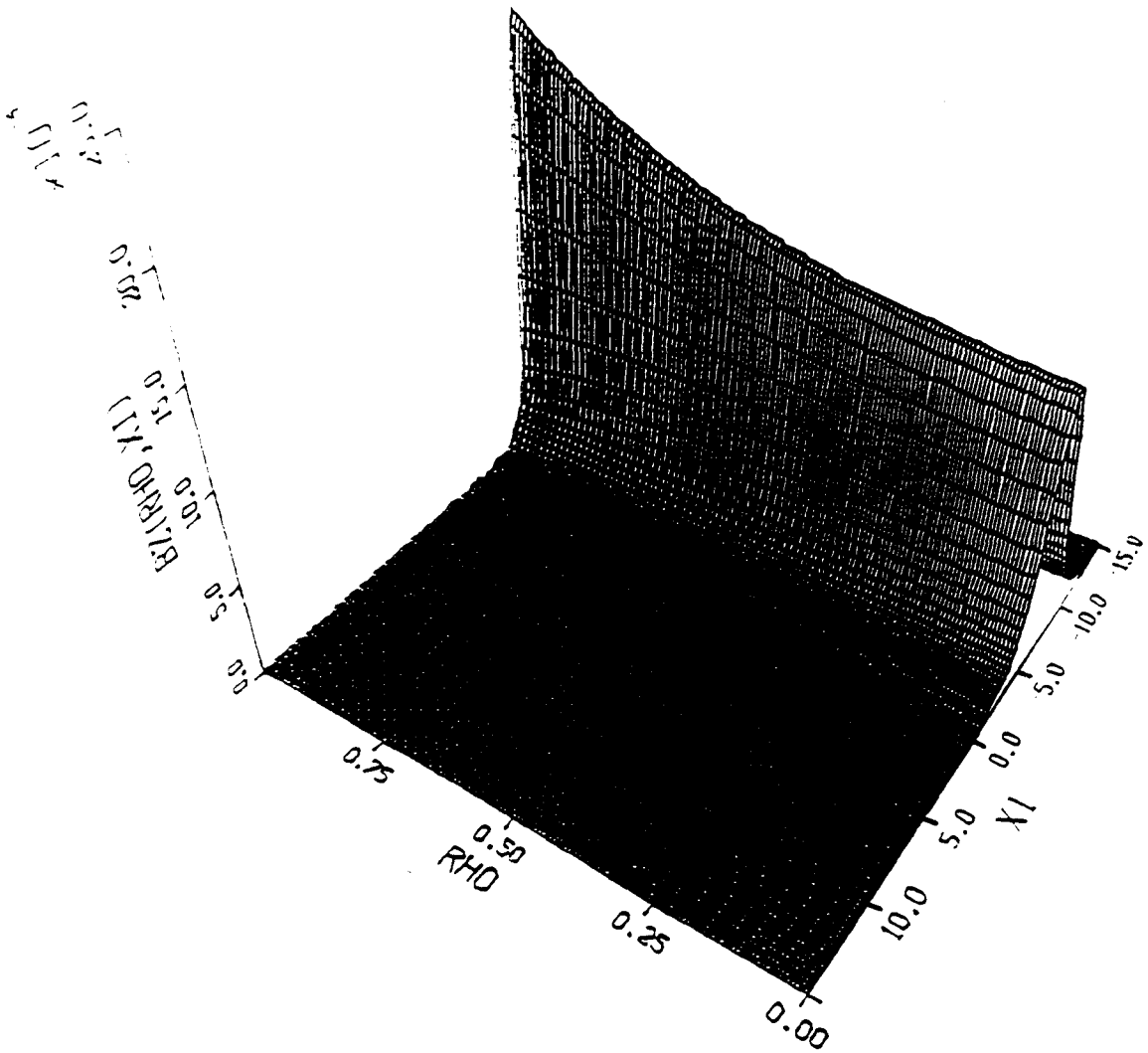

Figure 5: ICRF B_z plot as function of (ρ, ξ). Waves are launched from dipole loop antenna located at $\rho = 1.397$, $\xi = -5.00$. For this case, ICRF resonance location is located IN the chamber at $\xi = \pm 0.977$. 65 k_ξ spectral points were taken to generate this profile. The geometry is $R_0 = 0.77a$, $R_\infty = 0.5a$, where a is the radius of the wire loop antenna.

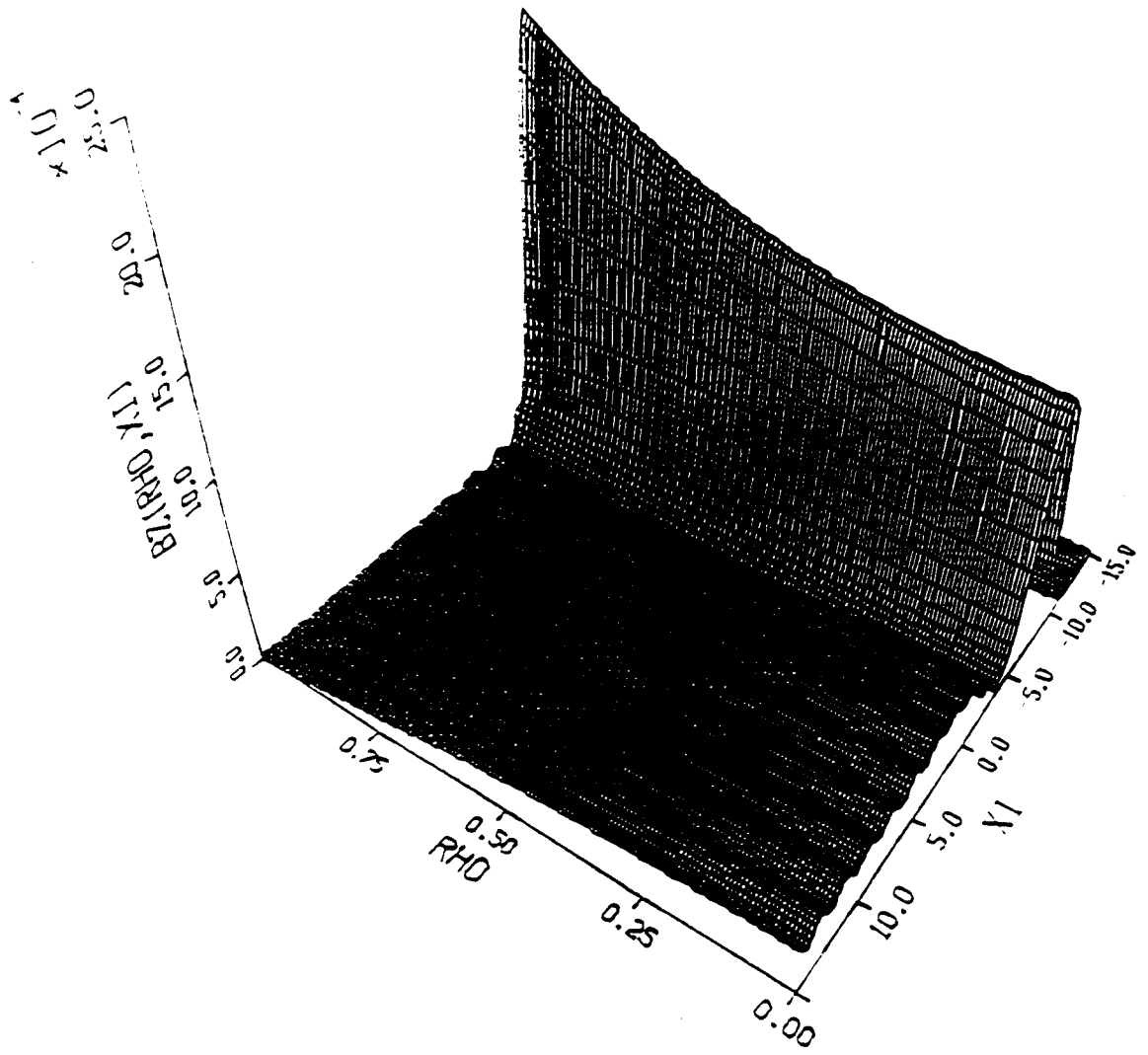

Figure 6: ICRF B_z plot as function of (ρ, ξ). Waves are launched from dipole loop antenna located at $\rho = 1.397$, $\xi = -5.00$. For this case, ICRF resonance location is located OUTSIDE the chamber 65 k_ξ spectral points were taken to generate this profile. The geometry is $R_0 = 0.77a$, $R_\infty = 0.5a$, where a is the radius of the wire loop antenna.

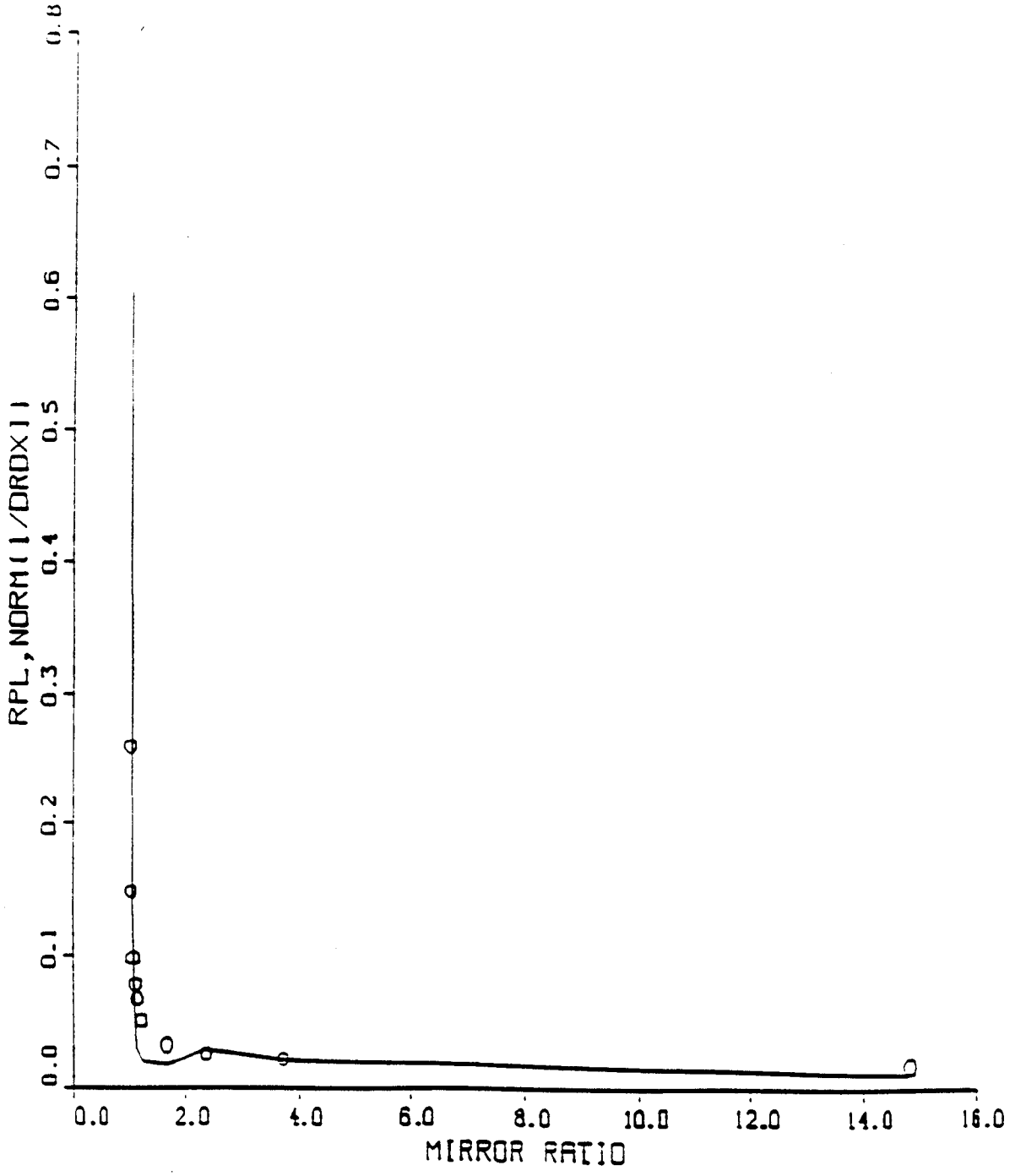

Figure 7: Plasma Impedence R_{pl} (Solid line) and Normalized Resonance-volume (Open Circle Line) calculations performed for different mirror ratios. Plasma parameters are: $n_e = 1.0 \times 10^{11} cm^{-3}$, $T_e = 10\text{eV}$.

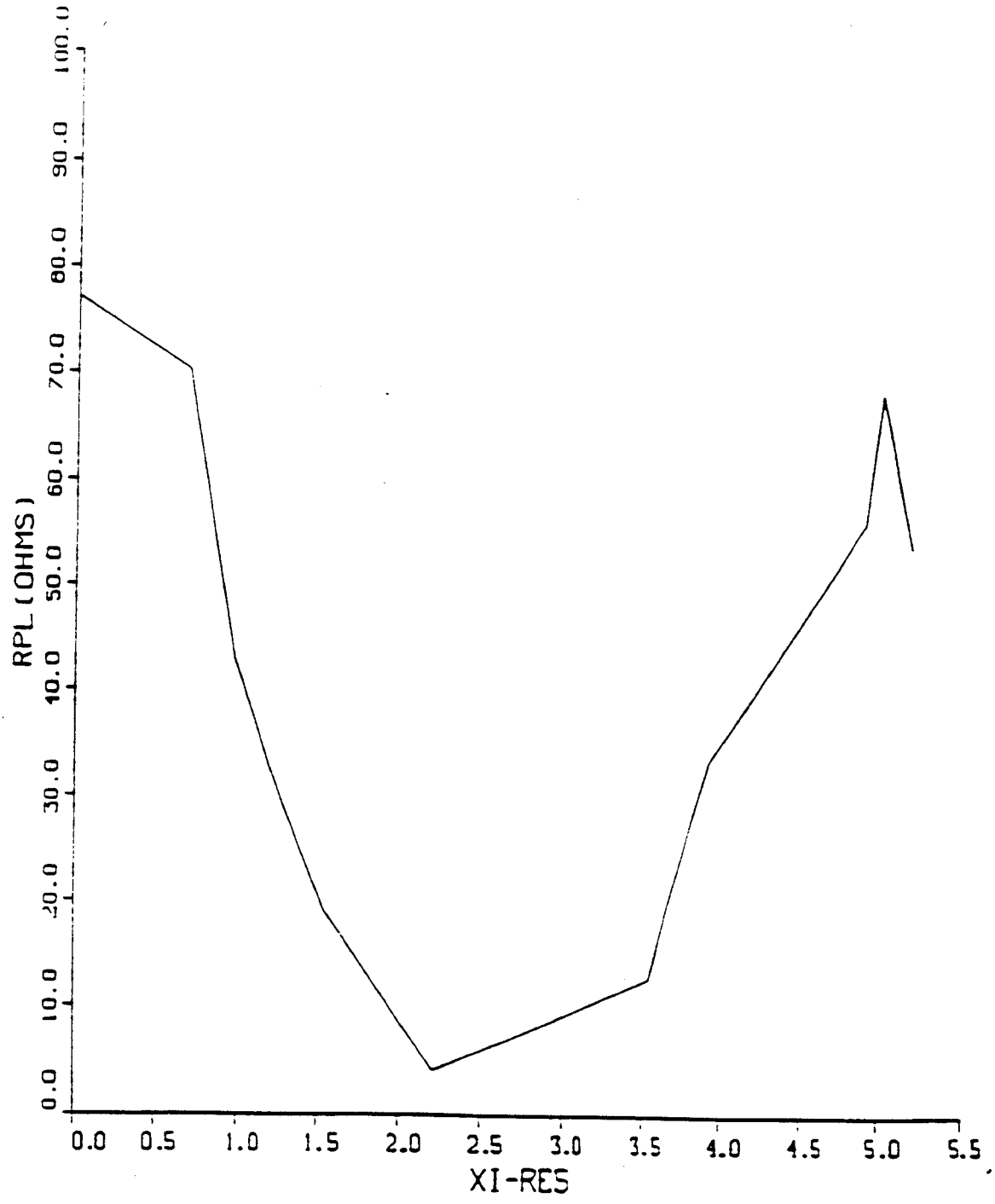

Figure 8: Plasma Impedence R_{pl} versus resonance location ξ_{res}. Plasma parameters are: $n_e = 1.0 \times 10^{11} cm^{-3}$, $T_e = 10$eV. Note that the peaks in R_{pl} are located at $\xi = 0$ field minimum, and $\xi = 5.00$ antenna location.

3.2 Computational Study

Although the analytical treatment of the previous section yielded intuitive results of the dependence of P_{abs} on plasma parameters, it nevertheless is too simplified a treatment to apply to a real system. The main simplifications that were made in the analytical treatment was the use of only one eigenmode and homogeneous magnetic field. A typical solution that proved to be useful requires the solution of about 30–50 modes which, upon summation, form the resulting field solutions.

The goal of this computational analysis is to provide a better modeling of the wave-plasma coupling problem than the simplified results of the analytical solution. However, this computational analysis is not simply a purely numerical simulation. Much analytical work is done to reduce the fields to functional form , i.e. $I_n(k_r r)$, $K_n(k_r r)$, $J_n(k_{\perp 1} r)$ before the numerical "number-crunching" is handed over to the codes.

The BEACH code extends the analytical approach taken in the cylindrical geometry solution of the previous section. It solves for the ICRF wave propagation in an inhomogeneous axial magnetic field. The inhomogeneous axial geometry is handled by separating the axial length into discrete axial "slices", each of which contains a homogeneous axial magnetic field.

The code first finds the eigenmodes that exist in each axial slice by satisfying both the infinite plasma dispersion relation and the boundary conditions. The boundary condition of the plasma–vacuum system can be written as:

$$c_1 H_p + c_2 E_p = e_1 J_\phi \tag{13}$$

$$c_3 H_p + c_4 E_p = e_2 J_\phi \tag{14}$$

The solution to the above are:

$$H_p = \frac{(e_1 c_4 - e_2 c_2)}{D} J_\phi \tag{15}$$

$$E_p = \frac{(e_2 c_1 - e_1 c_3)}{D} J_\phi \tag{16}$$

$$D = c_1 c_4 - c_2 c_3 \tag{17}$$

The term D is then the boundary condition of the bounded plasma–vacuum system. Solving this boundary condition coupled with the dispersion relation

$$S k_\perp^4 + k_\perp^2 [k_z^2 (S + P) - k_0^2 (SP + RL)] + P(k_z^2 - k_0^2 R)(k_z^2 - k_0^2 L) = 0 \tag{18}$$

yields the eigenmodes of the cylindrical system.

After solving for the eigenmodes of the system, the code then computes the excitation coefficients of the initial axial slice as driven by the source term (Antenna). The excitation coefficient of the next axial slice can then be determined by imposing two conditions of continuity on the boundary between the two axial slices: conservation of the integrated axially propagating Poynting Flux $\int \vec{S}_z r dr$, and the continuity of wave phase. These two conditions uniquely determine the excitation coefficients of the different eigenmodes in the next axial slice. This analysis is then performed for all axial slices.

Computational analysis was performed on two types of plasma regimes:collisionless cold Plasma, and collisional cold plasma. Different physics are inherent in each different regime.

3.2.1 Collisionless

Initially, the calculations of the ICRF field propagation were performed using a cold, collisionless plasma model. This ensures that there exist no complex k_z roots that could damp out the axially propagating Poynting Flux, thus enabling a good check of the model's ability to conserve power and basic phsical insight. Because there is no dissipation mechanism (Cold plasma, no collisions), some effects are expected physically from this simple propagation.

Several different antenna geometries are used to launch different modes. The two antenna geometries that were studied were the FULL TURN LOOP(FTL) and DUAL HALF TURN LOOP(DHTL). The baseline model is driven by a Full Turn Loop (FTL) antenna. Because it is symmetric in θ, the full turn loop antenna excites only the n=0 mode.

The solution of the dual half turn loop (DHTL) geometry poses a more difficult problem than the full turn loop (FTL) solution. The main difference between the DHTL and the FTL lies in the $\vec{J}(k_z)$ driving term, specifically the radial feeders. This is different from the Full Turn Loop (FTL) geometry in which the contribution from the radial feeders cancel out (Since one leg is entering and the other is exiting, net J_r is zero). The modelling of the driving term $\vec{J}(k_z)$ for the DHTL is detailed in a full report in preparation.

The wave propagation of both type of antenna is quite similar. Figures 9 and 10 show the propagation characteristics of the ICRF B_z and E_z fields as the waves propagate from the launch point (z=0) towards the resonance at mid-plane. The results that are readily observable from this collisionless propagation of the n=0 mode towards resonance are given below:

1. $|B_z|$ **Increases** - This is an expected result. Stix shows (Stix, Theory of Plasma Waves, p.51, Eq(18))[15] that for a homogeneous lossless medium, the group velocity is

$$v_g = \frac{\mathcal{P} + \mathcal{T}}{W_0} \tag{19}$$

   When resonance is approached, the group velocity slows down, resulting in an increased energy density W_0. This increased energy density is apparent in the increase in $|B_z|$, since the energy density varies as

$$W_0 = \mu_0 \frac{|B|^2}{2} + \epsilon_0 \frac{|E|^2}{2} \tag{20}$$

2. **Increase in axial and radial k_z** - As resonance ($\omega = \omega_{ci}$) is appraoched, the left hand cut-off ($k_z^2 = k_0^2 L$) increases, causing an increase in the resulting k_z eigenmodes. This is consistent with the slowing down of the group and phase velocities as resonance is approached.

3. **High edge electric fields E_+, E_- and E_z that propagate inward** - This is a result that could be consistent with experimental observation. Golovato points out (Personal communications) that although a high edge electric field is predicted by the ANTENA code, experimentally no edge electric field is detectable. The BEACH simulation shows that the reason that no edge electric field is detectable is that the edge spike moves radially inward into the plasma as resonance is approached.

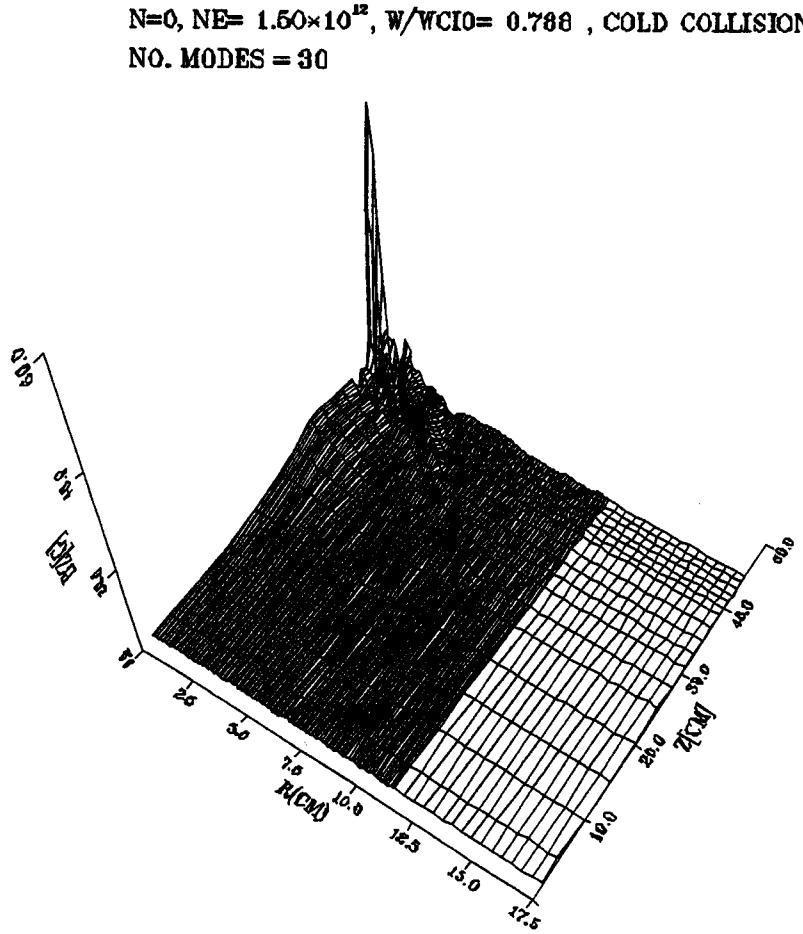

Figure 9: ICRF $\mathbf{B_z}$ Propagation in a Cold **Collisionless** Plasma, Full Turn Loop Antenna, $\omega/\omega ci0 = 0.788$. Waves are launched by the ICRF antenna at $z = 0$cm and propagate towards resonance at $z = 50$cm.

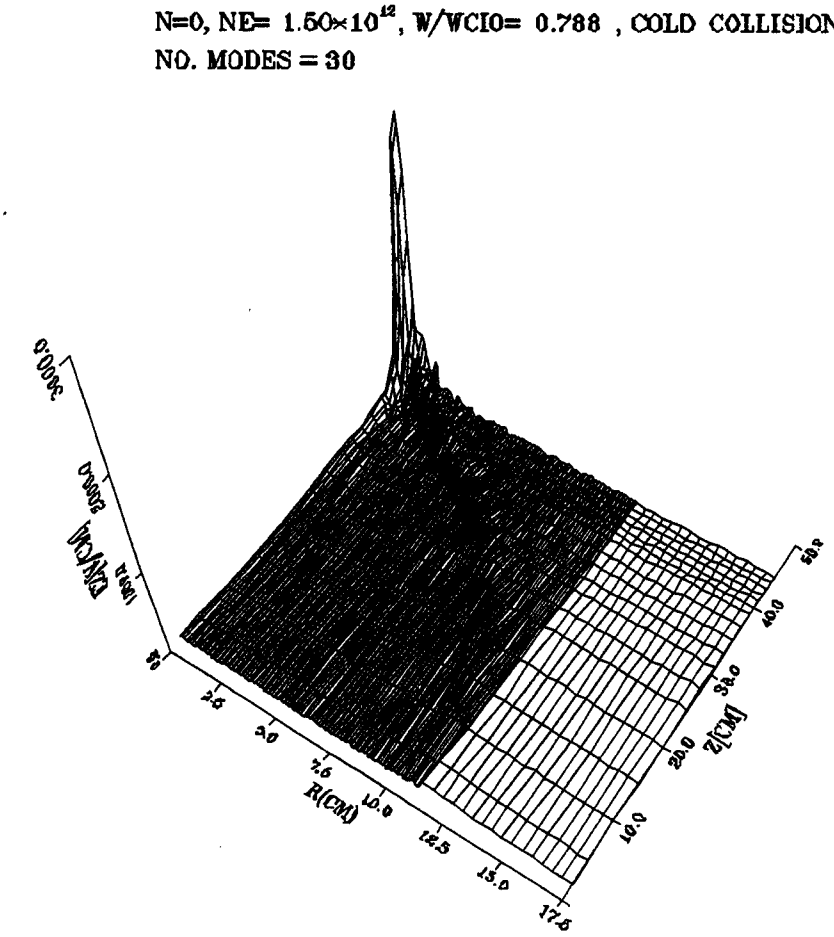

Figure 10: ICRF $\mathbf{E}_z$ Propagation in a Cold **Collisionless** Plasma, Full Turn Loop Antenna, $\omega/\omega ci0 = 0.788$

4. **Higher order modes excited at higher amplitudes N for lower initial ω/ω_{ci}** – This result reflects the effect of the antenna excitation profile ($J_\theta(k_z)$) on the excited EM field coefficients. For a lower ω/ω_{ci}, the value of the left-handed cut-off in the infinite plasma dispersion relation $k_0^2 L$ decreases. Since the $J_\theta(k_z)$ profile remains constant, this means that ALL modes are now excited to higher values.

3.2.2 Collisional

The presence of collisions, of course, implies a finite temperature. The *Cold Plasma Collisional Model* means that the expansion of the plasma Z-function excludes temperature effects and keeps only terms of $O(\nu_i/\omega)$. The code results for the case of ICRF propagation in a cold collisional plasma is shown in Figure 11.

The presence of collisions manifests itself in a complex dielectric tensor.

$$\underline{\underline{\epsilon}} \equiv \begin{bmatrix} S & -iD & 0 \\ iD & S & 0 \\ 0 & 0 & P \end{bmatrix} \tag{21}$$

where

$$S = \tfrac{1}{2}(R+L) \tag{22}$$

$$D = \tfrac{1}{2}(R-L) \tag{23}$$

The presence of collisions in a cold plasma produces the following expansions for S, D, and P

$$S = 1 - \sum_\alpha \frac{\omega_{p\alpha}^2}{\omega D_D} \left\{ \begin{array}{c} \omega(\omega^2 - \omega_{ci}^2 + \nu_i^2) \\ -i\nu_i(\omega^2 + \omega_{ci}^2 + \nu_i^2) \end{array} \right\} \tag{24}$$

$$D = \frac{\omega_{pi}^2 \omega_{ci}}{\omega} \frac{\left(\omega^2 - \omega_{ci}^2 - \nu_i^2 - 2i\omega\nu_i\right)}{\left(\omega^2 - \omega_{ci}^2 - \nu_i^2\right)^2 + 4\omega^2\nu_i^2} \tag{25}$$

$$P = 1 - \textstyle\sum_\alpha \frac{\omega_{p\alpha}^2}{\omega(\omega + i\nu_{c\alpha})} \tag{26}$$

Using these complex elements of the dielectric tensor, the dispersion relation can be solved with the geometric boundary condition to yield a set of eigenmode solutions for this plasma–vacuum geometry. The difference between these solutions and those of the cold collisionless plasma is that the k_z eigenmodes are now complex – these waves are now damped as they propagate towards the cyclotron resonance. This damping transfers energy from the waves to the plasma, causing plasma heating.

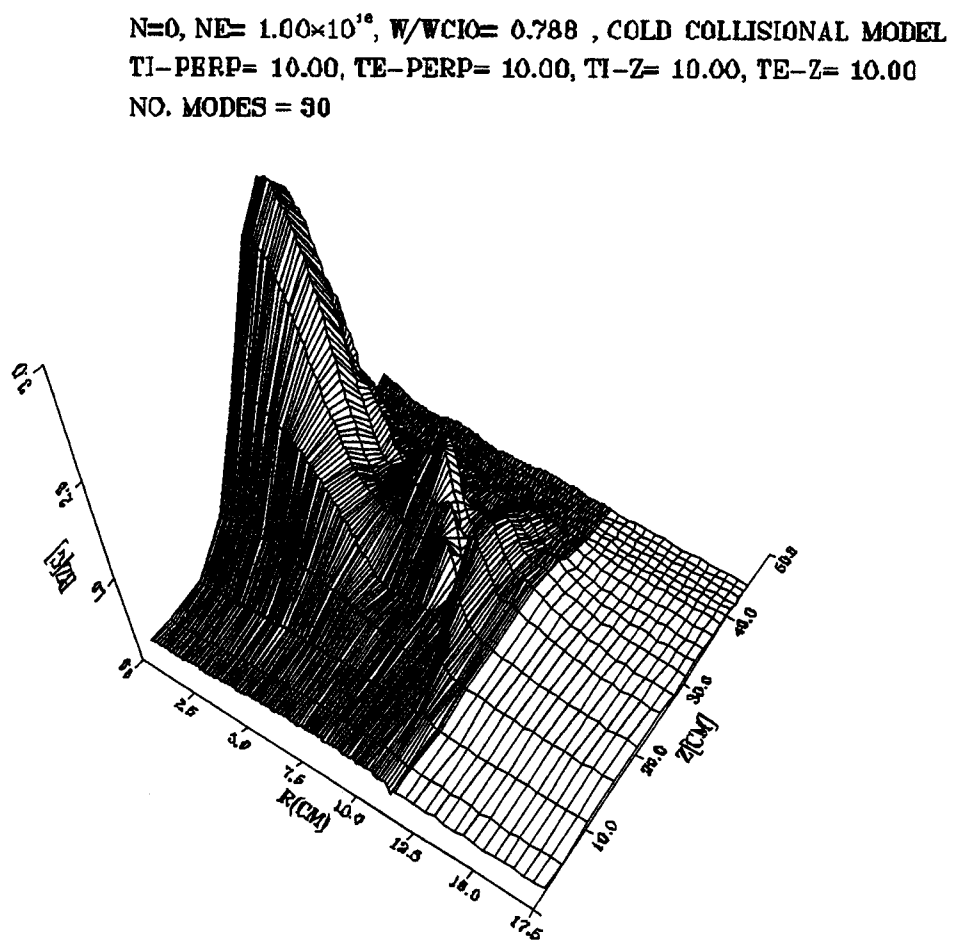

Figure 11: ICRF $\mathbf{B_z}$ Propagation in a Cold **Collisional** Plasma, Full Turn Loop Antenna, $\omega/\omega_{ci0} = 0.788$

N=0, NE= 1.00×10^{16}, W/WCIO= 0.788 , COLD COLLISIONAL MODEL
TI-PERP= 10.00, TE-PERP= 10.00, TI-Z= 10.00, TE-Z= 10.00
NO. MODES = 30

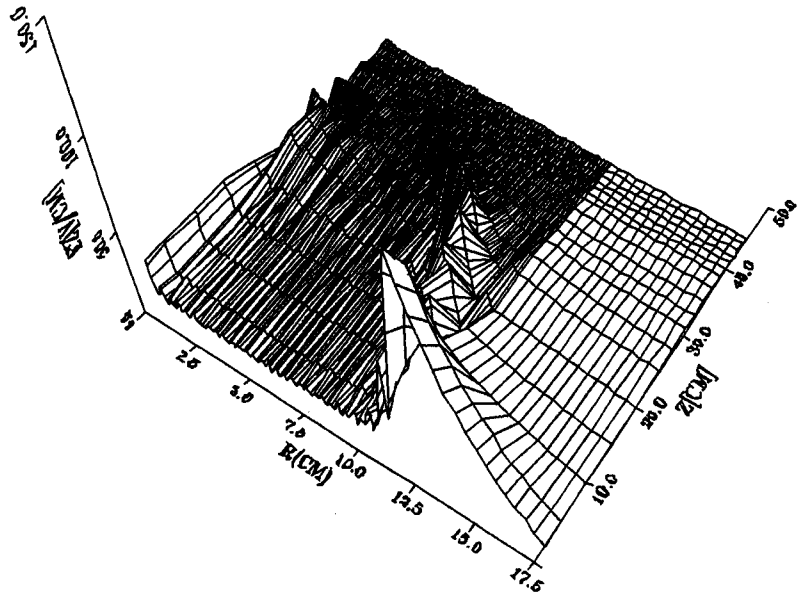

Figure 12: ICRF $\mathbf{E_z}$ Propagation in a Cold **Collisional** Plasma, Full Turn Loop Antenna, $\omega/\omega_{ci0} = 0.788$

4 Thrust Balance Development

There is a need to develop an accurate and sensitive target balance to measure the momentum transfer in a plasma system, such as an electric propulsion device, plasma propulsion systems and in the divertor of a tokamak fusion reactor. In electric propulsion research the common method to measure the thrust is a balance consisting of the suspended thruster and a displacement sensor. The thrust is determined from the displacement of the thruster when it recoils at the firing of the thruster. This method has several drawbacks: The thruster is heavy. It is tied to heavy electric power cables and gas feed line and therefore has a very high motion resistance. There are frictional losses due to the suspension of the heavy thruster and the transfer of displacement through pulleys to the sensor. In the future, the header will probably need to be cooled for high power operation. The motion resistance will be much higher with added cooling lines and heavier power cables. These factors will reduce the sensitivity and accuracy.

For the purpose of studying the momentum transfer in a fusion plasma system there are two methods being used by other groups. One is to attach the target through a long shaft to the diaphragm of a commercial pressure transducer. The shaft is suspended by two strings. The suspended target and the shaft system behaves like a pendulum and the pressure transducer serves as a displacement sensor. The other method is similar to the suspended target and shaft assembly whereas the sensor consists of a magnet and a pick-up coil. The force can be determined from the voltage induced on the pick-up coil from the motion of the magnet. The sensor unit has to be housed in a magnetically shielded box. The long arm of these two systems will make them difficult to be installed in the plasma stream in a closed system like tokamak. None of the systems mentioned above has provided adequate means to deal with the problem of mechanical vibrations, electric and magnetic interferences.

The target balance system developed in this work consists of two identical plates suspended by needle points. The device is compact, light and is symmetric with respect to the equilibrium position as either or both plates is impinged by plasma from opposite directions. The system can, therefore, be inserted in the plasma stream in a closed system like tokamak. The mechanical vibrations can be eliminated as a common mode to the two identical moving pendulum. The electric and magnetic pick-ups have been reduced to a negligible level by the use of differential amplifiers, shieldings and dynamic bandpass filters. The detailed developmental process of the pendulum system, electronic circuit, the analysis and measurement are described in the following subsections.

4.1 The Balance Development

The purpose of this work is to find a suitable method to measure the thrust in the Tandem Mirror Plasma propulsion device [1] [2] [3] [16]. At present the device is operated in the low power level and at a high specific impulse (about 13,000 sec). The thrust level is very low and is estimated to be at about 100 mN. To measure such a low thrust a sensor must have the sensitivity and accuracy of better than .1 mN. The balance has to be very compact so that it can be mounted in the limited space of the exhaust chamber.

The propulsion system is presently operated in a pulsed mode and plasma is created by microwave radiation and heated to high temperature by rf power, The magnetic impulse and mechanical vibrations, rf pick-ups, electric field, electromagnetic noises from the power supply systems are many orders of magnitude stronger than the anticipated thrust level. Undoubtedly they must be eliminated. At the beginning we were hoping to adapt the known methods. As described above none of them are adequate for our system. The possibility of using torsion wire and strain gauge has also been carefully examined and found not desirable either.

In order to keep the system as simple and compact as possible, we have given the simple pendulum a serious consideration. However, it loses its simplicity and compactness when the position sensing system is incorporated. After weighing all the odds we decided a system consisting of double plates is our best bet. We were encouraged by the initial success of a pendulum and fixed plate system as shown in Figure 13a. Both the moving and fixed plates are identical in size and shape and are made of aluminium. The displacement of the pendulum is translated into variation of capacitance of the plates. The capacitance measuring method will be described later. The signals for the balance in the air and in the vacuum chamber are shown in Figures 14a and 14b respectively. The oscillations in the air were produced by mechanical shock. The oscillation in the vacuum is produced by pulsing the magnetic field. As can be seen from these figures, the signal taken in the air damped quickly whereas there was almost no damping in the vacuum. This shows that the friction loss at the needle support is negligible. The magnitude of the magnetic impulse is very large and can be eliminated by dividing the plates into very thin strips.

The mechanical vibrations are the second order noise which appears when the magnetic impulse is removed. As shown in Figure 14c, such noise is random and could not be reduced with suspension methods. To eliminate the mechanical noise, both plates are suspended and swing as an independent pendulum (Figure 13b). Since both plates respond identically to the noise, no net change in the capacitance is produced and therefore no net signal is recorded from the noise.

In the plasma stream, the conducting plate acts as a big Langmuir probe which will detect the electric field and current. These electric field are the third order effects which appears when the vibrational noise is cancelled out. As shown in Figure 14d, these electric fields are still very large. To reduce the electric field, insulating materials such as ceramic or silicon are used on the surface facing the plasma. Further, a set of plates with conducting strips are placed above the support. The electromagnetic noise from the inverse pendulums can then be used to cancel the noise picked up by the regular pendulums below the support. The inverse pendulum above the support swings opposite to the regular pendulum below so

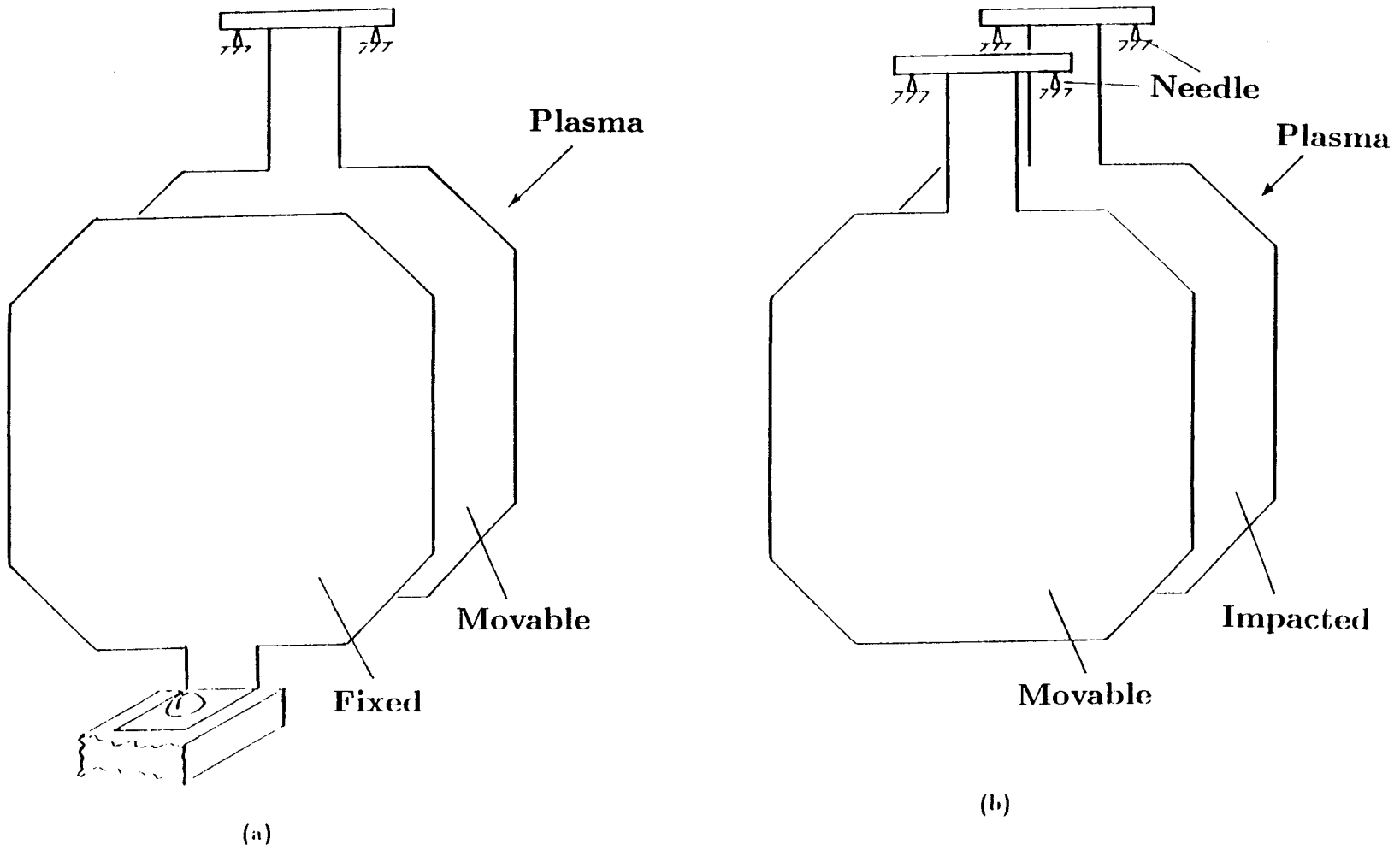

Figure 13: A thrust balance consisting of a simple pendulum and a fixed plate(a), and two identical moving platex (b)

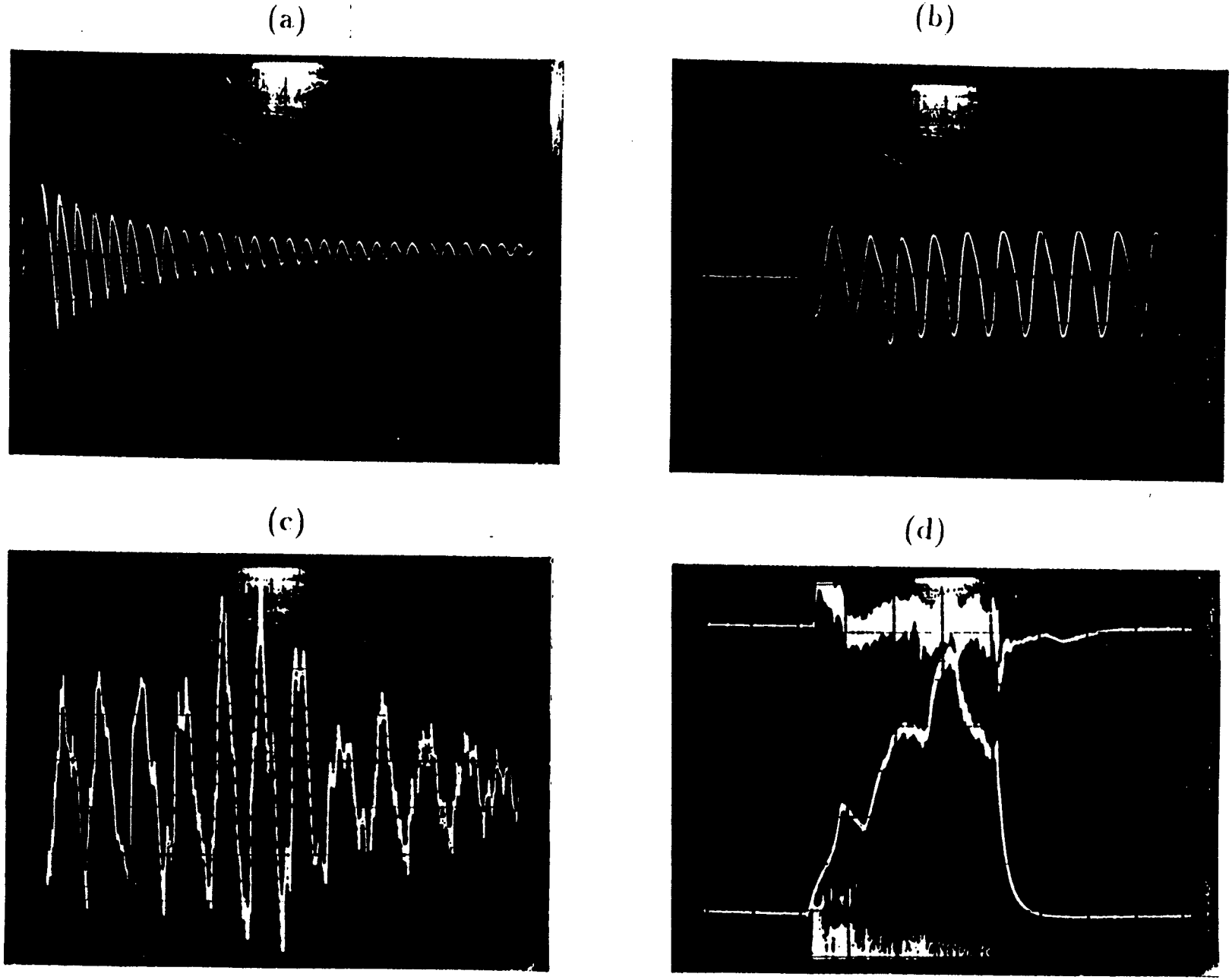

Figure 14: Signals from the thrust balance: (a) A damped oscillation from a mechanical shock in the air, (b) a nondamping oscillation produced by magnetic impulse in the vacuum, (c) mechanical noises and (d) electric noises.

that the signs of the voltages from these two sets of capacitor plates are opposite, whereas the signs of pick-up voltages from electric and magnetic noise are the same. By using a differential amplifier the pick-up signals are cancelled out and the real signals are summed. This system is shown in Figure 15.

Since the inverse pendulums are smaller than the regular ones, the noise can not be removed completely. To further avoid the electric field effect due to plasma, the plate in contact with the plasma is made entirely with an insulator, i.e., no conductor strips even on the back face. As depicted in Figure 16, the device is now a quadruple pendulum system where there is a set of double capacitor plates above the support and another set of double capacitor plates below the impact plates which are now made of insulators. The double capacitor plates consist of conductive metal strips used to monitor the signals. These capacitor plates are enclosed in a conducting box to shield out the electric and magnetic pick-up. Any residue pick-up can be further eliminated with the use of differential amplifiers. This method effectively reduces the pick-up and enhances the sensitivity. The magnetic noise produced by the power supply was the most difficult to deal with and can not be eliminated by the means described above. It was reduced with a carefully designed active filter.

4.2 The Signal Treatment

The simplified electronic circuit diagram is shown in Figure 17. To detect the small change in capacitance of the two pendulums, a carrier radio frequency voltage at 30 kHz is applied to plates. There are two pairs of signals, one pair from the top capacitor plates and the other from the bottom capacitor plates. The signals from the each pair of plates are carried by a pair of twisted wires to the inputs of a differential amplifier. Since the inverse pendulum plates on the top swing in the opposite direction to the pendulum plates at the bottom, The signs of the signal from the output of the differential amplifiers are opposite. These outputs are again summed by the third differential amplifier. Therefore the overall signal is enhanced after all the noises are eliminated.

The carrier frequency is removed from the signal by rectifiers. The residual noise is practically cancelled by the differential amplifiers. The magnetic ripples from the firing of SCRs in the power supplies are the most stubborn problem. The frequency of this noise has fallen in the range of the carrier frequency. This noise is filtered by a very carefully designed active bandpass filter. A high quality clean signal can finally be obtained.

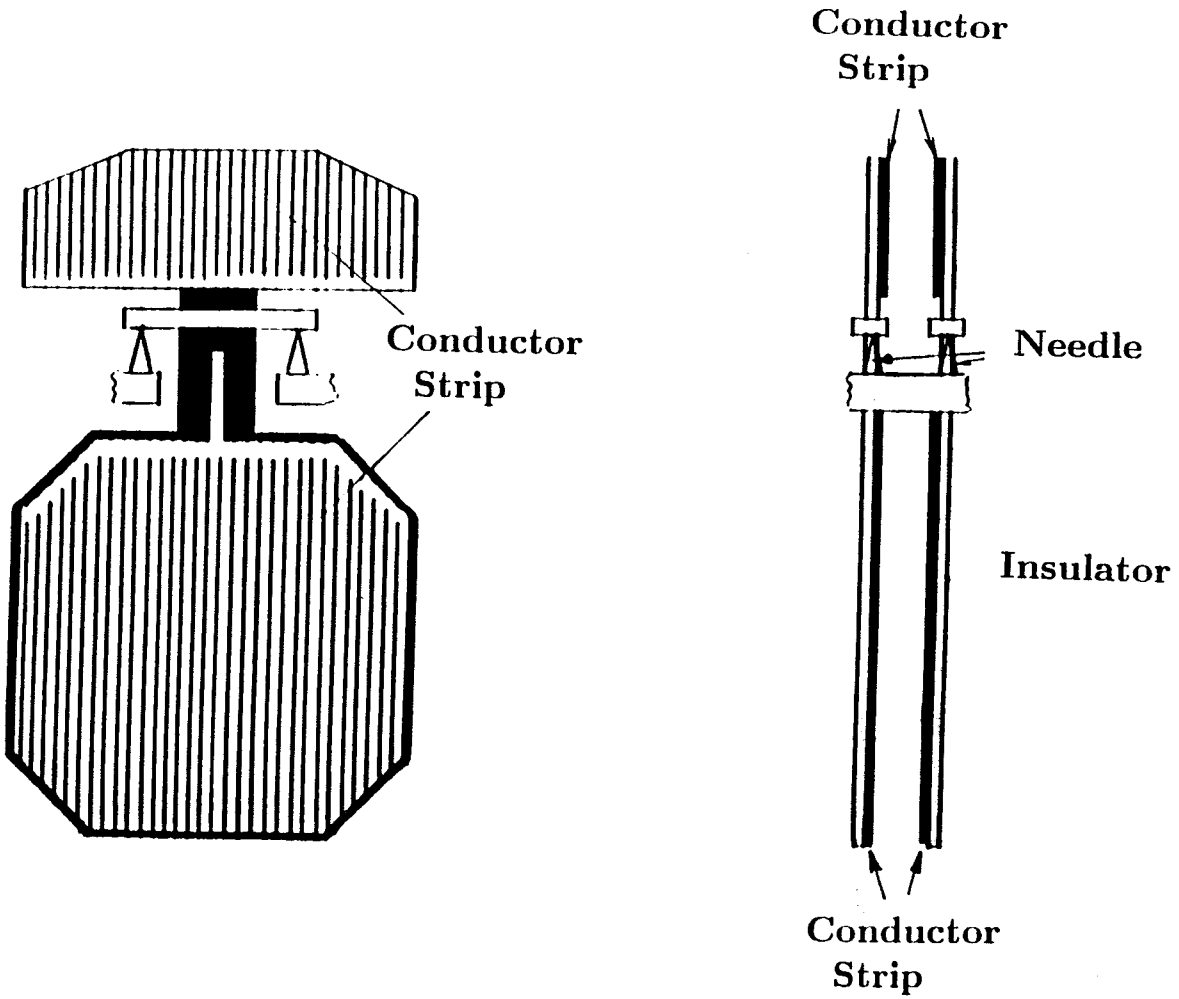

Figure 15: A thrust balance with inverse pendulums consisting of insulator and fine conductor strips.

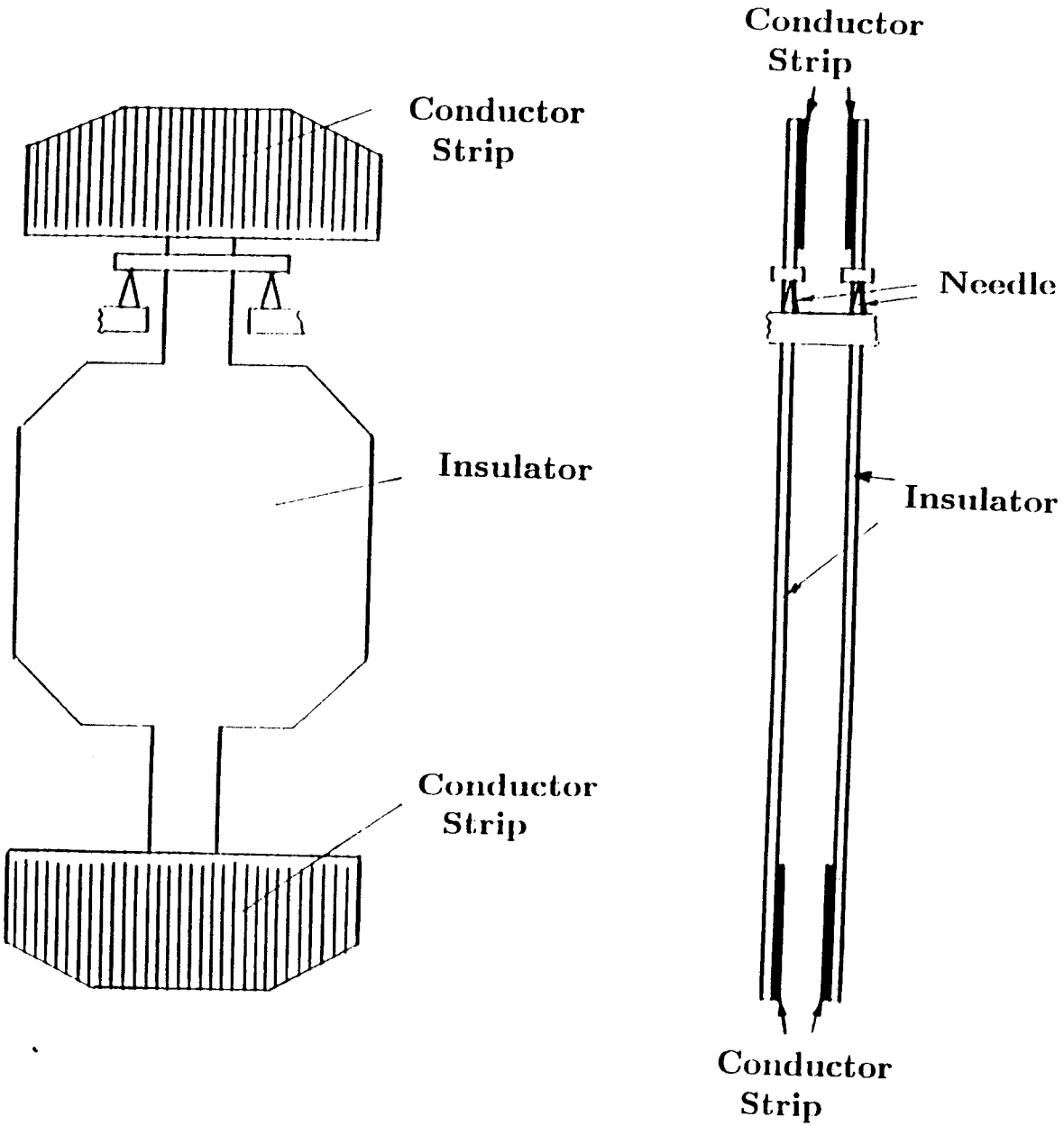

Figure 16: The working version of the thrust balance consisting of nonconducting target plates and sensor capacitor plates with fine conducting strips enclosed in shielded boxes on the top and bottom.

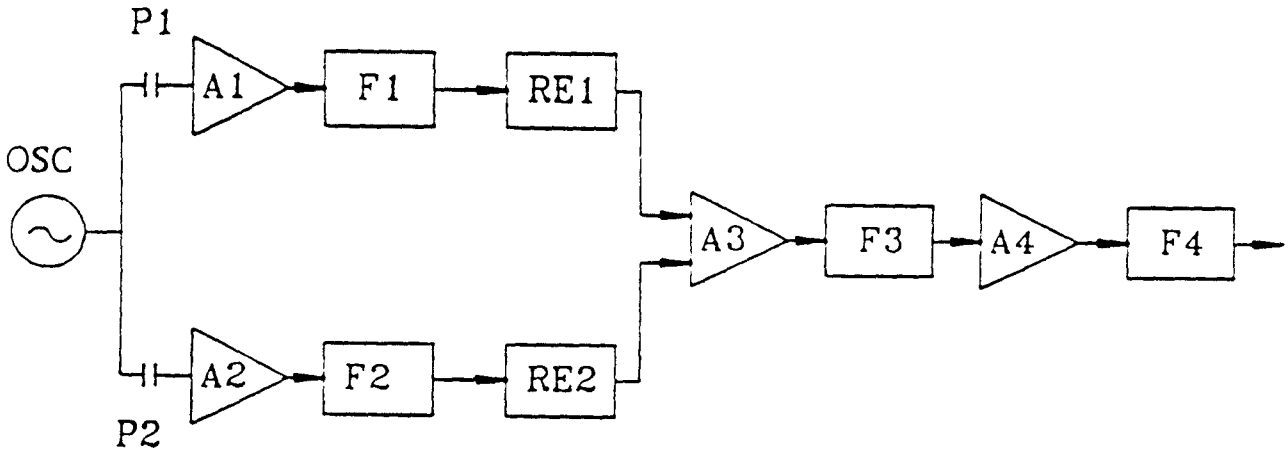

Legend

OSC	Oscillator, 40kHz, 100V	A3	Differential Amplifier
P1,P2	Double Pendulum	A4	Output Amplifier
F1,F2	Active Filter	F3	Anti-DC-Drift Filter
RE1,RE2	Rectifier and Filter	F4	Low Pass Filter

Figure 17: Block diagram of the electronic circuit

4.3 Experimental

The two pendulums of the thrust balance are not exactly identical and, therefore, their natural frequencies are not equal. When a mechanical impulse is applied, a beat as shown in Figure 18a is produced. The frequency of the beat is about one twentieth of the natural frequency or the period is 20 times longer. This beat frequency will become smaller when two natural frequencies are made to be closer. A great effort has been made to tune the two pendulums to make their natural frequencies match. However, a perfect match can not be achieved and it can only make the beat period longer. The beat can not be eliminated completely. Currently the thruster is operated in a pulsed mode and is fired in the first half cycle of the natural oscillation. The trace of the first cycle in Figure 18a is expended as is shown in Figure 18c. This expended trace shows that the noise level is negligible. Figure 18d presents the relationship between the plasma density and temperature traces from a triple probe and the pendulum signal. This shot was made using the pendulum system shown in Figure 15 where the signal died out after one cycle. It should continue to oscillate without damping and therefore it may not be the valid signal. In order to determine the validity of the measurement it is necessary to carry out detailed analysis which will be given in the next section. An exhaustive study of the residual noise from the power supply reveals that they can sometime cause misleading false signal even at a very low level. The complete elimination of such noise is necessary and was accomplished with the use of dynamic bandpass filters.

Finally Figure 19 presents the signal obtained with the working pendulum system shown in Figure 16 using the electronic circuit shown in Figure 17. The signal continued to oscillate without damping but was not symmetric with respect to the baseline. This requires a solid explanation in order to convince ourself that it is in fact a correct signal. The amplitude of the signal rises from a negative value to a constant symmetric oscillation after about three cycles. This asymmetric property is found to be due to the electric circuit as demonstrated by the circuit analysis given in the next section.

4.4 Analytical Solutions

As discussed above in order to validate the measurement it needs to carry out a complete analysis of the pendulum system and electronic circuit. Let us write down the equations of motion for a simple pendulum as shown in Figure 20. Assuming θ small, the equation of motion is

$$\frac{d^2\theta}{dt^2} = F_T - F_f - F_g \tag{27}$$

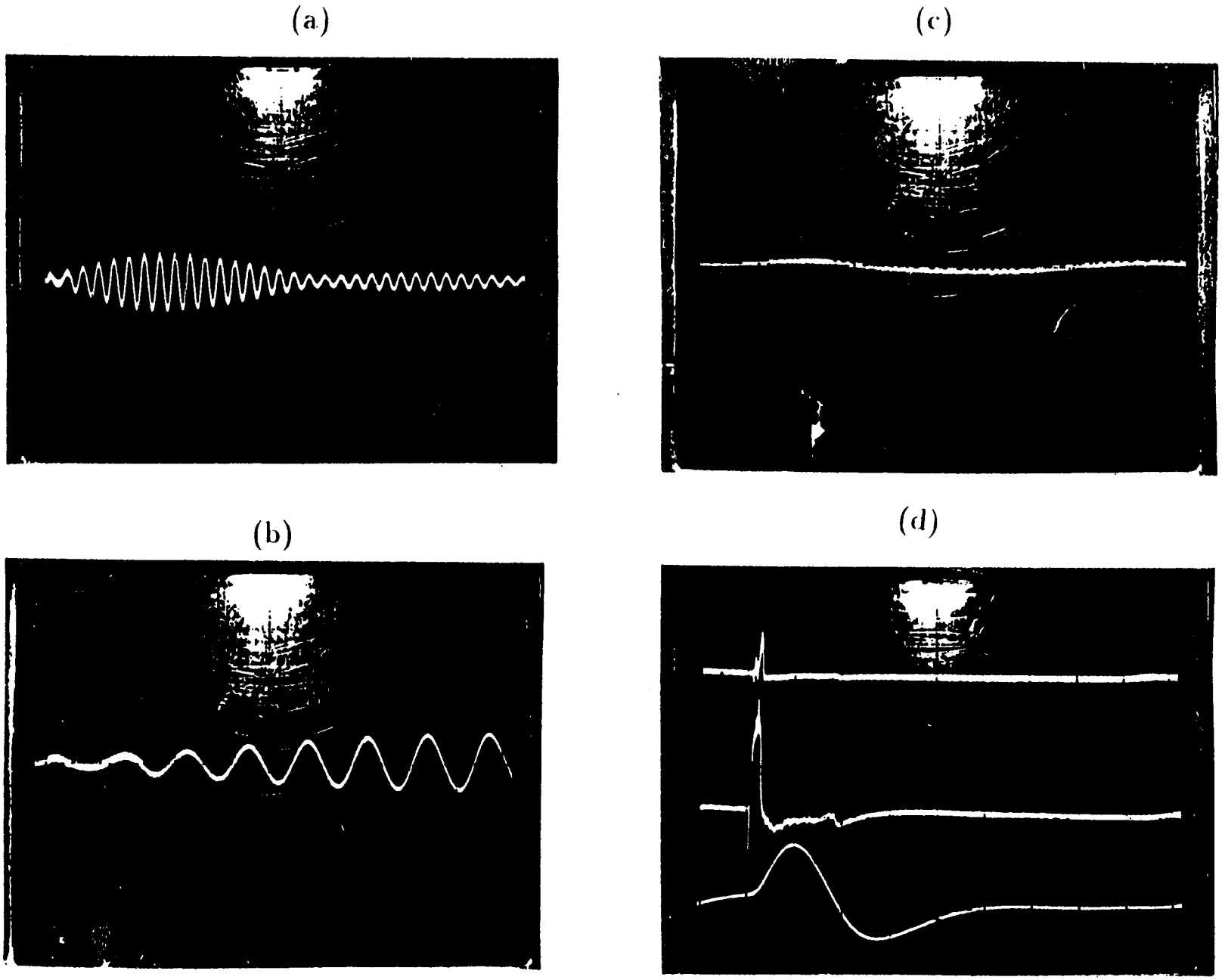

Figure 18: Waveform due to the beat of the two pendulums (a). Expanded waveforem (b). Expended trace of the first half cycle of the waveform (c). Plasma pulses and thrust signal (d).

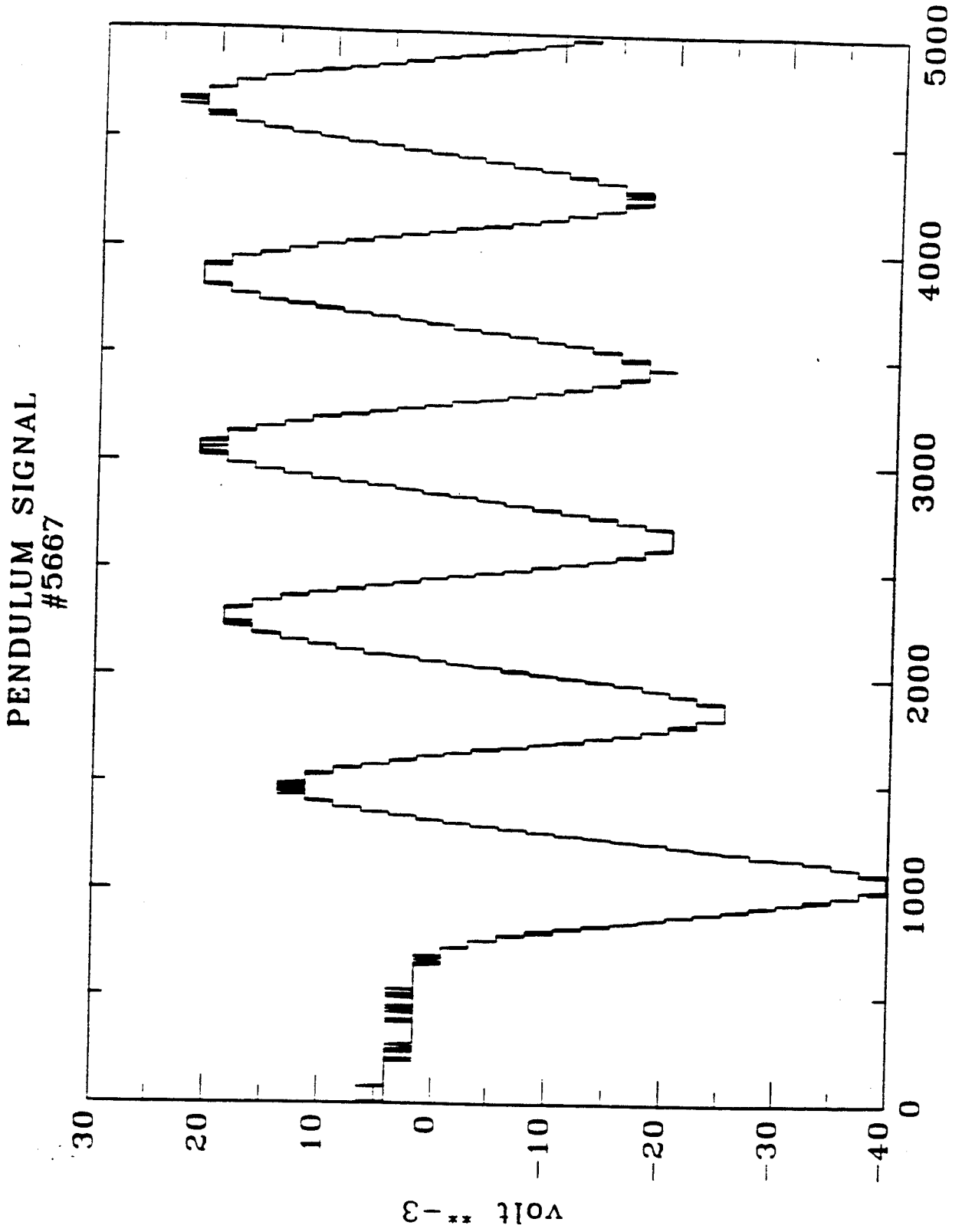

Figure 19: The thrust signal obtained using the working balance.

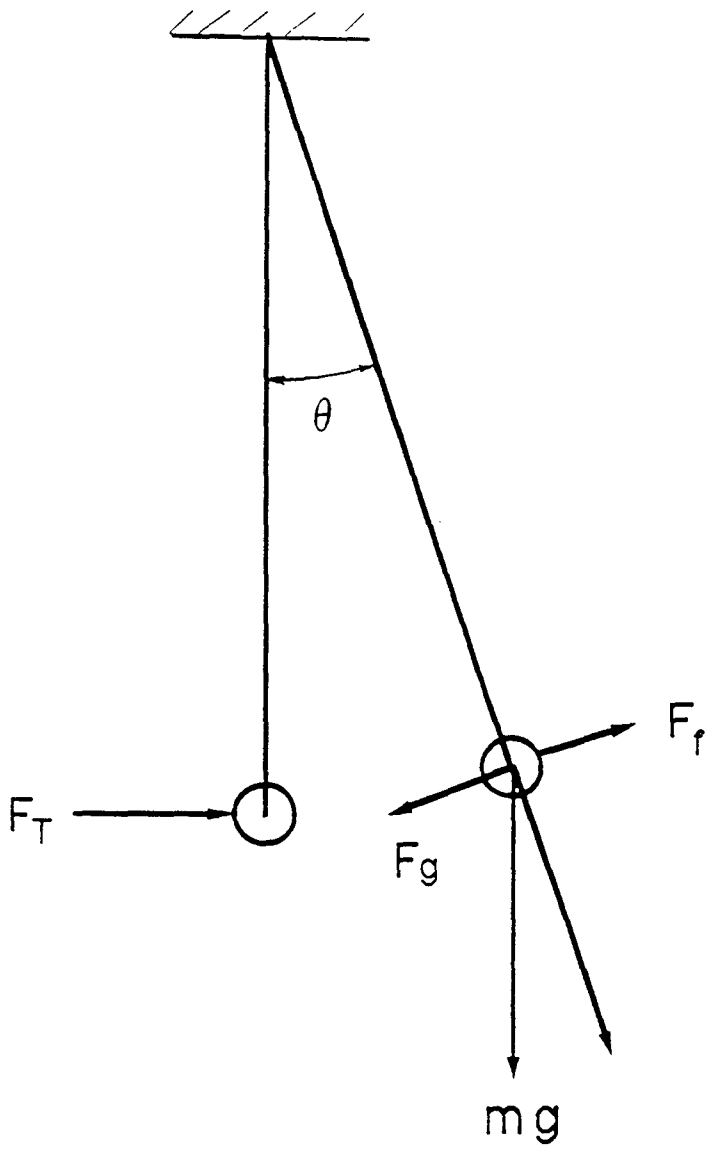

Figure 20: Simple pendulum.

where

$$\begin{aligned} F_T = &\quad Thrust \\ F_f = &\quad A\frac{d\theta}{dt} \\ F_g = &\quad mg\theta \\ A = &\quad a\text{damping factor} \\ \text{Let } \tau = &\quad \text{pulse length} \\ T_o = &\quad \sqrt{l/g} \end{aligned}$$

This equation has been solved for other systems. To understand the characteristics of this system the procedure for solving the equation of motion and results are presented in the following.

By apply Laplace Transformation

$$\Theta(S) = \frac{L[F_T]}{(S^2ml + SA + mg)} \tag{28}$$

Examine the solutions in two regimes:

1. $\tau << T_o$

$$\begin{aligned} F_T(t) = &\quad F_T\tau\delta(t),\ a\ \delta\ function \\ L[F_T] = &\quad F_T\tau \end{aligned}$$

2. $\tau >> T_o$

$$\begin{aligned} F_T = &\quad F_T \cdot 1(t),\ a\ step\ function \\ L[F_T] = &\quad \frac{F_T}{S} \end{aligned}$$

In each regime there are four different conditions:

1. $A = 0$, no damping
2. $0 < A < 4m2gl$, under damping
3. $A = 4m2gl$, critical damping
4. $A > 4m2gl$, over damping

In $\tau << T_o$ regime, apply Inverse Laplace Transformation to the equations for each condition, we obtain

1. For $A = 0$

$$\theta(t) = \frac{F_T\tau}{m\sqrt{gl}} \sin\sqrt{g/l}t \tag{29}$$

2. For $0 < A < 4m2gl$,

$$\theta(t) = \frac{2F_T\tau}{\sqrt{4m^2gl - A^2}} \exp(-\frac{A}{2ml}t) \sin(\frac{\sqrt{4m^2gl - A^2}}{2ml}t) \tag{30}$$

3. For $A = 4m2gl$,

$$\theta(t) = \frac{F_T\tau}{ml} t \exp(-\sqrt{g/l}t) \tag{31}$$

4. For $A > 4m2gl$,

$$\theta(t) = \frac{F_T\tau}{\sqrt{A^2-4m^2gl}} \{\exp(\frac{-A}{2ml} + \frac{\sqrt{A^2-4m^2gl}}{2ml})t - \exp(\frac{-A}{2ml} - \frac{\sqrt{A^2-4m^2gl}}{2ml})t\}$$

These solutions are plotted in Figure 21. Comparing the analytical solution and the experimental result presented in Figure 19 it appears that the experimental result can be explained by the damped solution. But it has shown previously that the friction at the needle support is negligible. The damping can not come from the pressure built-up in the chamber during the shot because it has been shown that there is no observable damping in the chamber at mtorr pressure range. Therefore this is not a true result. The result shown in Figure 19 appears to be real and in agreement with the undamped solution except the asymmetric property in the first three cycle. We reason that this is an effect of the asymmetric relative motion of the capacitor plates and the electronic circuit. Because the relative motion of the pair of plates on the top is opposite to that of the pair of the bottom plates, the asymmetric effects nearly cancel out and are ignored for simplicity. The electronic circuit is very complicated and there are high nonlinear elements. Fortunately, it can be represented by a drastically simplified diagram as shown in Figure 22 and two simultaneous linear equations as follows:

$$\begin{cases} \frac{dy}{dt} = \frac{dy_1}{dt} + \frac{y_1}{T_1}; \\ \frac{dz}{dt} + \frac{z}{T_2} = \frac{y_1}{T_2}. \end{cases} \tag{32}$$

where $T_1 = R_1C_1$ and $T_2 = R_2C_2$, and y and z are the input and output signal respectively. The solution is shown in Figure 23. Except for a slight phase different the analytical solution closely matches the experimental data. In any electric system phase shift is common and for this application we are not interested in its value. From this analysis we can confidently claim that the experimental result is the true measurement of the thrust free from mechanical, electrical and magnetic interferences.

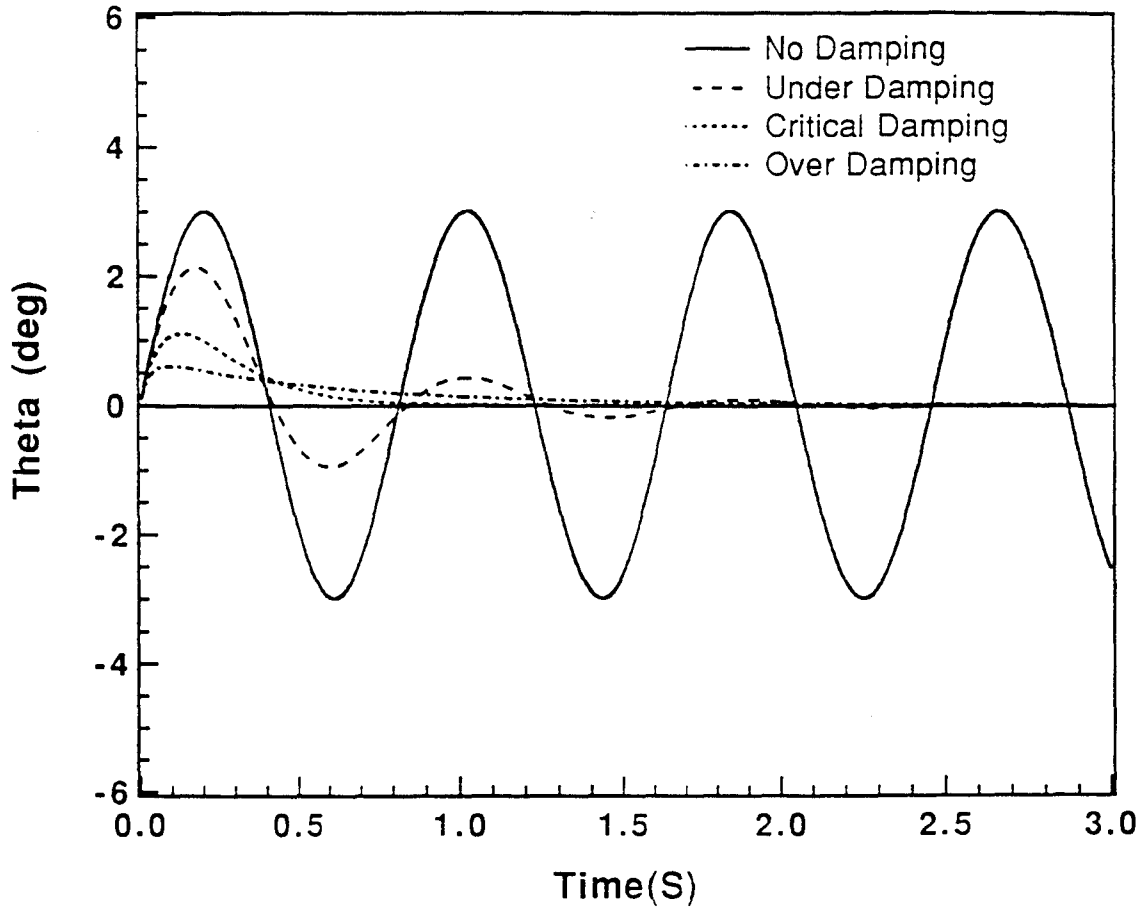

Figure 21: The waveforms of a simple pendulum for $\tau << T_o$

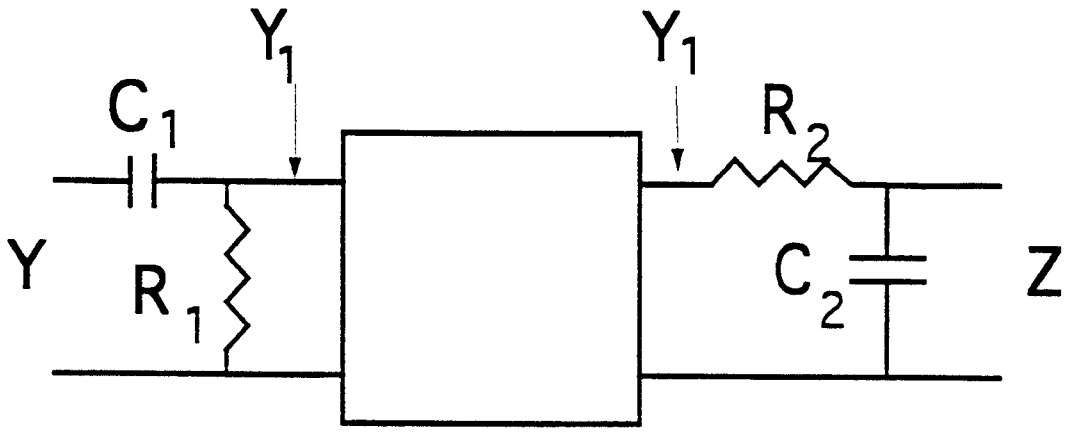

Figure 22: Simplified circuit diagram

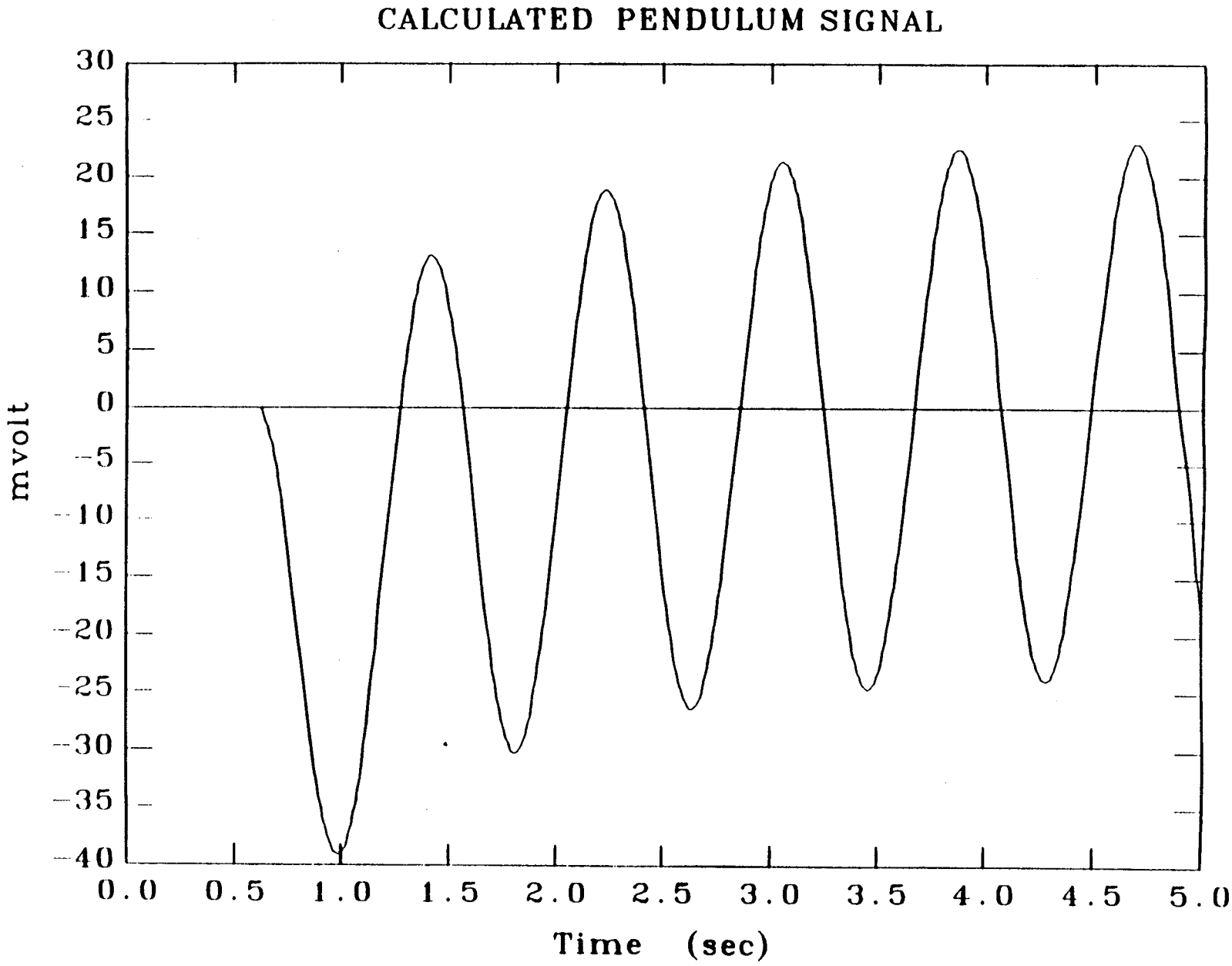

Figure 23: Output signal waveform of the simplified electric circuit

4.5 Experimental Results and discussion

The initial results obtained using this balance are presented in Table 2. The plasma temperature and density were monitored at a radial position two third of the plasma radius by a triple probe. The temperature at the center is monitored by a spectrometer using Doppler broadening method. A Langmuir probe biased at +100 V is used to measure the electron saturation current.

The specific impulse is 12,852 sec corresponding to the plasma temperature of 172 eV. The measured thrust is 76 mN in agreement with prediction. The propulsive efficiency is 68%. This can be considered as a milestone of this research.

This pendulum is made in the laboratory for testing purpose and is first of its kind. Therefore there is room for improvement. The plates are made from printed circuit board which consists of G-10 materials. G-10 material outgases during the plasma shot which degrades the plasma conditions. The new plates will be made from silicon wafers. For short pulse the particles can all be absorbed by the G-10 material. For long pulse the surface reflection has to be kept to a minimum and its effect has to be factored into the measurement.

There are two major advantages of this balance: (1) Since the plates are not parts of propulsion system and are simple and inexpensive to build; they can be made sacrificial for high power operation. (2) The balance is symmetric in both directions. It is particularly useful to study the pressure balance at the boundary layer between plasma and neutral gas in a gas divertor of tokamak reactors.

5 A Two-Optical-Path Laser Fluorescence Method

Measuring the H_α laser induced resonance fluorescence scattering from plasma is a method to determine the neutral hydrogen density. This method has been applied to toroidal tokomak plasma [17], [18], [19], and tandem mirror plasma [20], [21].

The laser induced fluorescence signal is usually much weaker then the H_α emission from plasma and the laser stray light. The signal extraction is difficult and inaccurate. This work shows that a clean signal can be extracted by using a two-optical-path technique. One optical path was focused on the spot in the plasma shone by the laser light, therefore it carries all signals (the H_α emission from plasma, laser stray light and fluorescence signal). Another path is focused on the spot inside the plasma slightly off the laser shined spot, It therefore carries only the H_α signal and stray light which will be called background signal for convenience. The optical paths were separated by a prism and then led to two photomultipliers. By subtracting the electric signals from the photomultipliers using a differential amplifier we were able to eliminate the background, and a nearly pure fluorescence signal was obtained.

5.1 Experimental Method

This Two-Optical-Path (TOP) laser fluorescence diagnostic system was located in the south exhaust chamber of the machine at a distance of 25 cm from the closest mirror point of the end cell. The electron temperature and density were measured by a fast Langmuir probe [22].

The crossectional view of the vacuum chamber, the laser beam and the detection optical system is shown in Fig. 24. The laser used here is a flashlamp–pumped dye laser (Candela EDL–6) tuned by an angle–tuned 40μ air–spaced etalon. A monochromator was used to monitor the wavelength of the laser output. A photo-diode, mounted directly behind the 99.9% reflecting rear cavity mirror of the laser is used to monitor the power of each laser pulse. A telescopic system in front of laser improves the beam convergence . The beam can be focused at various radial position in the plasma by adjusting the concave lens. In the beam entry port there were three copper knife-edge baffles which were arranged to minimize the stray light intensity. The gate valve in front of the baffles was used for vacuum isolation. The scattering system housed in a box on top of vacuum chamber can be moved radially. As will be discussed later it contained a big collection lens, 7 cm in diameter and 10 cm focal length, mounted across a $30cm \times 10cm$ observation window. Radial scan can be made from $r = 0$ to $r = 4.5$ cm. This limitation was due to the 10 cm transverse opening of the aperture which can be increased for larger radial scan in the future. A $30cm \times 10cm$ viewing dump which was made of stacked non–magnetic razor material located on the bottom of the chamber opposite to the scattering system box. The beam dump at the exit port consists of two disks of absorbing OB10–type glass. The glass was set at Brewster's angle to the incident laser direction in such a way that both polarization components were attenuated.

The sketch of the scattering system, the light paths and side view of the plasma and vacuum chamber are shown in Figure 25. The laser is normal to the entry quartz window and shines on the plasma at the spot as shown. The optical paths consist of a big lens, a

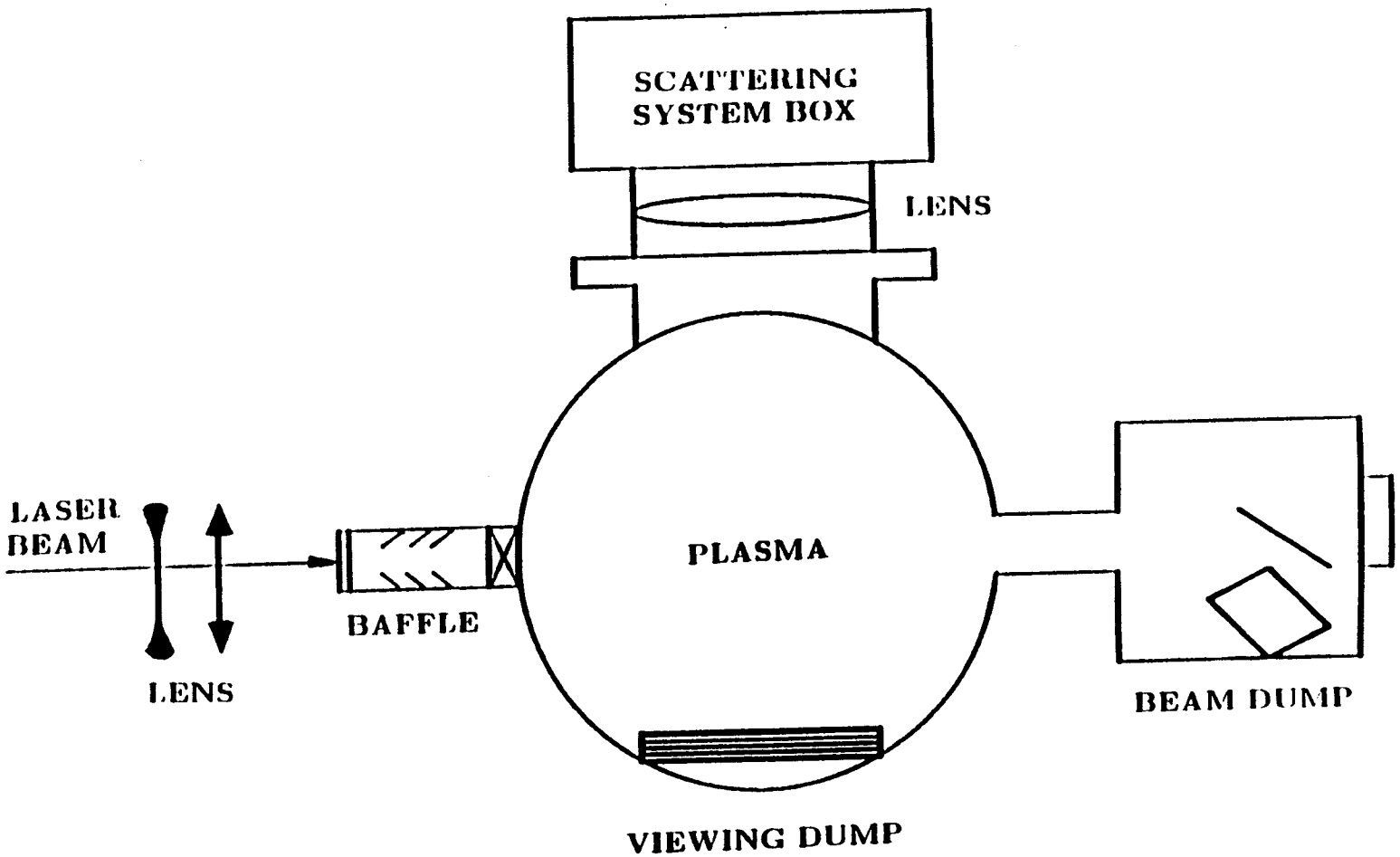

Figure 24: The laser beam and detection optical system.

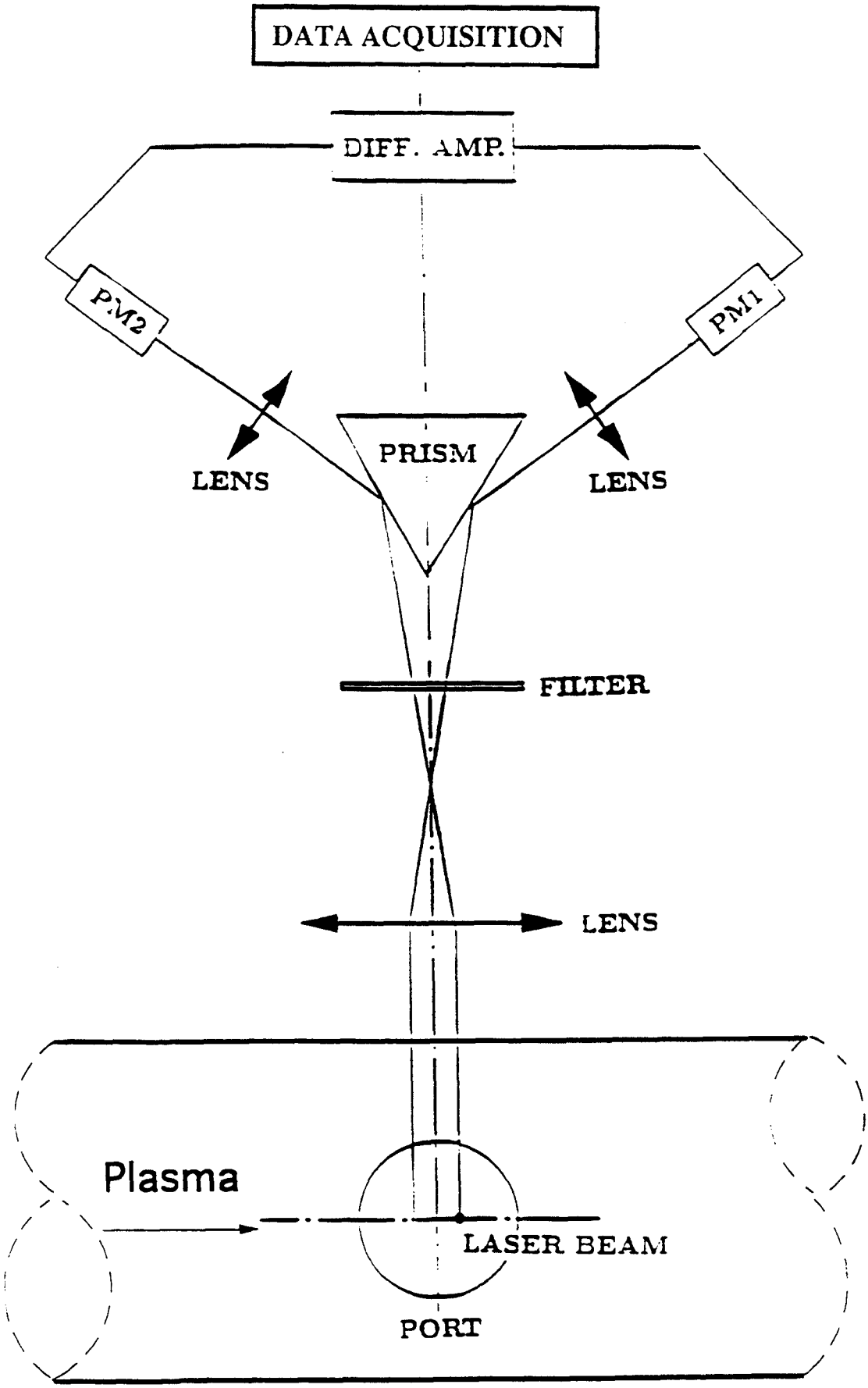

Figure 25: The sketch of the scattering system.

filter, a prism and two small lenses. The surface of the prism is deposited with a thin coating of aluminum which gives a surface reflectivity of 95%. The prism was adjusted so that the image of the each optical path fell on the entrance slits of the photomultipliers, PM1 and PM2 respectively. PM1 receives the light from the laser shone plasma spot, whereas PM2 receives the light from the plasma spot at an axial position slightly off from the laser spot. To induce the fluorescence emission of H_α from the hydrogen the wavelength of the laser was tuned to 6563$\mathring{A}$. The induced fluorescence light emitted form the plasma at the laser spot is led to PM1, whereas PM2 picks up the background signal only. When the laser light is not in tune with the H_α line no fluorescence emission was induced and both photomultipliers PM1 and PM2 receive only the background signal. The outputs from PM1 and PM2 are nearly equal and can be subtracted completely. The difference of the signals was obtained using a differential amplifier (Tektronix 502) with a gain of 10. The contribution of the background was further reduced by placing a narrow band filter, with a bandpass of 5 Å and transmission coefficient of 53%, in between the big lens and the prism. The Hamamatsu R928 photomultiplier tubes is shielded magnetically with high μ material. The optical parts were also shielded both optically and magnetically. The output from the differential amplifier and the power monitoring signal were processed by 6 MHz and 100 kHz digitizers respectively.

The laser was tuned to Balmer–alpha line 6563 Å by an etalon and had a linewidth of about 0.75 Å. The laser output power was about 80 kW and 1/3 of that power was focused on the plasma. The focused spot size was $0.4-0.5/cm^2$. The laser power of $10/kW\text{cm}^{-2}\text{Å}^{-1}$ was sufficient to saturate the $n = 2$ to $n = 3$ transition of hydrogen atom. The fluorescence intensity does not depend on the laser power.

The laser fluorescence signal was absolutely calibrated by Rayleigh scattering in nitrogen gas. The ratio of the fluorescence signal, F, to Reyleigh scattered signal, R, is

$$\frac{F}{R} = \frac{\Delta N_3 A_{32} T_L \pi r^2}{N_L N_{N_2} \sigma_R}$$

where ΔN_3 is the difference in population of hydrogen atom in the $n = 3$ state with and without laser, $A_{32} = 4.4 \times 10^7 sec^{-1}$ is the induced transition probability from $n = 3$ to $n = 2$, $\sigma_R = 2.16 \times 10^{-27} cm^2$ is the Reyleigh scattering cross section, $T_L = 5\mu s$ is the duration of the laser pulse, $r = 0.5$ cm is the radius of laser spot, $N_{N_2} = 3.54 \times 10^{16} P$ (P is the pressure of nitrogen in Torr) is the molecular number density of nitrogen in Reyleigh scattering, $N_L = 7.9 \times 10^{17}$ is the input photon number for Reyleigh scattering laser light of energy $E_L = 480$ mJ used in our experiment. The Reyleigh scattered signal was found to be $R = 7.8P$. Thus, $\Delta N_3 = 4.49 \times 10^4 F$, where F is fluorescence signal related to the Reyleigh scattered signal. According to the theory of the collisional–radiative model[9], the ground state population of neutral hydrogen depends on the electron temperature and plasma density. They were measured by a fast Langiniur probe located at same radial position as the laser spot.

5.2 Results and Discussion

The flat top of the ICRH pulse duration is 20. The laser was fired at 12 ms after the initiation of ICRH pulse and was at about the middle of flat top. Figure 26a shows the light spectrum from path PM1. The sharp line contains the laser stray light and fluorescence light, and the continuous spectrum is the H_α emission and stray lights. Figure 26b shows the spectrum of the lights from the path PM2. The difference of the magnitudes of the two sharp lines is the fluorescence signal as shown in Figure 27. The magnitude of this real signal is much smaller than the stray laser light and even smaller than the H_α emission and stray lights. Without the use of PM2 the extraction would be very difficult and inaccurate. As is shown in figure 27 the TOP method gives a clear signal free of noise.

The radial profile of electron temperature T_e and density N_e measured by Langmuir probe are shown in Figures 28a and 28b. The neutral hydrogen density profile N_o, inferred from ΔN_3 with electron temperature T_e and density N_e is shown in Figure 28(c). The electron temperature $T_e$is about 40–50eV and density N_e is $2-3\times 10^9/cm^3$ which is an order of magnitude lower than that in the center cell because the plasma was expanded in the exhaust and the mirror ratio was 10. The neutral density near the center is one order of magnitudes smaller than that at $r = 4.5$. The plasma is fully ionized on the axis.

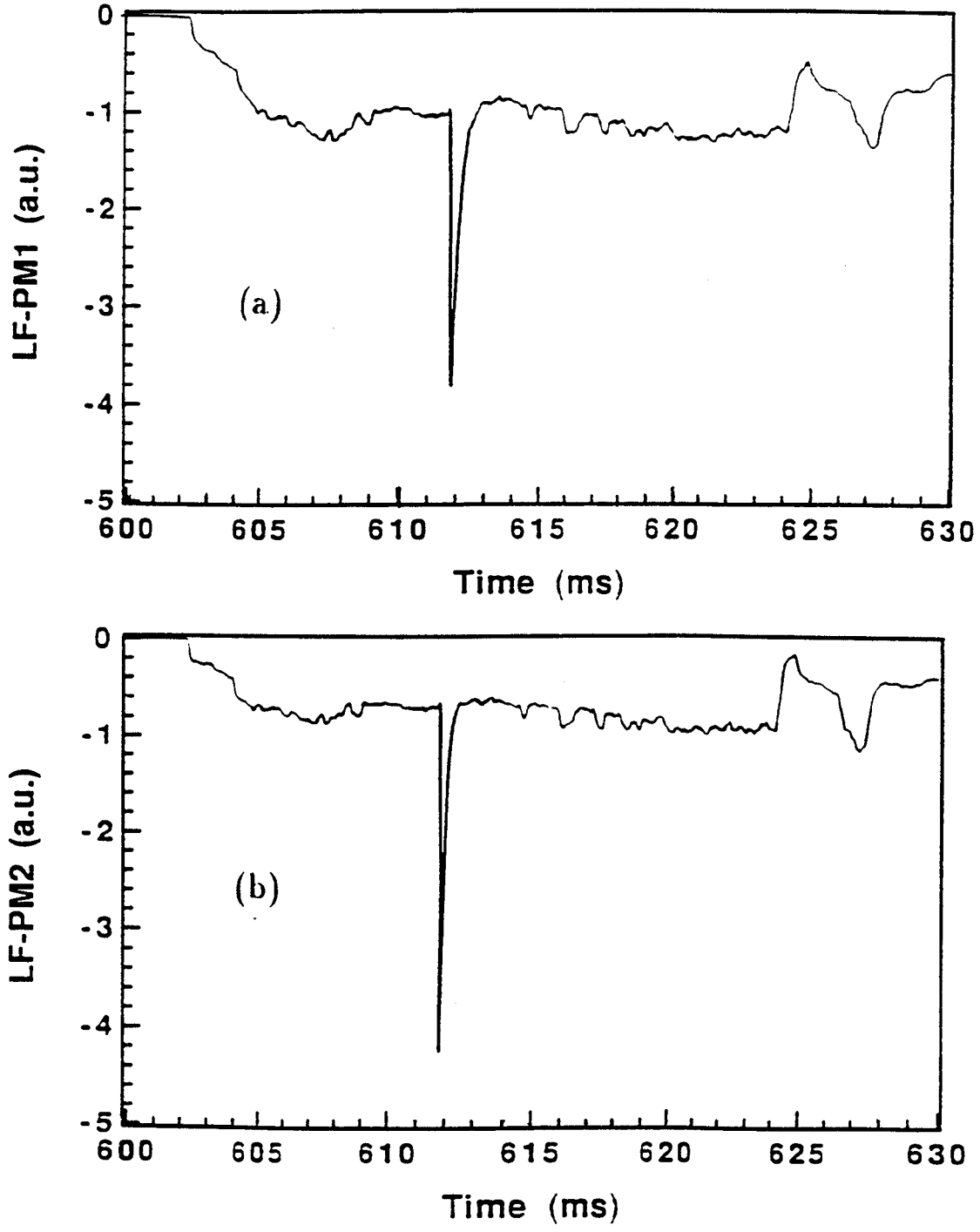

Figure 26: The signal through path PM1 (H_α , background light and stray laser light and the signal through path PM2 (The laser induced fluorescence light the stray light, H_α and background light.

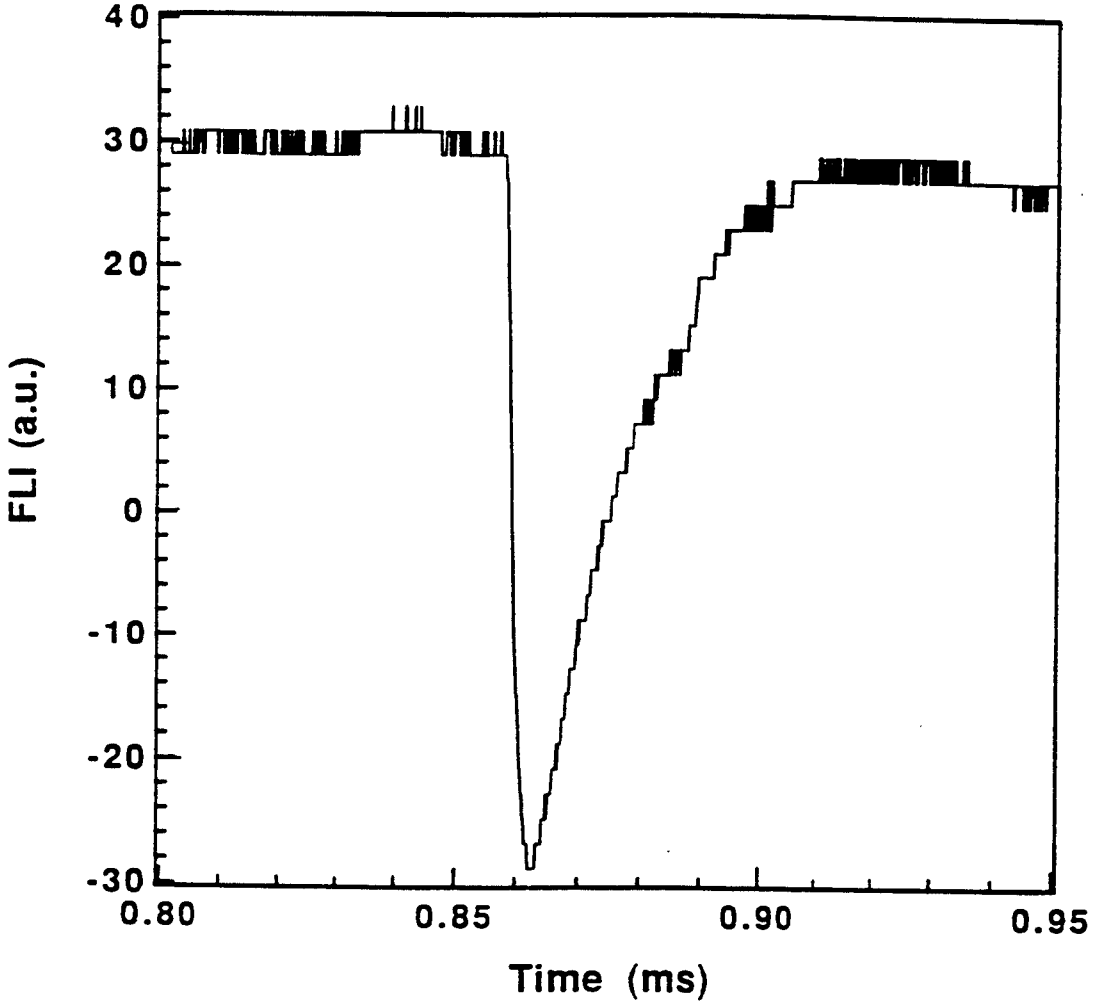

Figure 27: Fluorescence light spectrum produced by the TOP method.

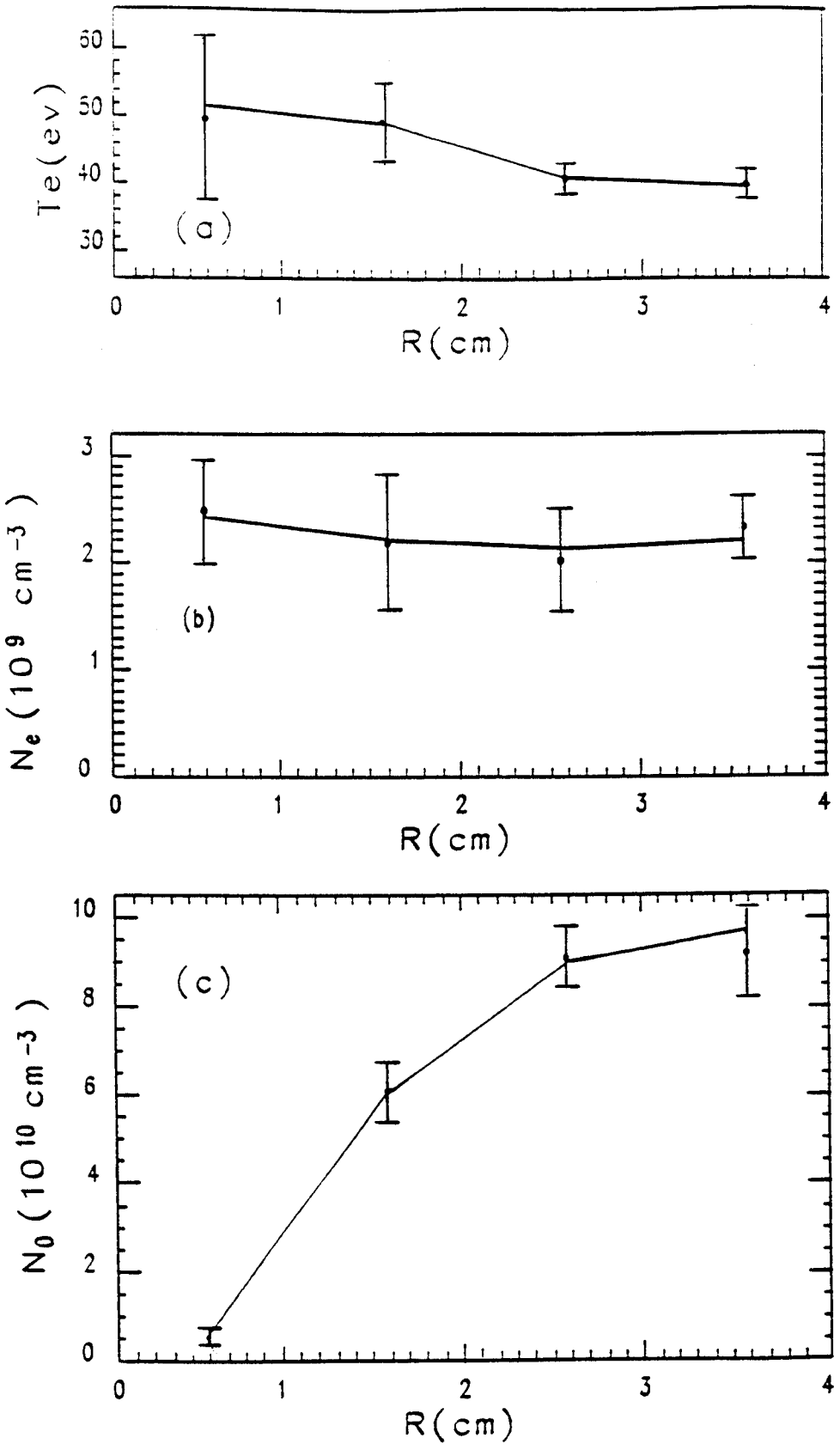

Figure 28: The electron temperature T_e, density n_e, and neutral density n_o in the exhaust chamber

6 Experimental Study

The experimental setup is shown in figure 2. The wave is launched from the antenna in the high field region and propagates toward the resonance plane and inward toward the axis. The measurements were made at the resonance plane where the diagnostics are currently located.

6.1 Diagnostics

In order to successfully carry out the experiments described in here we have to continuously develop new diagnostics. Following are the ones that were developed this year:

1. A retarding field grid energy analyzer has been built and tested successfully. However, funding limitations have prevented us from acquiring the necessary function generator and power supply to bring this unit on line.

2. A wave propagation B-dot probe array consisting of five evenly spaced detectors has been built and installed. The axial profile of the B-field measurement was made using this array.

3. A triple Langmuir probe for electron density and temperature measurements has been built, tested and has been used for experiments. A careful calibration with single probe measurements has to be made.

4. An entirely new E-probe has been successfully developed. This makes the measurement of the electric field component of the wave possible for the first time.

5. A laser fluorescence system to measure neutral density has been made operational and has been used for the exhaust study.

6. A Doppler broadening spectral meter has been developed. This system will be used for ion temperature measurement.

6.2 ICRF Wave Experiment

The experimental setup is shown in figure 29 (Note the slightl different illustration from Figure 2). The wave is launched from the antenna in the high field region as indicated and propagates toward the resonance plane and inward toward the axis. The measurements were made at the resonance plane where the diagnostics are currently located. The magnetic component of the wave is measured by a B-dot probe array. The electric component is measured by an E probe. The density is measured by both Langmuir probe and microwave interferometer. The numderical simulation region is shown by the shaded area.

The electron density of the plasma at two different ICRF frequencies was measured with a microwave interferometer and is shown in figure 30. The characteristics of the density

results shows the phenomena of the existence of two types of discharges observed from the H_α emission [6]. Figure 30a shows the discharge for $\omega > \omega_{ci}$ and is classified as type I, whereas figure 30b shows the discharge for $\omega < \omega_{ci}$ and is classified as type II. Type II discharge is more quiescent than type I.

Type I discharges generate densities that are lower than type II discharges. The peak line density obtained from the interferometer is approximately $3.2 \pm 0.85 \times 10^{12}\text{cm}^{-2}$, which corresponds to a plasma density of approximately $1.6 \pm 0.42 \times 10^{11}\text{cm}^{-3}$. The average line density is approximately $2.6 \pm 0.85 \times 10^{12}\text{cm}^{-2}$ or $1.3 \pm 0.42 \times 10^{11}\text{cm}^{-3}$. The uncertainty is due to both pickup as well as the resolution of the phase digitizer.

The radial profile of B_z of the wave for the the type II discharge measured by a single B-dot probe at midplane is shown in figure 31. The solid curve is the numerical results and the open circles with crosses are the experimental data. They are in good agreement.

The axial profile of B_z of the ICRH wave for the type II discharge measured by the B-dot probe array is shown in figure 32a. It is seen that the wave is damped as it travels toward the resonance plane. The numerical simulation of the wave was presented previously [6] and a trimetric view of the calculated B_z is shown in 32b. The corresponding region of the axial profile measured by the B-dot probe array is indicated in figure 32b as the damped region between the peak and resonance plane. The wave is rising to a peak and is then damped toward the resonance plane in agreement with the experimental data. Such a damping effect is also predicted by the analytic solution discussed in the theoretical analysis section.

To determine a range of stable operating conditions, a series of experiments at various magnetic fields was performed to see the effect of the magnetic field intensity on the stability of the plasma. Instability occurs at low field. Figure 33 shows triple Langmuir probe data illustrating this effect. From top to bottom, the plasma stability improves when the field intensity increases (as is indicated by the increasing values of coil current).

6.3 Propulsion Parameters

It is our plan to carry out a series of of experiments by making simultaneous measurements with all the diagnostics on line. To do so the machine has to be modified to increase the number of ports and more data acquisition equipment have to be acquired. In this experiment we try to utilize our existing resources to obtain the badly needed propulsion parameters. In order to extract the propulsion parameters we need to know, at least, the electron and ion temperature, the electron and ion density, the radiation losses, the gas pressure, the mass flow-rate and thrust. These measurements were taken simultaneously with a fast Langmuir probe, a triple Langmuir probe, a Doppler broadening spectral meter, radiation monitors, a residue gas analyzer, fast pressure gages and the ballistic thrust balance just developed for this purpose. A typical plasma shot is shown in Figure 34. The top two signals are triple probe measurements and the third signal is electron saturation current of a Langmuir probe. The H_α radiation from hydrogen atoms is shown in Figure 34 (fourth signal) without scanning. The bottom signal in this figure is the Doppler broadened line scanned by the rotating mirror. This line was obtained with entrance slit of the spectrometer set wide open, in order to admit enough light to see the line, thereby the resolution is very poor. The

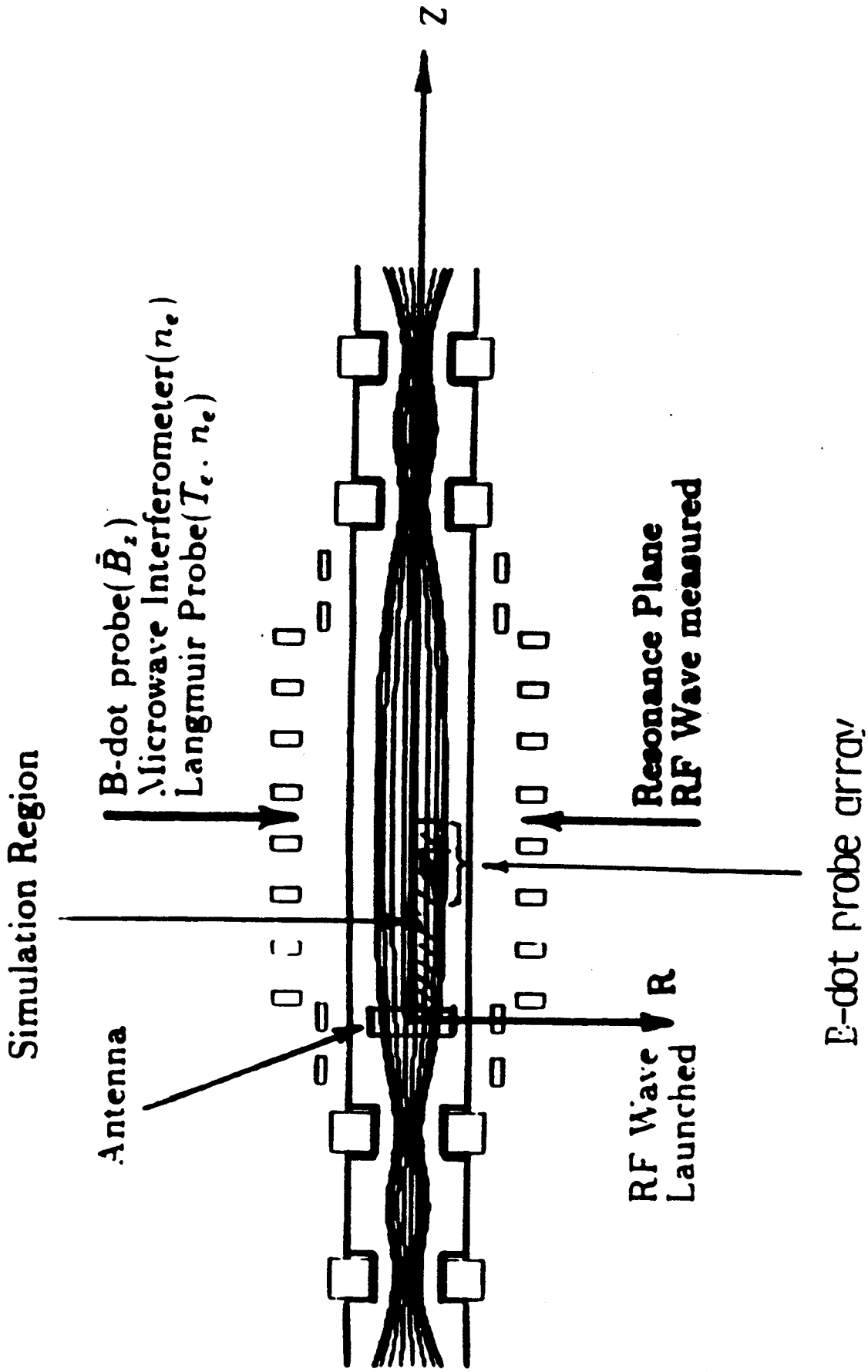

Figure 29: Simplified experimental setup for ICRF wave propagation and heating experiment. The shaded area is the numerical simulation region

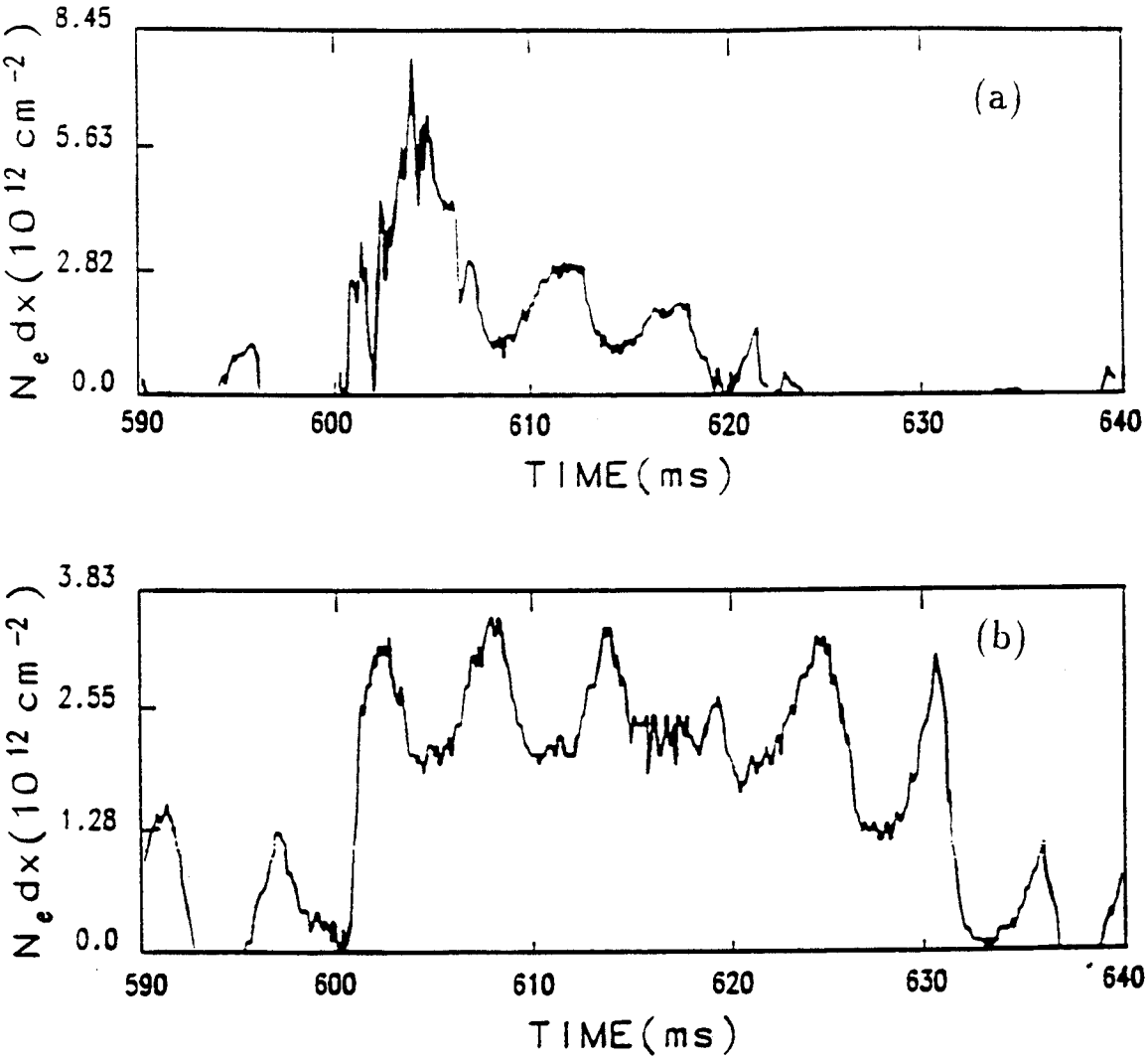

Figure 30: Plasma density measured by interferometer for (a)type I discharge ($\omega > \omega_{ci}$), and (b) type II discharge ($\omega < \omega_{ci}$)

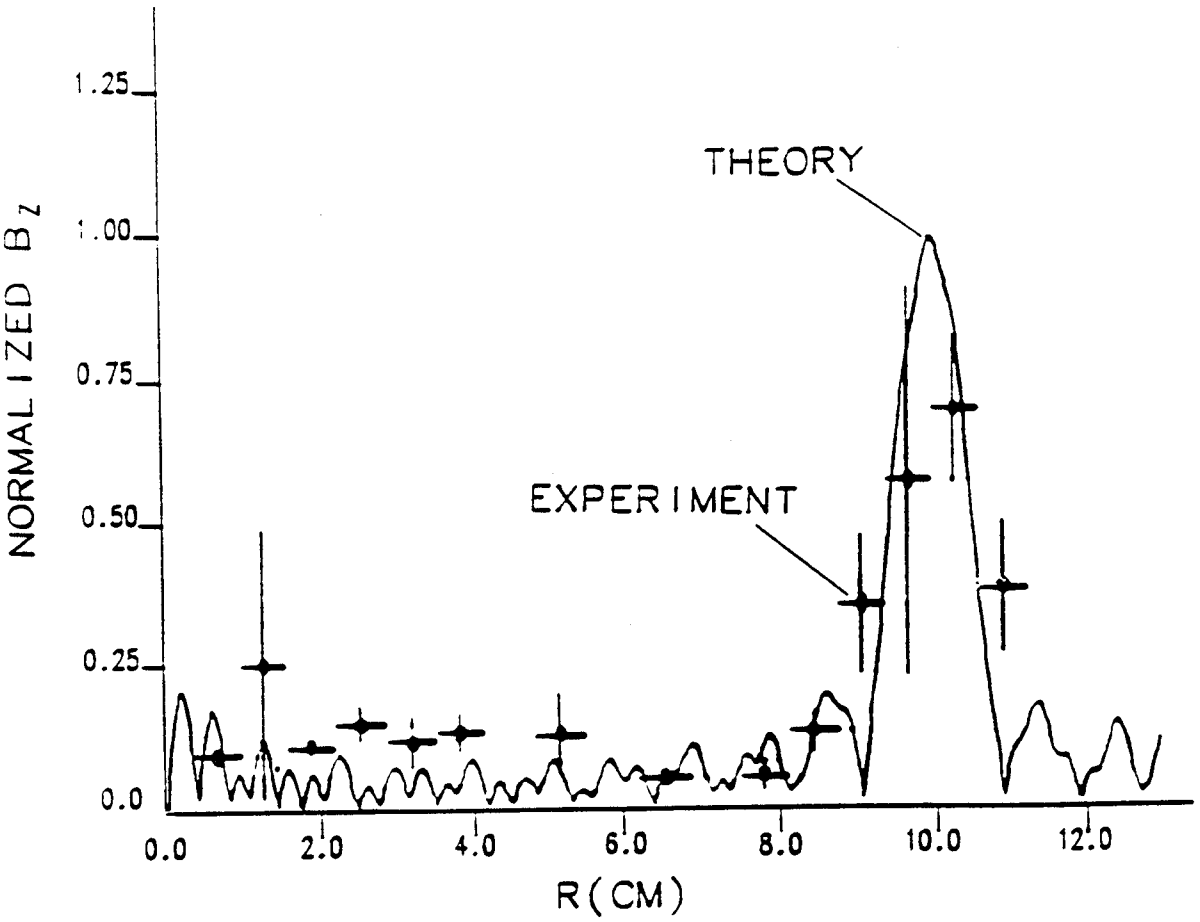

Figure 31: Radial B_z profile for type II discharge

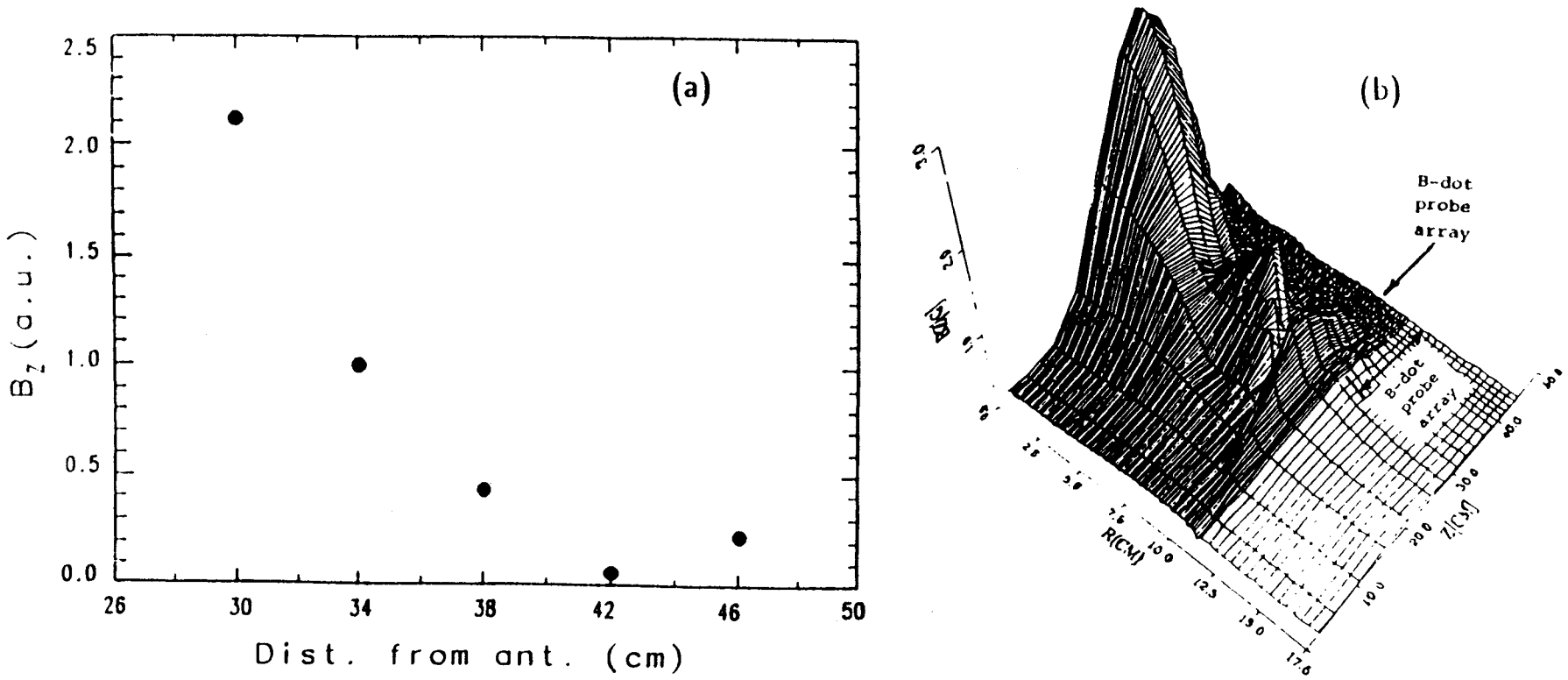

Figure 32: Axial B_z profile for type II discharge (a) and the plasma damping of B_z as shown by the numerical simulation (b).

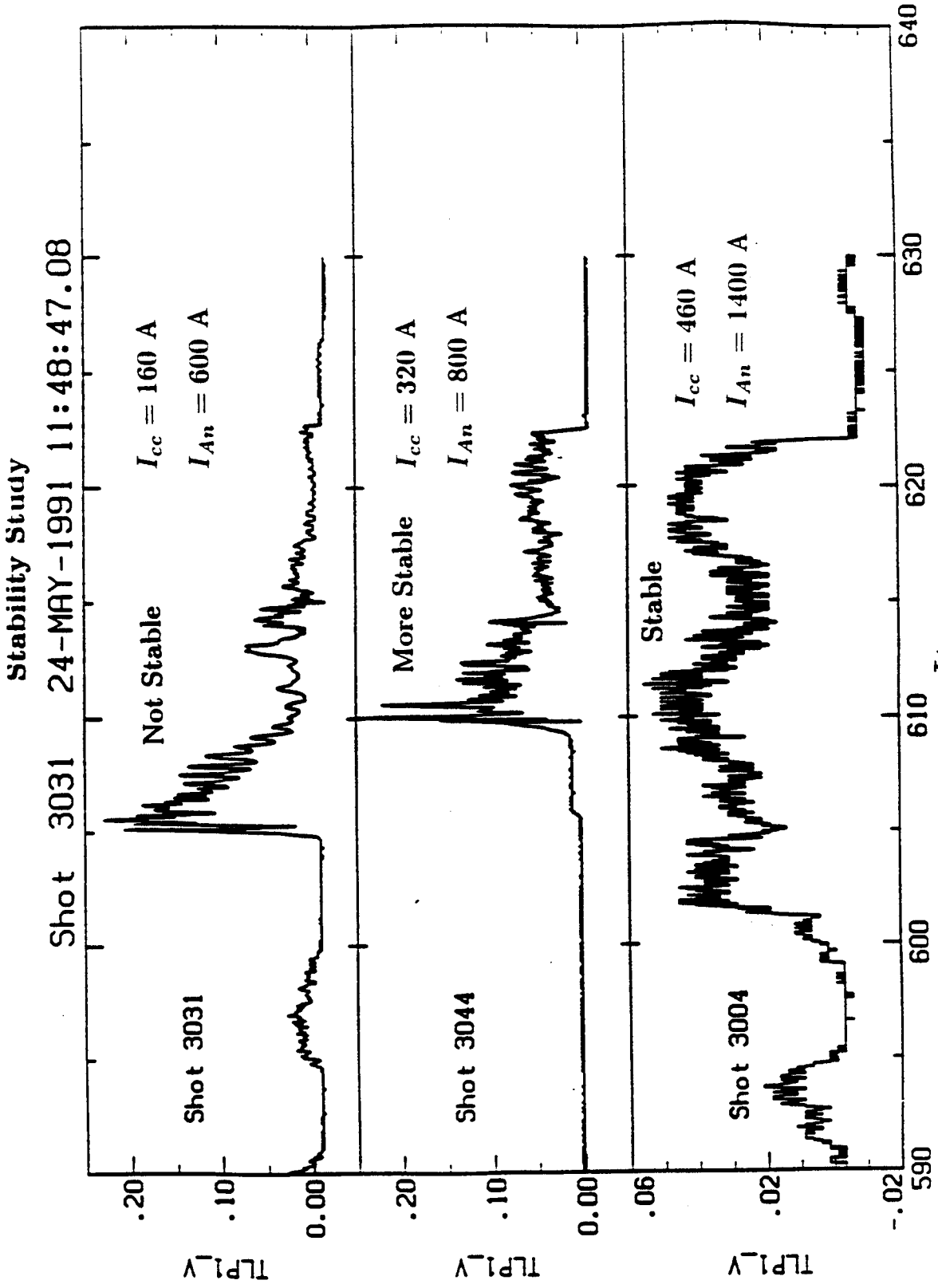

Figure 33: Steability study

deduced hydrogen temperature is not reliable. In order to obtain a high solution spectral line we have to deliberately create a radiative plasma. Also, for the purpose of measuring the ion temperature we have to seed the hydrogen plasma with helium. Again the radiation from the helium ions is very weak. We have not yet found a means to enhance the radiation strong enough to permit a meaningful measurement. This is a strong indication of low radiation losses from the plasma. The Plasma and Propulsion parameters are listed in Table 2 and their implication has been discussed in the progress summary section.

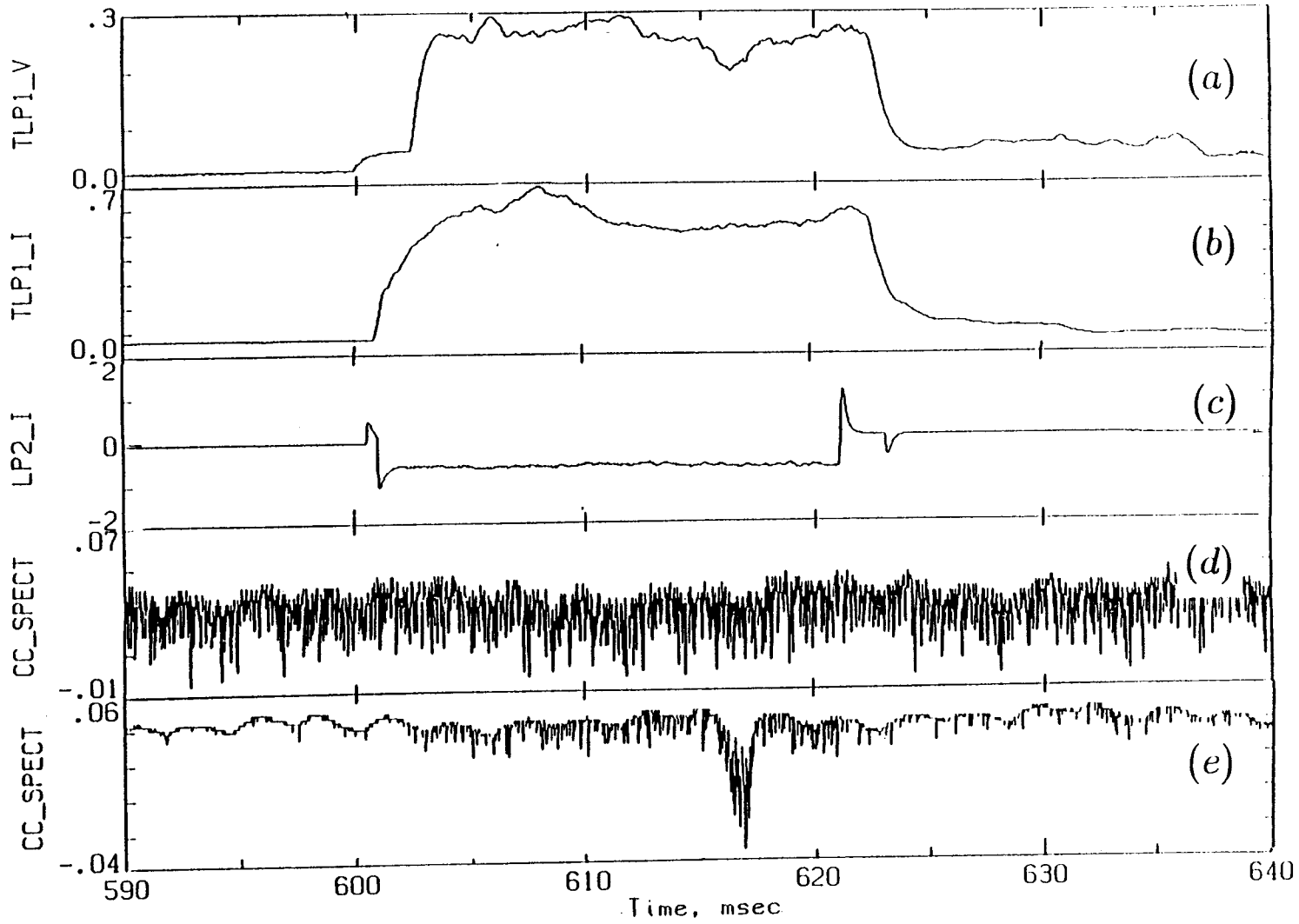

Figure 34: Sample probe signals of the plasma discharge: (a) triple probe voltage signal, (b) triple probe current signal, (c) the Langmuir probe saturation current signal, the fourth signal (d) and fifth signal (e) are the H_α radiation and Doppler broadened line spectrum.

7 Flight System Study

We have undertaken a flight system design study and mission analyses (postulating a piloted Mars mission at 10 MWe and 50% efficiency)[11]. The preliminary results are very attractive. Figure 35 shows the extrapolated operational envelope for this system. I_{sp} variations between 2,000 and 20,000 s can be obtained while the available thrust varies between 10,000 N and 10 N for hydrogen propellant. This is a unique feature for this propulsion system. The thrust is very large at low I_{sp}, and decreases as the vehicle gains speed (low thrust at high I_{sp}). Such a capability can not be found in most other types of propulsion schemes where high thrust is always associated with high I_{sp}. Therefore the vehicle can be flown at constant acceleration for continuous optimization of propulsive efficiency. The thrust can be further increased by using heavy elements such as argon or cesium as propellant at low temperature. The major advantage of cesium is that it can be preionized with waste heat from the power generator and other equipment such as rf transmitters.

Figure 36 illustrates one possible system layout. For a 10 MW flight system the rocket itself has a specific weight of 0.04 kg/kW while the rf system is 4 kg/kW. Using an existing space nuclear electric system design from Rocketdyne [23] we arrive at an overall figure of 8.04 kg/kW making the variable I_{sp} rocket very competitive. The general subsystem specific weight breakdown is shown in Table 3. These preliminary calculations, based on reproducible experimental results, open the way for a more in-depth subsystem design. This effort is ongoing albeit limited by manpower constraints.

Initial calculations performed recently for our group by J. Gilland and C. Hack of NASA/Lewis [12] indicate an attractive 150 day transit to MARS. The total trip time is 480 days including a 90 day stay on MARS. The calculations used an input value of 8 kg/kW and an efficiency of 50%. Since then, experimental results and hardware design modifications have allowed us to refine the subsystem specific weight estimates, as well as to consider a more realistic efficiency value of 70%.

From the mission analysis results shown in Figure 37, one sees the I_{sp} variation during both the accelerating and decelerating phases of the flight leading to the capture of the vehicle in the MARS orbit in all cases. Thrust system design refinement using state-of-the-art superconducting technology as well as a more careful evaluation of the structural requirements in a space-borne system, have led to a much more compact and lightweight device. This evolution is shown in Figure 38 which compares the experimental device to the optimized flying system. The experimental device is made from copper and stainless steel. The coils are discrete and large, therefore heavy support structure is necessary, whereas for the flying system the coils are superconductor and the chamber and coil casing are aluminum. The overall size of the coils is reduced by a factor of four. Therefore the system is much more compact and weighs only one fifth of our experimental device. A conceptual picture of the rocket is shown in Figure 39.

Table 3: Specific Weight of The Subsystems

Plasma Rocket	0.04 kg/kWe
RF Transmitter	4.0 kg/kWe
Nuclear Electric Power	4.0 kg/kWe
Overall specific weight	8.04 kg/kWe

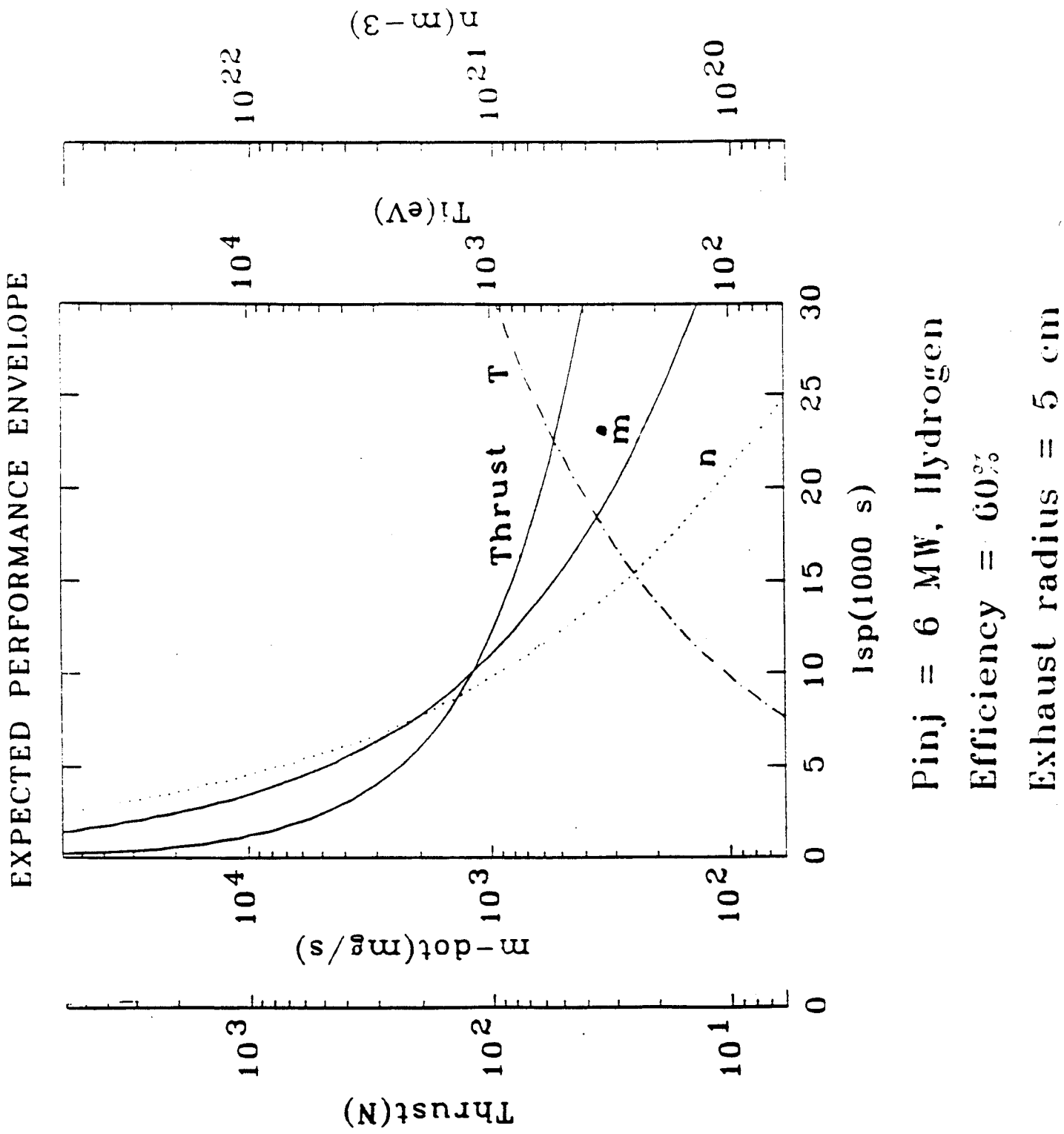

Figure 35: An extrapolated operational envelope for a 10 MWe propulsion system.

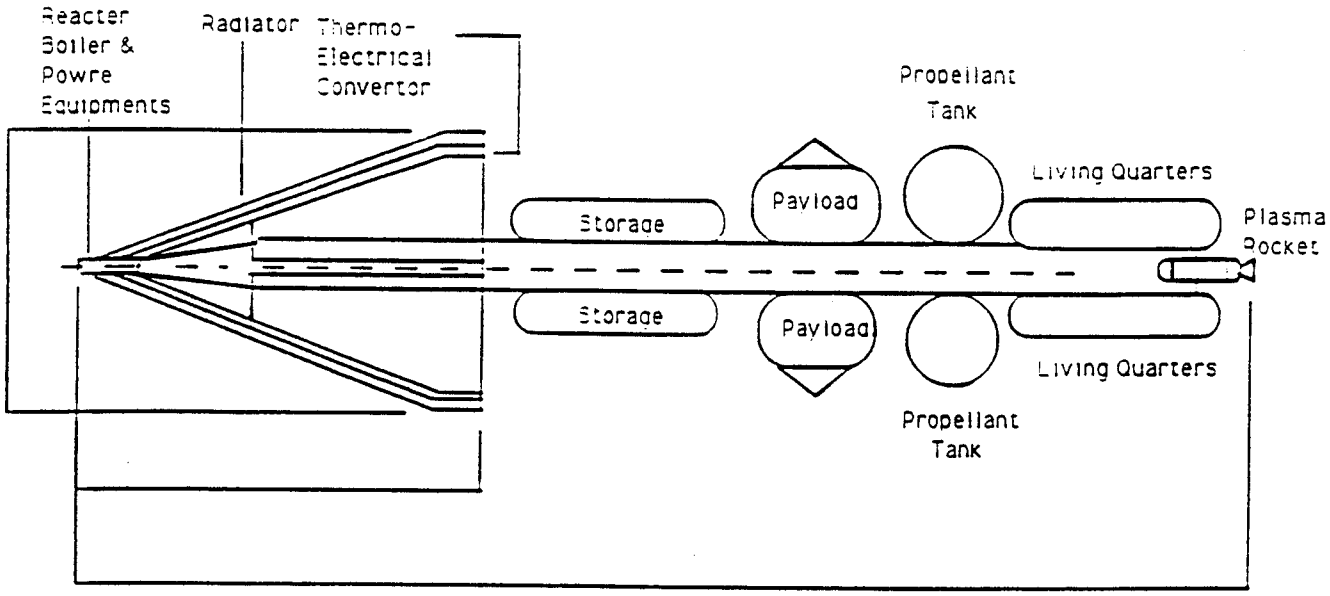

10 MWe Variable Isp Plasma Rocket Vehicle Configuration

Figure 36: Sketch of a flight system incorporating the Tandem Mirror Rocket.

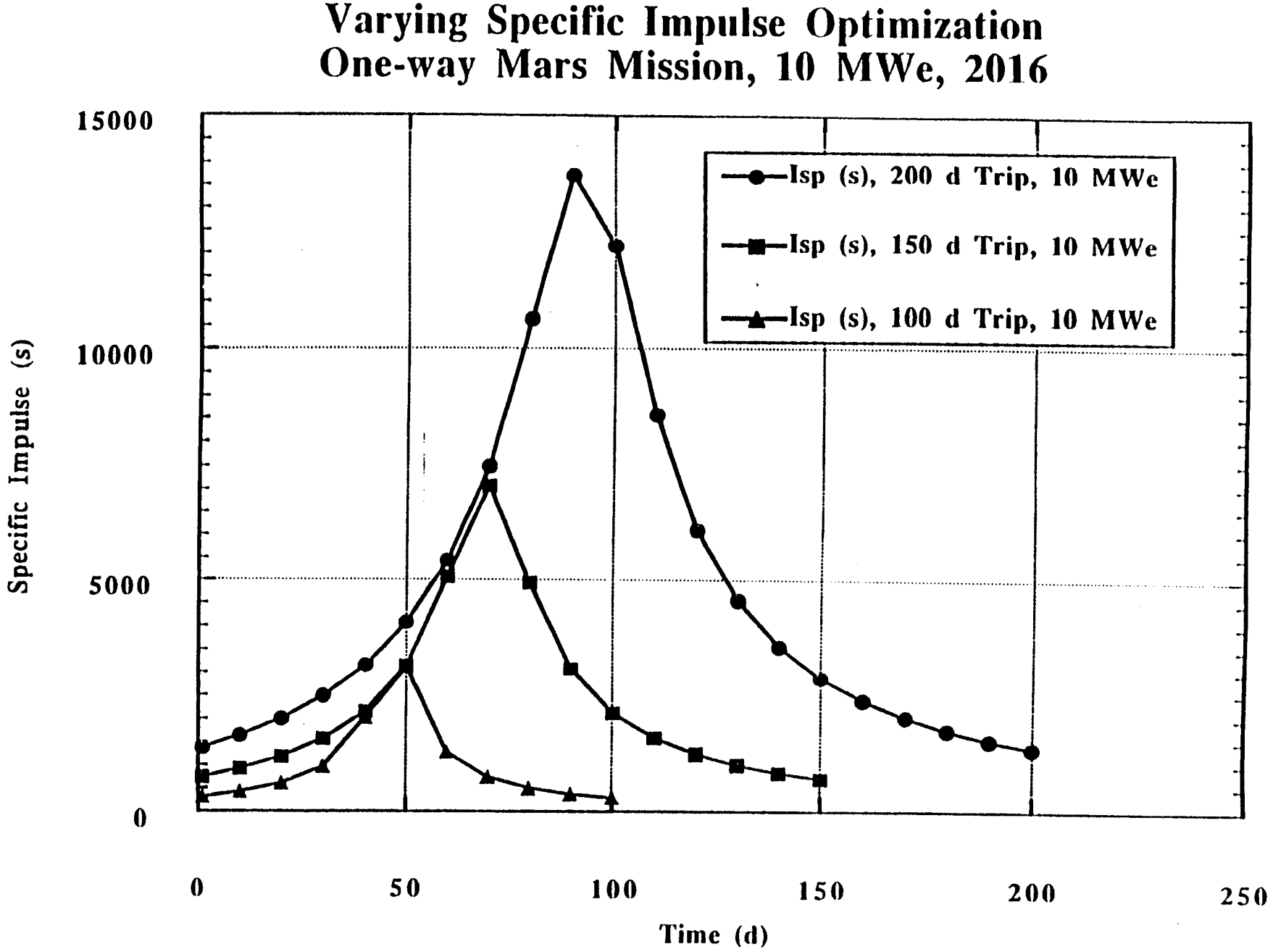

Figure 37: An example of mission analysis[Gilland].

(a) Experimental Device.
Copper magnet, S.S chamber.
Weight: 1783 kg.
Specific weight: 0.17 kg/KW.

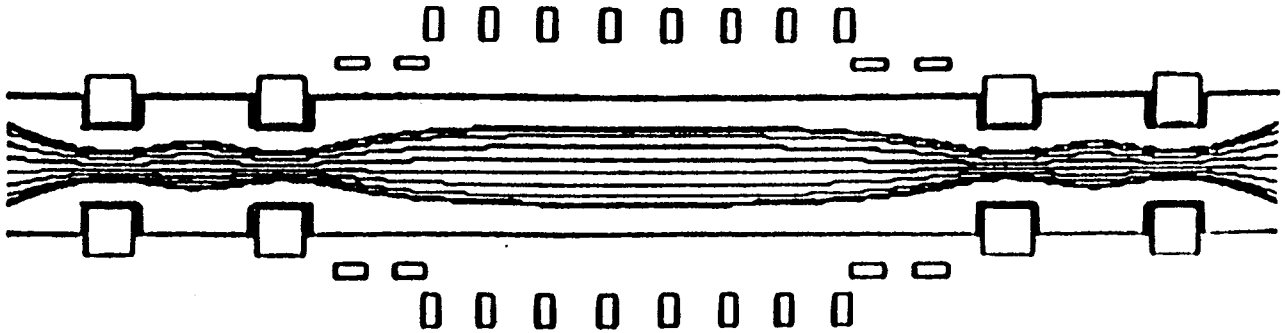

(b) A Flying Device.
Superconducting magnet, Al chamber.
Weight:399 kg.
Specific weight: 0.04 kg/KW.

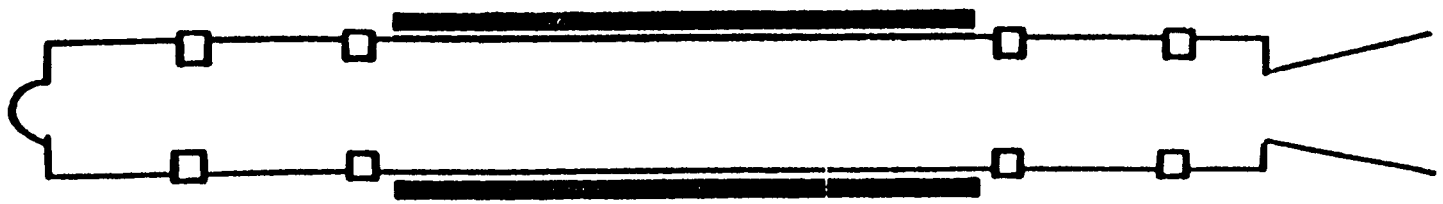

Figure 38: A 10 MW Tandem Mirror Plasma Propulsion System: (a) Experimental device, and (b) Flying device.

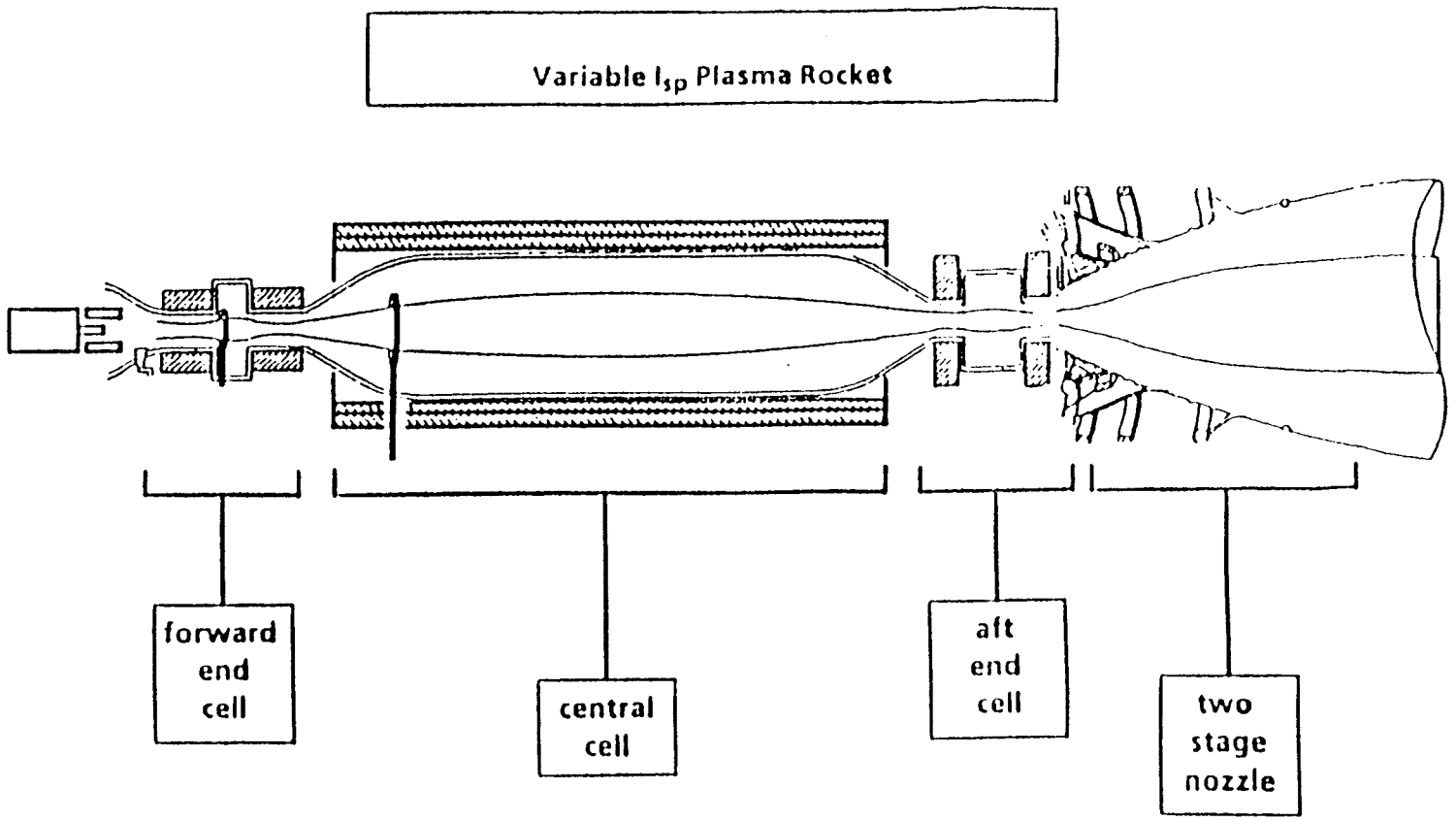

Figure 39: A conceptual tandem mirror rocket.

8 Exhaust Modeling

To model the exhaust a time dependent, three fluid (electron, ion and neutral) code by solving transport equations in cylindrical geometry including interactions between species has been developed. We began to learn the dynamic behavior of the plasma-gas system. The theory and the simulation method are described below.

The macroscopic quantities (n,V, and T) are modeled via a fluid representation. The basic equations can be obtained from the work of Braginskii [24]. Braginskii assumed that there was no processes that convert particles of one species to another, so the right hand side of his particle conservation equation, for example, is set to zero. We have such processes, and must generalize the equations appropriately. We need fluid equations for the conservation of particles, momentum, and energy. The equations to be presented will be for the plasma ion species. The equations for electron species are identical. The equations for the neutral gas are the same, except for the momentum conservation equation, which lacks the Lorentz force term. To close the fluid equations, we need an equation of state to specify the relation between pressure and temperature.

8.1 The Transport Equations

The equation for conservation of particles is (Eq. (1.11) of Braginskii on page 225 in reference [24])

$$\frac{\partial n}{\partial t} + \nabla \cdot (n\mathbf{V}) = S_p \tag{33}$$

Here n is the particle density and $\mathbf{V}$ is the mean fluid velocity, defined as

$$\mathbf{V} = \langle \mathbf{v} \rangle \tag{34}$$

$\mathbf{v}$ is the exact particle velocity, and the $\langle \cdot \rangle$ denotes an average over velocity space. S_p is the particle source term, to be described in detail later.

The equation for the conservation of momentum is (Eq. (1.12) of Braginskii in reference 7)

$$\frac{\partial}{\partial t}(mn\mathbf{V}) + \nabla \cdot (mn \langle \mathbf{vv} \rangle) - en\left(\mathbf{E} + \frac{1}{c}\mathbf{V} \times \mathbf{B}\right) = \mathbf{R} \tag{35}$$

Here $\mathbf{v} = \mathbf{v}' + \mathbf{V}$, the exact particle velocity, and $\mathbf{v}'$ is a random velocity.
Ignoring viscosity, this becomes:

$$\frac{\partial}{\partial t}(mn\mathbf{V}) + \nabla \cdot (mn\mathbf{V}\,\mathbf{V}) + \nabla p - en\left(\mathbf{E} + \frac{1}{c}\mathbf{V} \times \mathbf{B}\right) = \mathbf{R} \tag{36}$$

where m is the mass of a particle, c is the speed of light, p is pressure, $\mathbf{E}$ is the electric field and $\mathbf{B}$ is the magnetic field. $\mathbf{R}$ is the source of momentum, to be described in detail later. Note that both of these equations are in conservative form, and this is the way that they are numerically differenced in the code.

For conservation of energy, we start from the heat-balance equation, (Eq. (1.23) of Braginskii in reference [24])

$$\frac{3}{2}\frac{\partial nT}{\partial t} + \nabla \cdot \left(\frac{3}{2} nT\mathbf{V}\right) + nT\nabla \cdot \mathbf{V} + \Pi : \nabla \mathbf{V} + \nabla \cdot \mathbf{q} = Q \tag{37}$$

Here $\mathbf{q}$ is the heat flux and Π is the viscosity tensor. Q is the heat source term, to be described in detail later. Ignoring viscosity, this becomes

$$\frac{3}{2}\frac{\partial nT}{\partial t} + \nabla \cdot \left(\frac{3}{2} nT\mathbf{V}\right) + nT\nabla \cdot \mathbf{V} + \nabla \cdot \mathbf{q} = Q \tag{38}$$

The second term can be divided as follows:

$$T\nabla \cdot n\mathbf{V} + n\mathbf{V} \cdot \nabla T \tag{39}$$

The first term above can be combined with the appropriate time derivative term of Eq. (8) to give the continuity equation scaled by T.

$$\frac{3}{2}T\left(\frac{\partial n}{\partial t} + \nabla \cdot nV\right) = \frac{3}{2}TS_p \tag{40}$$

Writing

$$Q^* = Q - \frac{3}{2}TS_p \tag{41}$$

and dividing Eq. (8) by $(3/2)\,n$ leaves us

$$\frac{\partial T}{\partial t} + \mathbf{V} \cdot \nabla T + \frac{2}{3}T\nabla \cdot \mathbf{V} = \frac{2}{3n}(Q^* - \nabla \cdot q) \tag{42}$$

The second and third terms can be rewritten as

$$\nabla \cdot (T\mathbf{V}) - \frac{1}{3}T\nabla \cdot \mathbf{V} \tag{43}$$

This leads to the following equation for temperature:

$$\frac{\partial T}{\partial t} + \nabla \cdot (T\,\mathbf{V}) - \frac{1}{3}T\,\nabla \cdot \mathbf{V} = \frac{2}{3n}\,(Q^* - \nabla \cdot \mathbf{q}) \tag{44}$$

Heat conduction is dominated by the electrons, and thus $\mathbf{q}$ is only present in the electron temperature equation, or, $\mathbf{q} = \mathbf{q}_e$. The form for $\mathbf{q}_e$ is:

$$\mathbf{q}_e = \kappa_\perp^e \nabla_\perp (kT_e) \tag{45}$$

Here k is Boltzman's constant. $\kappa_\perp^e$ is the perpendicular electron thermal conductivity and is given as

$$\kappa_\perp^e = 4.7\frac{nkT_e}{m_e\omega_{ce}^2\tau_e} \tag{46}$$

Here ω_{ce} is the electron gyrofrequency and τ_e is the basic collisional time.

To close the fluid equations, the equation of state for pressure is

$$p = nkT \tag{47}$$

8.2 The Source Terms

The source terms are from various collision processes with the neutral gas, including atomic reactions. The details of the various source terms will now be presented.

The atomic reactions included here are ionization, charge-exchange and recombination and are characterized as follows.

Electron Impact Ionization:

$$e + H^o \rightarrow H^+ + 2e \tag{48}$$

Resonant charge–exchange:

$$\overset{\text{hot}}{H^+} + \overset{\text{cold}}{H^o} \rightarrow \overset{\text{cold}}{H^+} + \overset{\text{hot}}{H^o} \tag{49}$$

Collisional–radiative recombination:

$$e + H^+ \rightarrow H^* + h\nu \tag{50}$$

and electron three–body recombination:

$$e + H^+ + e \rightarrow H + e \tag{51}$$

In the recombination reactions above, the names describe the way the energy released by the recombination is carried away. H^* is an excited state, and $h\nu$ represents photons.

The particle source term, S_p, consists of sources from atomic reactions between the plasma and the neutral gas, which can be broken into three terms

$$S_p = S_{\text{ion}} + S_{\text{cx}} + S_{\text{rec}} \tag{52}$$

Here S_{ion} is the source of particles from electron impact ionization, S_{cx} is the source of particles from resonant charge-exchange and S_{rec} is the source of particles from the recombination reactions.

The specific particle source terms have the following form:

$$S_{\text{rx}} = n_1 n_2 \langle \sigma v \rangle_{\text{rx}} \tag{53}$$

n_1 and n_2 are determined by the species involved in the reaction. $\langle \sigma v \rangle_{\text{rx}}$ is the reaction-rate for the specific reaction. The reaction-rates have been previously calculated and stored in a lookup table to be used by the code. The cross-section, σ, is temperature dependent. The average reaction-rates $\langle \sigma v \rangle$ was calculated assuming a Maxwellian velocity distribution for both species involved in the reaction.

The momentum source term has the same form as the particle source term. Specifically,

$$R = R_{\text{ion}} + R_{\text{cx}} + R_{\text{rec}} \tag{54}$$

The R's represent the source of momentum from the various atomic reactions,or:

$$R_{\text{rx}} = (m\mathbf{V})_1 \, n_1 n_2 \langle \sigma v \rangle_{\text{rx}} \tag{55}$$

In addition, the $\mathbf{R}$ term contains elastic collisions between the plasma and neutrals, i.e., collisions that do not lead to atomic reactions. These elastic collisions are commonly referred to as friction. The frictional momentum transfer can be modeled as (for ions scattering off of neutrals)

$$R_{\mathrm{f,in}} = mn\left(V_n - V_i\right)\nu_{in} \tag{56}$$

where ν_{in} is the collision frequency for scattering of ions by neutrals.

From momentum conservation we know that $R_{\mathrm{f,in}} = R_{\mathrm{f,ni}}$. Electrons also scatter elastically from the neutrals, but in the hybrid model, this is taken into account in the term for the plasma's resistivity (to be described later).

The last source term to consider is the source term for internal energy, Q. This includes the internal energy brought in via atomic reactions,

$$Q = Q_{\mathrm{ion}} + Q_{\mathrm{cx}} + Q_{\mathrm{rec}} \tag{57}$$

Each Q has the form

$$Q_{\mathrm{rx}} = \left(\frac{3}{2}nkT\right)_1 n_1 n_2 \langle\sigma v\rangle_{\mathrm{rx}} \tag{58}$$

For the ions there is an additional term for ion heating from the electrons

$$Q_i = \frac{3m_e}{m_i}\frac{nk}{\tau_e}\left(T_e - T_i\right) \tag{59}$$

Electromagnetic Terms

All that is left is to find equations for $\mathbf{E}$ and $\mathbf{B}$. vIn a hybrid plasma model, both come from the electron momentum equation.

In the limit of small electron inertia, the electron momentum equations reduced to

$$\mathbf{E} = -\frac{\nabla nkT_e}{en} - \frac{1}{c}\mathbf{u}_e \times \mathbf{B} + \eta\mathbf{J} \tag{60}$$

where η is the plasma resistivity. The last term of this equation, $\eta\mathbf{J}$, is simply the $\mathbf{R}$ term in the notation used for the ion momentum equation. In other words, the friction of electrons scattering off of ions. As mentioned above, this term must also account for the scattering of electron off of neutrals. This is taken into account in the η term.

$$\eta_{total} = \eta_{en} + \eta_{ei} \tag{61}$$

The electron momentum equation can be considered the Ohm's Law for the system. It should be emphasized that the velocity in the Lorentz term of this equation is the *electron* velocity, $\mathbf{u}_e$, not the fluid velocity $\mathbf{V}$. These two velocities are related through the current,

$$\mathbf{J} = en\left(\mathbf{V} - \mathbf{u}_e\right) \tag{62}$$

or,

$$\mathbf{u}_e = -\frac{1}{en}\mathbf{J} + \mathbf{V} \tag{63}$$

Thus, the $\mathbf{u}_e \times \mathbf{B}$ term can be expanded to the form

$$\mathbf{V} \times \mathbf{B} - \frac{1}{en}\mathbf{J} \times \mathbf{B} \tag{64}$$

This second term is commonly referred to as the Hall current term. In a more familiar form, the electron momentum equation becomes

$$\mathbf{E} + \mathbf{V} \times \mathbf{B} = \eta \mathbf{J} + \frac{1}{en}\left(\mathbf{J} \times \mathbf{B} - \nabla p_e\right) \tag{65}$$

However, we will use Eq. 60 and Maxwell's equations to transform the electron momentum equation into an equation for $\mathbf{B}$.

The radiation-free limit of Ampere's law is

$$\nabla \times \mathbf{B} = \frac{4\pi}{c}\mathbf{J} \tag{66}$$

Faraday's law is

$$\nabla \times \mathbf{E} = -\frac{1}{c}\frac{\partial \mathbf{B}}{\partial t} \tag{67}$$

Introducing the magnetic vector potential ($\nabla \times \mathbf{A} = \mathbf{B}$) in the Coulomb gauge, and utilizing Maxwell's equations we can transform the electron momentum equation to

$$\dot{\mathbf{A}} = c\frac{\nabla p_e}{en} + \mathbf{u}_e \times \mathbf{B} - \frac{c^2}{4\pi}\eta\left(\nabla \times \mathbf{B}\right) \tag{68}$$

The θ component of this equation will give us both B_r and B_z. Finally, if we take the curl of the electron momentum equation, and again utilizing Maxwell's equations, we obtain the equation which was used to advance B_θ numerically.

The electron velocity components are given via the relationship between the fluid velocity and current. Specifically,

$$\begin{aligned} u_{er} &= V_{ir} + \tfrac{c}{4\pi en}\tfrac{\partial B_\theta}{\partial z} \\ u_{er} &= V_{ir} + \tfrac{c}{4\pi en}\nabla^2 \mathbf{A}|_\theta, \\ u_{ez} &= V_{iz} - \tfrac{c}{4\pi en}\tfrac{1}{r}\tfrac{\partial (r B_\theta)}{\partial r} \end{aligned} \tag{38}$$

8.3 Boundary Conditions

To complete the formulation of the problem one must specify consistent boundary conditions (BC's) for the equations discussed above. The geometry is a cylindrically symmetric duct. BC's must be specified at the inflow, z_{min}, outflow, z_{max}, $r = 0$, and the wall, r_{max}.

The inflow is assumed completely specified for the plasma and held fixed in time. The same is assumed for the neutral gas for axial injection. If radial injection is used, z_{min} becomes an *outflow* boundary for neutrals, also to be described later.

At the origin, $r = 0$, all quantities are assumed symmetric in θ which leads to the BC $\partial/\partial r = 0$. This holds for all quantities except A_θ. The BC for A_θ is Dirichlet zero. L'Hôpital's rule is utilized to ensure the fields derived from the vector potential is appropriate.

At the wall, r_{max}, A_θ is specified. For the fluid quantities, most are set as Neumann zero. The exception is temperature. In some cases the temperature is specified.

The most difficult BC's occur at z_{max}. Conventional *outflow* boundary conditions are used for the neutral gas, e. g., simple interpolation back in z. When the same BC's are attempted for the plasma, the computation failed eventually due to the problem that the plasma fluid reflects (numerically) from the outflow boundary. Many different BC's were attempted for the plasma fluid at z_{max}. The best results were obtained by simply interpolating back up a flux surface (magnetic field line), and setting the fluid quantities constant along the field line just at z_{max}. In this sense the magnetic field line is approximating a characteristic, even though in actuality it is not. To date, the best results have been obtained using the above BC's for the system.

8.4 Discussion

Our problem is many degrees more general than a simple one fluid MHD problem and is therefore many degrees more complex. Instead of solving one set of fluid equations, we are solving three sets of fluid equations – one set for ions and one set for electrons plus the neutral transport equation. Instead of steady state we are solving the time dependent problem. The reactions between species were taken into account. The coordinate system is cylindrical instead of a two dimensional Cartesian. The electron stream and the ion stream are governed by different time scales. The plasma time scale is many orders of magnitude faster than the neutral jet.

The expanded exhaust section of the mirror device is shown in Figure 40 and is marked by the coordinate axis $r-z$, where $r = 0$ is the centerline of the device. $Z = 0$ is the entrance of the plasma into the exhaust. The flowing plasma paterns for various gas injection method are presented in Figure 41. Only lower half (below the z-axis) of exhaust is displayed. The plasma is seen flowing from left to right. Figure 41a is the flow of plasma without neutrals at 3.75μs. The plasma is seen fanned out along the field lines. Figures 41b show that plasma flow with coaxial neuteral jet. The plasma was contained and boundary layer was formed. However, the neutral jet was eroded downstream and the plasma eventually spread out along the field lines (This effect is not shown here). The reason is obvious because the neutrals can not flow as fast as plasma. A steady state flow can not be maintained. Figure 41c shows density contour of plasma and neutrals when the neutral was injected radially as indicated by dashed lines and an arrow. The plasma was contained better but neutrals were eroded at the tip. Figure 41d shows the radial injection at increasing neutral density and/or jet width.

In the radial injection case the flow characteristics was further improved by increasing the width of the radial gas jet. The flow time has been extended to 23μ which is nearly steady state.

These analyses show that injection angle, gas flow rate and density are very important and need to be studied thoroughly. There is a wide range of parameter space that has to be

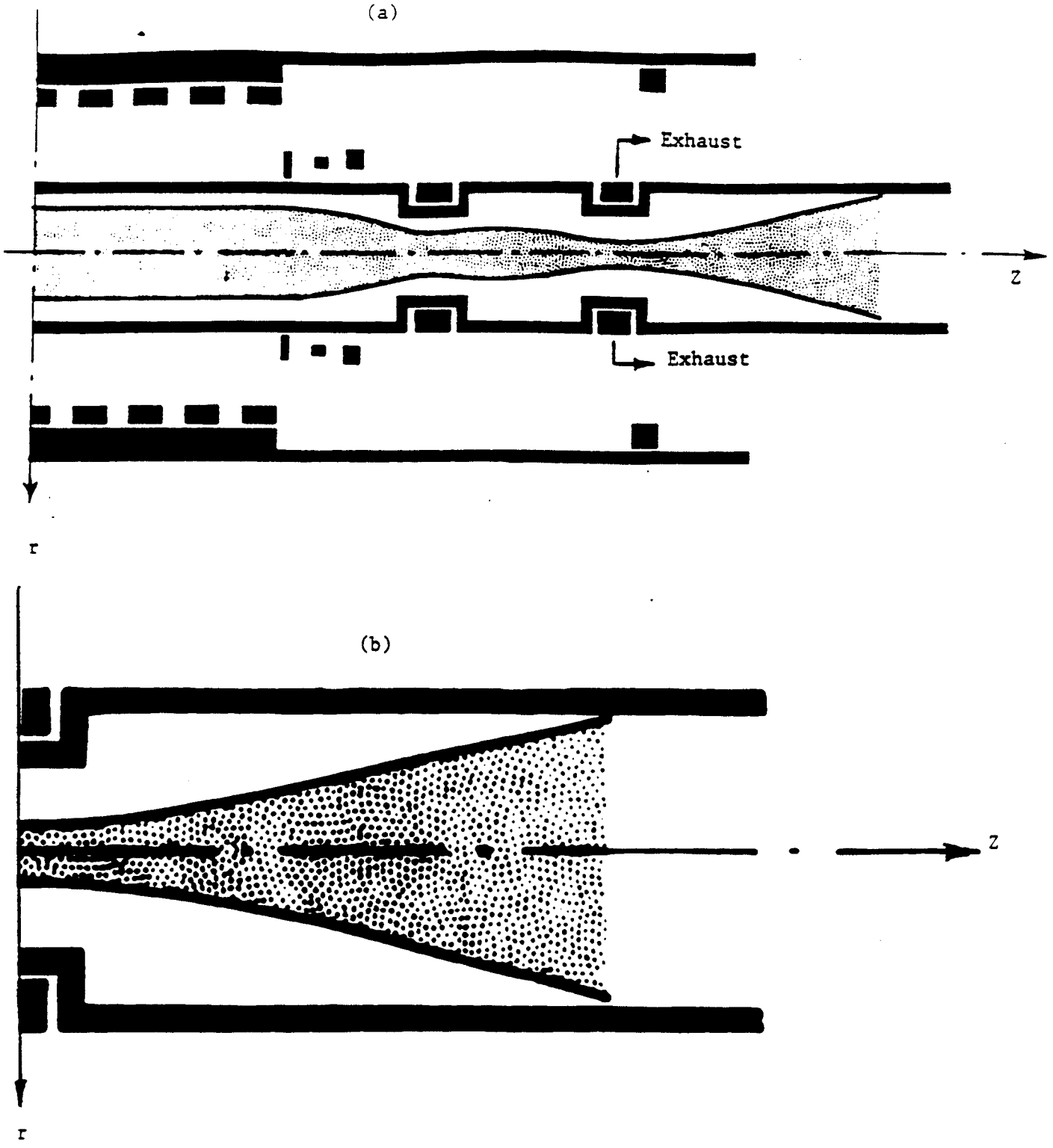

Figure 40: Plasma exhaust

covered in order to understand the dynamic properties of this plasma-gas system. However, the plasma detachment with the injection of annual cold gas is clearly demonstrated. The detachment can be further improved with a disconnected magnetic system. A disconnected magnetic system has been designed and the detachment has been demonstrated with single particl model. This work will be reported when rigorous theoretical analysis being done.

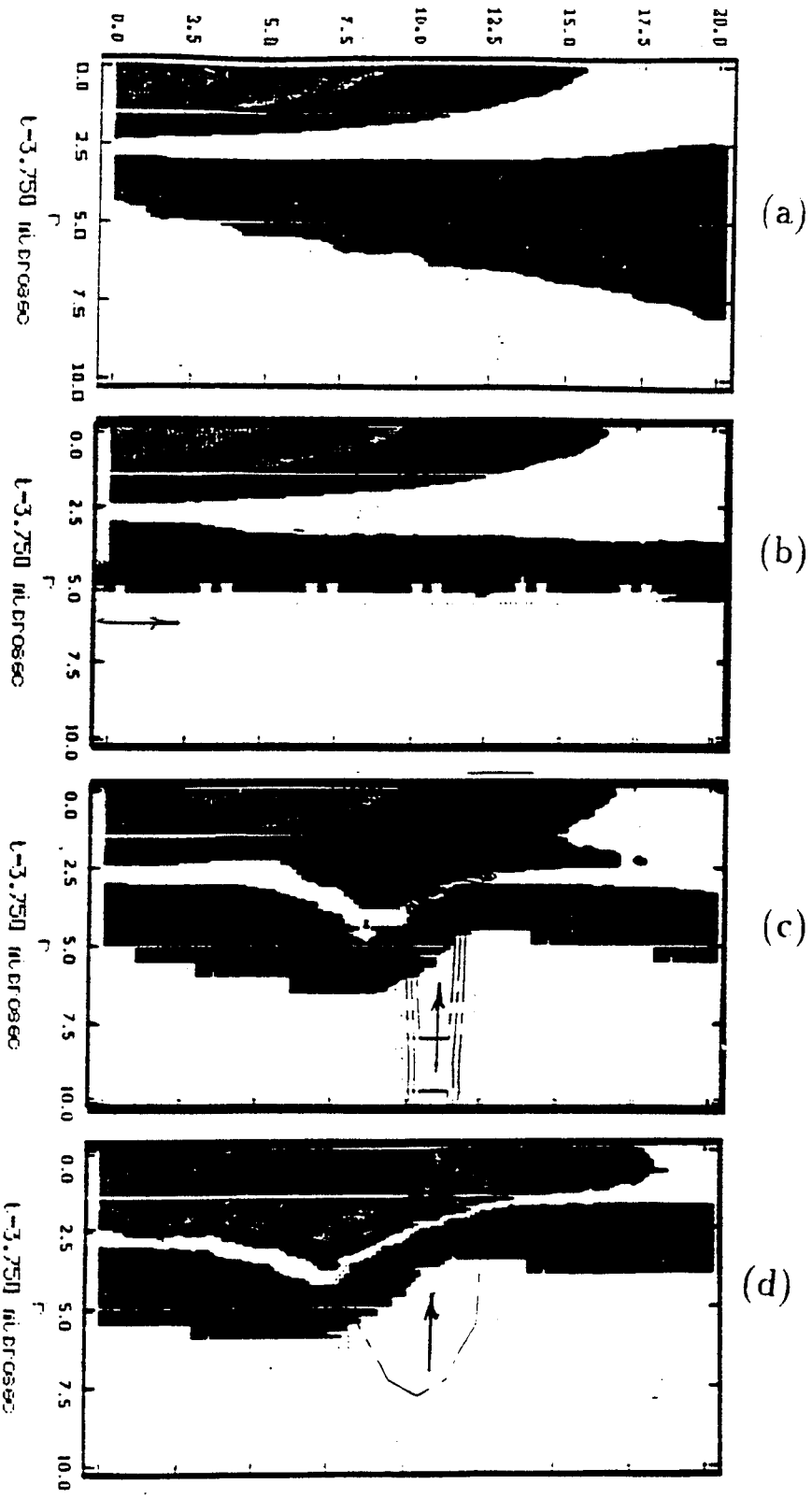

Figure 41: Plasma flow in the exhaust without gas injection (a), with axial injection (b), with radial injection (c), and with radial injection at higher density (d)

9 Future Work

To conclude this research it is useful to to give some projections and outline of possible future plan. To do so some remark on the future need of space propulsion and the capabilities of this system is in order. A new class of advanced propulsion devices is required to meet future space exploration goals including the efficient delivery of large payloads to geostationary orbit and fast manned and unmanned missions to the Moon and Mars. The variable I_{sp} tandem mirror rocket provides such capabilities by operating at high power levels ($>$ 10 MW) and high efficiency ($>$ 60%). The system is also capable of a variable thrust/I_{sp} profile which optimizes the vehicle propulsive efficiency over the entire flight.

Other distinctive features of this device further enhance its relevance as a viable propulsion method. For example, its magnetically insulated, electrodeless design greatly ameliorates materials constraints thus enabling high power operation. Systems' analyses also point to a favorable specific mass scaling ($< 6kg/kW$ at 10 MW) for a full-up superconducting design coupled to a nuclear Rankine power conversion system. Additional gains are envisioned for designs operating at higher voltages ($>$ 10 kV) and high frequencies ($>$ 500 Hz). The present experimental device has operated virtually trouble-free for over four years and continues to serve as a "pathfinder" to explore new design approaches.

In spite of these advances, multiple deficiencies in our knowledge base continue to exist for this system. For example, although high temperature/low density (high I_{sp}/low thrust) operation has now been demonstrated, it remains to be shown that this system can run efficiently in the high density/low temperature (high thrust/low I_{sp}) regime. Moreover, the well-behaved plasma conditions observed thus far need to be verified when the device operates asymmetrically in the flowing plasma mode. In addition, magnetically vectored plasma jets eventually have to detach from the guiding field to provide useful thrust. While such detachment has been shown successfully in numerical models, it has yet to be confirmed experimentally. Finally, the physics of ICRF wave propagation in tandem mirror plasmas has not been fully understood despite the achievement made in this program, such knowledge is crucial to maximizing the overall power absorption efficiency of the system over its wide operating range.

As mentioned repetitively, we would like to perform the experiment to demonstrate the plasma detachment necessary to bring this tandem mirror rocket to the mainstream of electric propulsion program. However, resource limitations have prevented us from operating in the streaming-plasma mode. This capability requires the manufacturing of a vacuum interface to the large vacuum tank in our laboratory and the design and manufacture of a propellant injector. Also, two additional magnet power supplies are required to run the system asymmetrically. The future system enhancements are highly desirable. The near term and long term research plans are presented below.

9.1 Near-Term Research

For the near future we should continue with our envelope expansion approach by validating theory over a wide operational range. Therefore the immediate next step is to carry out the experiment to increase thrust by increasing the density and reducing the temperature and to improve the energy conversion efficiency. The major equipment for this experiment is a higher frequency microwave transmitter. For this purpose a surplus 14.5 GHz microwave transmitter has been acquired and installed. Therefore no major capital investment is required except some system upgrade. Plasma parameters in the central cell will be evaluated not just at one point but as profile functions of axial and radial position. These data will continue to be used to generate engineering design guidelines applicable to spacecraft systems. In particular, an accurate characterization of efficiency and its dependence on plasma conditions will be sought. At the exhaust, the direct measurement of thrust and I_{sp} will be obtained through two detectors presently being installed: a grid energy analyzer to measure axial ion energy and ballistic balance to measure total thrust. The specific tasks are:

1. Continue envelope expansion by validating theory and experiment;
2. Obtain profile measurements of plasma parameters and characterize efficiency and its dependence on plasma conditions;
3. Obtain direct I_{sp} and thrust measurements at the exhaust with grid energy analyzer and ballistic balance.

9.2 Long-Term Research

It is fundamental to the proof-of-principle to be able to operate this device in the asymmetric, flowing-plasma mode. Such an upgrade requires two major hardware modifications: construction and installation of a vacuum interface to the vacuum plenum already available in our laboratory and the acquisition of two additional power supplies to allow independent magnetic field programming at the two end-cells. Moreover, with completion of these modifications, we would also propose the design and installation of the plasma injection system, and of the annular nozzle in order to fully test plume detachment characteristics.

In the theoretical arena we plan to continue our numerical code expansion and validation, as well as our ongoing efforts on mission design and flight system analysis. The specific goals are as follows:

1. To achieve the asymmetric, flowing-plasma mode of operation;
2. To work toward high density, low temperature, high power, high thrust operation.
3. To make four major hardware modifications:
    - Vacuum interface between system and existing plenum;
    - Upgrade of rf power transmitters;

- two additional power supplies needed for independent magnetic field programming at the end-cells.
- Design and installation of fueling injection system and of annular nozzle for flowing plasma and Carry out experimental plume detachment studies.

4. Continue the ongoing effort on code expansion and validation on the ICRF wave propagation and absorption for a wide range of plasma parameters, as well as mission and flight system design.

References

[1] F.R. Chang and J.L. Fisher. *Nuclear Fusion*, 22(8):1003, 1970.

[2] F.R. Chang, W.A. Krueger, and T.F. Yang. In *AIAA/DBLR/JSASS Int. Electric Propulsion Conference, paper AIAA-85-2049*, Alexandria, 1985.

[3] T.F. Yang, R.H. Miller, K.W. Wenzel, and W.A. Krueger. In *AIAA/DBLR/JSASS Int. Electric Propulsion Conference, paper AIAA-85-2049*, Alexandria, 1985.

[4] F.R. Chang-Díaz, T.F. Yang, W.A. Krueger, S. Peng, J. Urbahn, X. Yao, and D. Griffin. In *DGLR/AIAA/JSASS Int. Electric Propulsion Conference, paper DGLRA-88-126*, Garmisch-Partenkirchen, W. Germany, 1988.

[5] T.F. Yang, F.R. Chang-Díaz, S. Peng, J. Urbahn, and X. Yao. In *AIAA/ASME/SAE/ASEE, 25th Joint Propulsion Conf., paper AIAA-89-2383*, Monterey, CA, 1989.

[6] S. Peng T.F. Yang and F.R. Chang-Díaz. The propagation of rf wave in a tandem mirror plasma propulsion device. In *AIAA/DGLR/JSASS, 21th Joint Propulsion Conf., paper AIAA-90-2638*, Orlando, Fl, 1990.

[7] N. Herschkowitz, R.A. Bruen, and et al. In *Proc. IAEA on Plasma Phys. and Contr. Nucl. Fus. Res.,*, page 553, Vienna, 1981.

[8] Scott Peng, T.F. Yang, and F.R. Chang-Díaz. An icrh beach effect in a tandem mirror device. *To be submitted to Physics of Fluid.*

[9] Scott Peng, , J. Freidberg T.F. Yang, and F.R. Chang-Díaz. An cylindrical model of icrh wave propagation in a tandem mirror device. *To be submitted to Physics of Fluid.*

[10] X.Z. Yao, T.F. Yang, and F.R. Chang-Díaz. Neutral hydrogen density measurement in tmspp. Technical Report PFC/JA-91-23, MIT, 1991.

[11] F.R. Chang-Díaz and T.F. Yang. Design characteristics of the variable i_sp plasma rocket. In *AIDAA/AIAA/DGLR/SASS 22nd Int. Electric Propulsion Conference, IEPC-91-128*, Viareggio, Italy, 1991.

[12] C Hack J. Gilland. Technical Report Private Communication, NASA/LeRC., 1991.

[13] Scott Peng. Wave propagation in tandem mirror plasma propulsion device. Technical Report To be Published, MIT Plasma Fusion Center, 1990.

[14] J. F. Freidberg. Ideal magnetohydrodynamic theory of magnetic fusion systems. *Review of Modern Physics*, 54(3):801–902, 1982.

[15] T. H. Stix. *The Theory of Plasma Waves.* McGraw Hill, New York, 1962.

[16] T.F. Yang, S. Peng, and F.R. Chang-Díaz. An icrf plasma experiment in the tandem mirror propulsion device. In *AIDAA/AIAA/DGLR/SASS 22nd Int. Electric Propulsion Conference,IEPC-91-129*, Viareggio, Italy, 1991.

[17] P. Bogen and E. Hingtz. *Comments Plasma Phys. and Contl. Fusion*, 4:115, 1978.

[18] P. Bogen, R.W. Dreyfus, T. Lie, and H. Langer. *J. Nucl. Mater.*, 111:75, 1982.

[19] P. Gohil, G. Kolbe, M.J. Forrest, D.D. Bargess, and B. Z. Hu. *J. Phys. D*, 16:333, 1983.

[20] W. C. Guss, X. Z. Yao, L. Póca, A. Mahon, J. Casey, and R. S. Post. *Rev. Sci. Instrum.*, 59:1470, 1988.

[21] W. C. Guss, X. Z. Yao, L. Póca, A. Mahon, J. Casey, R. S. Post, and R. P. Torti. *Phys. Fluids*, B2:2168, 1990.

[22] T.F. Yang, C.S. Zu, and F.R. Chang-Díaz. A dual-cable fast scanning langmuir probe. *Will be submitted to Rev. Sci. Instrum.*, page To Be Submitted.

[23] Ultrahigh power space nuclear power system design and development. Technical report, Rocketdyne Div. Report, 1990.

[24] M. A. Leontovich. *Review of Plasma Physics.* AP, New York, second edition, 1965.